Modeling and co–simulation of global transport dynamics in turbulent plasmas

Tomonari Nakayama

Doctor of Philosophy

Department of Fusion Science
School of Physical Sciences
The Graduate University for Advanced Studies,
SOKENDAI

March, 2024

Acknowledgement

First of all, I would like to express deep gratitude to my supervisor Dr. Motoki Nakata for his continuous support and advice. I would like to thank him especially for giving me the freedom to work on the subjects of my interest. Fruitful discussions with him has led me to this work. This thesis would be never completed without his help. Also, I would like to thank Dr. Mitsuru Honda(Kyoto Univ.) for his helpful advice and discussion. He has guided me in many aspects in this work.

I would like to appreciate Dr. Emi Narita(Kyoto Univ.). She gave me a useful suggestion and a lot of comments in modeling study. I also acknowledge Dr. Seikitchi Matsuoka(NIFS), Dr. Masanori Nunami(NIFS). They gave me not only useful discussions of this research but also supported me in the study of basic plasma physics.

I express my acknowledgement to Dr. Yasuhiro Suzuki(Hiroshima Univ.), who encouraged me the Ph.D. course of SOKENDAI. I would also like to thank Dr. Shinsuke Satake(NIFS), to teach me many things about plasma physics. Furthermore, I would like to thank Mr. Go Yatomi, Mr. Kotaro Fujii, Mr. Tetsuji Kato, and other Ph.D. students at NIFS.

Finally, this work was supported by JST SPRING, Grant Number JPMJSP2104. The numerical simulations were carried out by using the JFRS-1 supercomputer system at Computational Simulation Centre of International Fusion Energy Research Centre (IFERC-CSC) in Rokkasho Fusion Institute of QST (Aomori, Japan) and Plasma Simulator (NEC SX-Aurora TSUBASA) in NIFS.

Abstract

In order to realize high performance fusion plasmas, it is crucial to clarify and predict turbulent transport processes and the associated formations of global profiles such as the temperature, density, pressure, electric current, and electric fields. The turbulent transport is driven by various microinstabilities. There have been much effort on these subjects from both aspects of theoretical and experimental studies, and an era of realizing the burning plasma is, nowadays, in prospect.

As a powerful approach, gyrokinetic simulations for the transport and profile formations in turbulent plasmas have been developed, where the global analyses over the whole plasma volume are capable, as well as the radially local analyses. Since the global gyrokinetic simulations require huge computational costs for the target of analysis, it is often difficult to comprehensively scan the various plasma states and heating/fueling scenarios. Also, the coupling effects among the pressure profile evolution, the variation of heating absorption, fueling, plasma current, and the confinement magnetic field, have not fully been considered, where all above dynamics are related to the turbulent transport.

In this thesis, a turbulent transport modeling based on the nonlinear gyrokinetic simulations and mathematical optimization techniques is developed. The constructed simplified transport model enables us to accurately reproduce the turbulent heat diffusivity in the nonlinear gyrokinetic simulation only by the quantities obtained from the linear calculations. Then, a novel global turbulent transport simulation is developed, where the co–simulation framework with the simplified turbulent transport model is utilized. This allows us to calculate the spatio–

temporal evolutions of turbulent transport and the radial profiles under the various heating scenarios at relatively less computational costs. The impact of the background variations on the turbulent transport and profile formations is investigated. The following main results were obtained.

First, a nonlinear functional relation(NFR), which describes a functional relation among the turbulent diffusivity, turbulence intensity, and zonal–flow intensity observed in the local nonlinear gyrokinetic ion temperature gradient(ITG) turbulence simulation, is identified. Considering several functional forms that satisfy the phenomenological requirements, the optimal regression parameters in the NFR are determined by an optimal solution of the mathematical optimization problem to minimize the deviation from the nonlinear simulation results. The relevant physical interpretations are discussed for the choice of the functional form. The newly constructed NFR shows a better reproducibility for a wide parameter region of the temperature gradient including the near– and far–marginal stability of the ITG instability, compared to that in the conventional works. Then, a novel simplified turbulent transport model based on the NFR is constructed by further modeling of the turbulence intensity and zonal–flow intensity with quantities in the linear gyrokinetic calculations. The temperature–gradient dependence is newly incorporated into the modeling of the zonal–flow intensity. The accuracy and robustness of the NFR are verified through the comparison against the conventional model on the turbulent heat diffusivity.

Next, by utilizing the simplified turbulent transport model based on the NFR, a new global transport simulation, AGITO(Alterable Gyrokinetics–Integrated Transport cO–simulation), has been developed, where discretely distributed linear or nonlinear local gyrokinetic calculations are directly coupled with a 1–dimensional transport calculation to solve the time evolution of the temperature, density, and plasma current profiles. The so–called co–simulation framework is applied in terms of MPMD (Multiple Program Multiple Data) parallelization. The numerical verifications for the global ITG-driven turbulence simulation with the station-

ary heating are carried out. It is confirmed that the time evolution of the turbulent diffusivity and temperature profile towards the power–balanced steady state is properly solved.

Finally, the impacts of the heating power modulation and background magnetic modulation on the global profile evolutions in turbulent plasmas are investigated by means of AGITO. It is found that the different time delay appears in each profile, depending on the modulation frequency. Then, in some modulation scenarios, the time–averaged temperature profile deviates from that in the case with the stationary heating. Although the feedback from the pressure and bootstrap current profile evolutions is ignored in the present analysis, a significant deviation from the stationary heating cases suggests new heating and/or modulation scenarios to expect an improved global confinement.

Contents

Chapter 1

Introduction

1.1 Turbulence and transport phenomena in fusion plasmas

Fusion reactor is a promising as the innovative power plant in the future. To obtain the net output power in magnetically confined fusion plasmas, a long–time stable confinement of high–temperature and high–density plasmas is required. The confinement performance is often limited by "transport phenomena" that determine the temperature and density profiles, so–called kinetic profiles. In addition to the macroscopic stability, the study of the transport phenomena in confined plasmas is one of the central issues in fusion plasma research. There are mainly two types of transport phenomena, i.e., "neoclassical transport" due to the coulomb collisions in ions and electrons, "anomalous transport" which generally exceeds the neoclassical one. Nowadays, the anomalous transport is understood as the transport caused by the turbulent fluctuations driven by microscopic instabilities [1], where the typical spatial scale of the fluctuation is the order of gyroradii. Since the turbulent transport is dominant transport processes in confined plasmas, the driving mechanisms and its impacts on the plasma confinement should be clarified for realizing the hith–performance plasmas.

The turbulent transport on the thermal energy and/or particle is driven by the microinstabilities, e.g., the ion (or electron) temperature gradient (ITG) modes, trapped electron modes, kinetic ballooning modes, where the unstable growth of the fluctuations saturate through their nonlinear interactions. Since the radial inhomogeneity of the temperature and density profiles, i.e., the pressure gradient, is the free–energy source of the microinstabilities, the spatio–temporal evolutions of the kinetic profiles and turbulent transport are mutually influenced each other. Note that the heating and/or fueling into the plasma, which is attributed to the external injection or fusion reactions, is also another important mechanism, because they also contribute to the pressure profile evolution as the source. Toroidal magnetic geometries that confine the plasma also play a crucial role in control the transport phenomena. Indeed, the microscopic turbulence and the turbulent transport is strongly influenced by the magnetic geometry.

For the quantitative prediction of the turbulent transport caused by various microinstabilities, many efforts have, so far, been devoted to the first-principle-based nonlinear gyrokinetic simulations [2]. A key finding, which is still one of the ongoing issues, is a spontaneous generation of the so-called zonal flows to suppress the turbulent transport. In addition to recent advances in electromagnetic multi-species and multi–scale local fluxtube simulations [3–6], several validation studies with the experimental data have been carried out [3, 7, 8]. Furthermore, global turbulence simulations including external heating and sink have revealed non–steady and non–local nature of the turbulent transport and zonal–flow dynamics [9–14]. However, the global gyrokinetic simulation often requires huge computational costs to investigate the long–time evolutions of the density and temperature profiles over the confinement time. The comprehensive numerical scans for various operation scenarios are, thus, still limited.

As another powerful approach to predict the long–time profile evolution and the power–balanced steady state, the so–called integrated transport codes, such as TASK/TASK3D [15–17], TOPICS [18, 19], and GOTRESS+ [20, 21], have been

developed, where various simplified models of the transport, stability, and heating proposed by experimental, theoretical, and numerical studies are combined. Indeed, they can individually calculate the magnetic equilibria, heating, fueling, neoclassical and turbulent transport, and time evolutions of the kinetic profiles. However, the models for turbulent transport are over–simplified, making it difficult to accurately predict the realistic profile evolutions.

In order to accelerate the study of global turbulent transport and profile formations towards the future burning plasmas, the development of a novel simplified turbulent transport model, which accurately reproduces the gyrokinetic simulation results but can be evaluated enough quickly, is indispensable. Once such a transport modeling with a remarkable reduction of computational resources was established, one can look towards the further capabilities to explore new global simulations with self–consistent interactions between the turbulent transport and the spatio–temporal variations of heating and magnetic fields, etc., which have been ignored in earlier studies. This is a main focus in this study.

The rest of this chapter is organized as follows. The basic theoretical framework on the turbulent transport is briefly reviewed in Sec. 1.2. Then, the scope of the present study is summarized in Sec. 1.3.

1.2 Brief review of theoretical framework

In this section, the theoretical framework in this study is briefly presented. One can easily find the details in e.g., Ref. [2]. The basic equation of transport phenomena in plasmas is given by Boltzmann equation as:

$$\frac{\partial}{\partial t} f_{\mathrm{s}}(\boldsymbol{q}, \boldsymbol{p}, t) + \{f_{\mathrm{s}}, \mathcal{H}_{\mathrm{s}}\} = C(f_{\mathrm{s}}), \tag{1.1}$$

$$\mathcal{H}_{\mathrm{s}}(\boldsymbol{q}, \boldsymbol{p}, t) = \frac{1}{2m_{\mathrm{s}}} \left(\boldsymbol{p} - e_{\mathrm{s}} \boldsymbol{A}(\boldsymbol{q})\right)^2 + e_{\mathrm{s}} \phi(\boldsymbol{q}). \tag{1.2}$$

Here, $f_{\rm s}(\boldsymbol{q},\boldsymbol{p},t)$ and $\mathcal{H}_{\rm s}(\boldsymbol{q},\boldsymbol{p},t)$ are 6–dimensional distribution functions and Hamiltonian for the particle species "s", respectively. The Hamiltonian determines the motion of a single particle in a 6–dimensional phase space, represented by the canonical coordinates $\boldsymbol{q}$ and $\boldsymbol{p}$, respectively. The bracket symbol $\{\cdots\}$ in the second term on the left-hand side means Poisson brackets, and $C(f_{\rm s})$ is a collision operator. When the total distribution function $f_{\rm s}$ and the Hamiltonian $\mathcal{H}_{\rm s}$ are expanded to a series of the macroscopic equilibrium part and the microscopic fluctuation part, by means of a small expansion parameter ϵ, one finds

$$f_{\rm s} = F_{\rm s,0} + \delta f_{\rm s} + \mathcal{O}(\epsilon^2), \tag{1.3}$$

$$\mathcal{H}_{\rm s} = \mathcal{H}_{\rm s,0} + \mathcal{H}_{\rm s,1} + \mathcal{O}(\epsilon^2), \tag{1.4}$$

where $F_{\rm s,0}$ is regarded as $\langle f_{\rm s}\rangle_{\rm ens}$ with the ensemble average. In the microscopic fluctuations driven by microinstabilities (sometimes called drift–wave instabilities), the spatial scale, the typical frequency, and the magnitude of fluctuation amplitude are assumed to be related to ϵ as follows:

$$\frac{k_\parallel}{k_\perp} \sim \frac{\omega_{\rm t}}{\Omega_{\rm s}} \sim \frac{e_{\rm s}\delta\phi}{T_{\rm s}} \sim \frac{\delta B}{B_0} \sim \epsilon = \frac{\rho_{\rm ti}}{a}, \tag{1.5}$$

where, $\rho_{\rm ts} = v_{\rm ts}m_{\rm s}/e_{\rm s}B_0$ is the gyroradius with the thermal velocity $v_{\rm ts}$, the particle mass $m_{\rm s}$, the strength of magnetic field B_0, the electric charge $e_{\rm s}$, and the plasma radius a. $\omega_{\rm ts} = v_{\rm ts}/R$ is the transit frequency, and the gyrofrequency is given by $\Omega_{\rm s} = e_{\rm s}B_0/m_{\rm s}$. Also, $\delta\phi$ and $\delta B = |\nabla \times \delta\boldsymbol{A}|$ denote the potential and magnetic fluctuations, respectively. The mean temperature is denoted as $T_{\rm s}$. The parallel and perpendicular components of the wavenumber vector correspond to $k_\parallel$ and $k_\perp$, respectively. Substituting Eq. (1.3) and Eq. (1.4) into Eq. (1.1) and separating them into the macroscopic and microscopic parts by taking the

ensemble average, the following equations are obtained:

$$\frac{\partial}{\partial t}F_{\mathrm{s},0} + \{F_{\mathrm{s},0}, \mathcal{H}_{\mathrm{s},0}\} + \langle\{\delta f_{\mathrm{s}}, \mathcal{H}_{\mathrm{s},1}\}\rangle_{\mathrm{ens}} = C(F_{\mathrm{s},0}), \tag{1.6}$$

$$\frac{\partial}{\partial t}\delta f_{\mathrm{s}} + \{\delta f_{\mathrm{s}}, \mathcal{H}_{\mathrm{s},0}\} + \{F_{\mathrm{s},0}, \mathcal{H}_{\mathrm{s},1}\} + \{\delta f_{\mathrm{s}}, \mathcal{H}_{\mathrm{s},1}\} = C(\delta f_{\mathrm{s}}). \tag{1.7}$$

Here, we assume that the time scale of $F_{\mathrm{s},0}$ is much smaller than that of δf_{s}, and the $\langle\{\delta f_{\mathrm{s}}, \mathcal{H}_{\mathrm{s},1}\}\rangle_{\mathrm{ens}}$ term is ignored in Eq. (1.7) since the ensemble averaged quantity is no longer fluctuating variable, and should be treated in macroscopic equation. These are the time evolution equations for macroscopic and microscopic distribution functions, but generally it is difficult to deal directly because of the 6–dimensional nature. Therefore, it is necessary to impose an appropriate approximation for each equation. In the following, real–space position $\boldsymbol{x}$ and velocity $\boldsymbol{v}$ are used as the phase–space variables instead of $\boldsymbol{q}$ and $\boldsymbol{p}$.

The macroscopic equation (1.6) describes physics in the time scales slower than that in the microscopic fluctuations. Taking the second-order velocity moment of Eq. (1.6), the following the energy balance equation is obtained:

$$\frac{3}{2}\frac{\partial}{\partial t}p_{\mathrm{s}} + \nabla\cdot\left(\boldsymbol{\mathcal{Q}}_{\mathrm{s}} + \frac{5}{2}p_{\mathrm{s}}\boldsymbol{u}_{\mathrm{s}} + \boldsymbol{u}_{\mathrm{s}}\cdot\boldsymbol{\Pi}_{\mathrm{s}}\right) = \boldsymbol{u}_{\mathrm{s}}\cdot(\nabla p_{\mathrm{s}} + \nabla\cdot\boldsymbol{\Pi}_{\mathrm{s}}) + \mathcal{P}_{\mathrm{s}}. \tag{1.8}$$

Here, p_{s}, $\boldsymbol{\mathcal{Q}}_{\mathrm{s}}$, $\boldsymbol{u}_{\mathrm{s}}$, and $\boldsymbol{\Pi}_{\mathrm{s}}$ correspond to the scalar pressure, the heat flux, the velocity field, and the viscosity tensor, respectively. Heat production by collision is denoted by $\mathcal{P}_{\mathrm{s}}$. For further simplification, we ignore $\boldsymbol{\Pi}_{\mathrm{s}}$ and $\mathcal{P}_{\mathrm{s}}$ in the following. Then, taking the flux surface average to extract only the radial dependence, a one-dimensional transport equation is obtained as follows:

$$\frac{3}{2}\frac{\partial}{\partial t}p_{\mathrm{s}} = -\frac{1}{V'}\frac{\partial}{\partial r}V'\left(\frac{5}{2}T_{\mathrm{s}}\Gamma_{\mathrm{s}} + Q_{\mathrm{NC,s}} + Q_{\mathrm{trb,s}}\right) + S_{\mathrm{s}}, \tag{1.9}$$

where V', $\Gamma_{\mathrm{s}} \equiv \langle n_{\mathrm{s}}\boldsymbol{u}_{\mathrm{s}}\cdot\nabla r\rangle$, and $Q_{\mathrm{NC,s}} + Q_{\mathrm{trb,s}} \equiv \langle\boldsymbol{\mathcal{Q}}_{\mathrm{s}}\cdot\nabla r\rangle$ denote the specific

volume, the radial particle flux, and the radial heat flux composed of the neoclassical and turbulence parts, respectively. $S_{\rm s}$ means an ad hoc energy source term resulting from the external heating. Turbulent radial heat flux is determined by solving the microscopic equation of Eq. (1.7). The pressure profile, which is approximately given by $p_{\rm s} = n_{\rm s}T_{\rm s}$, develops until the right–hand side vanishes. In other words, a steady state is realized when the heating flux and transport flux are in balance.

As for the equation of microscopic distribution function Eq. (1.7), the so–called gyrokinetic equation is derived as follows:

$$\begin{aligned}
&\left[\frac{\partial}{\partial t} + v_\parallel \nabla_\parallel + i\omega_{\rm Ds} - \left(\frac{e_{\rm s}\mu}{m_{\rm i}}\nabla_\parallel B\right)\frac{\partial}{\partial v_\parallel}\right]\delta f_{{\rm s}\boldsymbol{k}_\perp} \\
- &\frac{1}{B}\sum_{\boldsymbol{k}'_\perp + \boldsymbol{k}''_\perp = \boldsymbol{k}_\perp} \boldsymbol{b}\cdot(\boldsymbol{k}'_\perp \times \boldsymbol{k}''_\perp) J_0(k'_\perp \rho_{\rm s})\delta\phi_{\boldsymbol{k}'_\perp}\delta f_{{\rm s}\boldsymbol{k}''_\perp} \\
= &\frac{e_{\rm s}F_{\rm Ms}}{T_{\rm s}}(i\omega_{*T{\rm s}} + i\omega_{\rm Ds} - v_\parallel\nabla_\parallel)J_0(k_\perp\rho_{\rm s})\delta\phi_{\boldsymbol{k}_\perp} + C_{\rm s}, \qquad (1.10)
\end{aligned}$$

where the Fourier representation in the perpendicular spatial coordinate ($\boldsymbol{x}_\perp \to \boldsymbol{k}_\perp$) is applied. One can find the detail derivations of the above gyrokinetic equation in e.g., Ref. [2,22]. Here, $\delta\Psi_{\boldsymbol{k}_\perp} = J_0\delta\phi_{\boldsymbol{k}_\perp}$ is the gyrophase–averaged electrostatic potential fluctuations with the zeroth order Bessel function J_0. The macroscopic distribution function $F_{\rm s,0}$ was assumed to be Maxwellian distribution function $F_{\rm Ms} = n_{\rm s}(m_{\rm s}/2\pi T_{\rm s})^{3/2}\exp[-(m_{\rm s}{v_\parallel}^2 + 2\mu B)/2T_{\rm s}]$. The drift frequency, and the diamagnetic frequency are denoted by $\omega_{\rm Ds}$, $\omega_{*T{\rm s}}$, respectively.

In order to solve Eq. (1.10) self–consistently, the Poisson equation to determine $\delta\phi_{\boldsymbol{k}_\perp}$ is given by:

$$\left[k_\perp^2 + \sum_{\rm s}\frac{1}{\lambda_{D{\rm s}}}(1 - \Gamma_{0{\rm s}\boldsymbol{k}_\perp})\right]\delta\phi_{\boldsymbol{k}_\perp} = \frac{1}{\varepsilon_0}\sum_{\rm s} e_{\rm s}\int d\boldsymbol{v}\, J_0\delta f_{{\rm s}\boldsymbol{k}_\perp}. \qquad (1.11)$$

Here, $|e_{\rm i}| = |e_{\rm e}| = e$ and $n_{\rm i} = n_{\rm e} = n_0$ are assumed. The Debye–length, factors $J_{0,{\rm s}}$ and $\Gamma_{0{\rm s}\boldsymbol{k}_\perp}$ are denoted as $\lambda_{D{\rm s}} \equiv (T_{\rm e}\varepsilon_0/n_0e^2)^{1/2}$, $J_{0,{\rm s}} \equiv J_0(k_\perp\rho_{\rm s})$, and $\Gamma_{0{\rm s}\boldsymbol{k}_\perp} \equiv$

$e^{-b}I_0(b)$ with $b = (k_\perp \rho_{\rm ti})^2$, respectively.

The radial turbulent flux appearing in Eq. (1.9) is given as the second order correlation of $\delta f_{{\rm s}\boldsymbol{k}_\perp}$ and $\delta\phi_{\boldsymbol{k}}$ in the following form:

$$\begin{aligned} Q_r &= {\rm Re}\left\langle \sum_{\boldsymbol{k}_\perp} \int d\boldsymbol{v} \left(\frac{m_{\rm s} v^2}{2} - T_{\rm s} \right) \delta f_{{\rm s}\boldsymbol{k}_\perp} \delta \boldsymbol{v}^*_{\boldsymbol{E}\boldsymbol{k}_\perp} \cdot \nabla r \right\rangle \\ &= \left\langle \sum_{\boldsymbol{k}_\perp} \int d\boldsymbol{v} \left(\frac{m_{\rm s} v^2}{2} - T_{\rm s} \right) \frac{\boldsymbol{b} \times \boldsymbol{k}_\perp \cdot \nabla r}{B} {\rm Im} \left[\frac{\delta f_{{\rm s}\boldsymbol{k}_\perp}}{\delta \phi_{\boldsymbol{k}_\perp}} \right] |\delta \phi_{\boldsymbol{k}_\perp}|^2 \right\rangle \end{aligned} \tag{1.12}$$

where, $\delta \boldsymbol{v}_{\boldsymbol{E}\boldsymbol{k}_\perp} = i\boldsymbol{b} \times \boldsymbol{k}_\perp \delta\phi_{\boldsymbol{k}_\perp}/B$ denotes the $\boldsymbol{E} \times \boldsymbol{B}$ drift velocity driven by the electrostatic potential fluctuations.

The equations derived in this section have been utilized extensively in transport studies. In this study, the global profile formation is evaluated by Eq. (1.9), while the local turbulent transport flux or diffusivity is evaluated by using Eqs. (1.10), (1.11), and (1.12), keeping $F_{\rm s,0}$ to be stationary. Because of the scale separation assumption in the time scales between $F_{\rm s,0}$ and $\delta f_{{\rm s}\boldsymbol{k}_\perp}$, Eq. (1.9) and Eq. (1.10) are separately calculated in the numerical simulations.

1.3 Scope of this study

In burning plasmas, the confinement performance and the burning efficiency are dominantly governed by the turbulent transport, where the global analysis of profile formations becomes more crucial than the local analysis of turbulent transport properties. Also, in addition to the global turbulence dynamics for given heating and magnetic fields, the spatio–temporal variations of the heating deposition and confinement magnetic fields coupled with turbulent transport through the pressure profile formation become more crucial in the high-performance plasmas, where the most of plasma current is sustained by the pressure–gradient driven bootstrap current.

To explore such unrevealed physics, a novel simulation framework for the

global transport analysis is developed in this study. It is realized by constructing an extended simplified model to reproduce the turbulent diffusivity and zonal–flow intensity in the nonlinear gyrokinetic simulation results. The simplified model provides us with quick and accurate estimations of the turbulent transport only by the linear calculations, and is utilized to combine into co–simulation framework for the global transport simulation.

The rest of this thesis is organized as follows. The identification of the nonlinear functional relation (NFR), which is a key building brick to construct the simplified model, is discussed in Chap. 2. Then, Chap. 3 describes how to construct the turbulent transport model based on the NFR. The basic concept and numerical verification of the novel global transport simulation by utilizing the simplified transport model is presented in Chap. 4. The simulations results for transport and profile evolutions with temporal modulations of the heating and the magnetic fields are shown in Chap. 5. The summary is given in Chap. 6.

Chapter 2

Nonlinear functional relation(NFR) in turbulent transport

2.1 Introduction

For quantitative predictions of turbulent transport, it is useful to clarify the relationship among the transport fluxes, turbulence intensity, and zonal–flow intensity. Such relationship can provide us with important informations to construct a simplified transport model, including the effect of transport suppression due to turbulence nonlinearity. Theoretical and numerical studies on the simplified models for the turbulent transport have extensively been conducted so far, where some remarkable models such as GLF23 [23], TGLF [24–26], and QuaLiKiz [27] have been proposed in the framework of quasi-linear gyrokinetic and gyrofluid approaches. The effects of multi-scale fluctuations [28] and mean $\boldsymbol{E} \times \boldsymbol{B}$ flow shear [29] are also incorporated. Moreover, a combined modeling based on the linear and nonlinear gyrokinetic simulations has also been explored, where the impacts of turbulence nonlinearity and zonal flow generation on the ion temperature gradient(ITG) driven turbulent thermal transport for ions have been taken into account [30]. An extension to the electron–thermal and particle transport has been applied in the similar manner [31–34].

Furthermore, modeling studies with deep neural networks have actively been addressed as another recent approach [20, 35–37]. Experimentally and/or numerically produced massive datasets regarding the radial kinetic profiles and the transport fluxes, etc., are utilized for the training of deep neural networks. Then, one can rapidly estimate the turbulent transport fluxes or the related diffusivities from the several inputs of known physical parameters such as the safety factor, local background density and temperature, and their logarithmic gradients. Indeed, a semi-empirical neural network model, which was constructed by using the local gyrokinetic simulation and JT–60U experiment data, well reproduces the particle and thermal transport fluxes in neutral-beam-heated plasmas [38–40]. Although such deep-neural-network-based modeling are powerful, one should note that the physical expandability or interpretability and the extrapolation capability are generally limited in the approach with deep neural networks.

In this study, to describe turbulent transport processes in a simplified form, an extended modeling based on a nonlinear functional relation(NFR) is proposed [41]. In the NFR, the nonlinearity among turbulence, zonal flows, and thermal transport flux in tokamak ITG driven turbulence is phenomenologically incorporated by means of the nonlinear gyrokinetic simulations and mathematical optimization techniques. Since significant variations of the profile gradients have often been observed in the global turbulent transport [10], the NFR is verified to be valid for a wide range of the physical parameters such as the temperature gradient and the radial domains, including near- and far-marginal linear ITG stability. Indeed, the importance of the zonal–flow effects in the near–marginal regime, as known as Dimits-shift [42], has been revealed in several gyrokinetic simulation studies regarding the near-marginal or sub-critical turbulence dynamics [43, 44] and the isotope effects [7, 45]. Encompassing such strong zonal–flow effects is necessary to predict accurately the dynamical evolutions of the kinetic profiles and the magnetic equilibria in the global transport processes of confined plasmas. Once the systematic methodology to proposed an accurate NFR is established,

various simplified transport models can be induced by combining the conventional modeling [30–34] with linear gyrokinetic calculations, as will be shown later. Also, the phenomenological arguments in the present NFR approach enable us to extract the physical interpretations and useful suggestions to improve the accuracy of the model.

The rest of this chapter is organized as follows. In Sec. 2.2, the gyrokinetic model and the nonlinear simulation results for the tokamak ITG driven turbulence including the Dimits-shift regime are presented. Then, based on three types of nonlinear functional relations, the identification of their regression parameters by using mathematical optimization techniques is discussed in Sec. 2.3. Further investigations for a key factor to determine the reproduction accuracy are shown in Sec. 2.4. The verifications of the accuracy and the versatility are given in Sec. 2.5. The robustness of optimal regression parameters is discussed in Sec. 2.6.

2.2 Gyrokinetic ITG turbulence simulation

Gyrokinetic turbulence simulation model and numerical results are shown in this section. Various datasets regarding the turbulence intensity, the zonal flow intensity, and the turbulent transport coefficient, which strongly depend on the temperature gradient, are prepared to construct the NFR, as will be discussed in Sec. 2.3 and Sec. 2.4.

The ITG driven turbulent transport simulations in a tokamak equilibrium are performed by using a gyrokinetic Vlasov simulation code GKV [46]. Since the nonlinear modeling incorporating the strong zonal–flow effects is of particular focus in this study, the electrostatic limit with the adiabatic electron response is assumed for simplicity. The gyrokinetic-Poisson equations in Fourier wavenum-

ber representation derived in Sec. 1.2 are summarized as follows:

$$\begin{aligned}
&\left[\frac{\partial}{\partial t}+v_{\parallel}\nabla_{\parallel}+i\omega_{\mathrm{Ds}}-\left(\frac{e_{\mathrm{s}}\mu}{m_{\mathrm{i}}}\nabla_{\parallel}B\right)\frac{\partial}{\partial v_{\parallel}}\right]\delta f_{\mathrm{s}\boldsymbol{k}_{\perp}}\\
-\ &\frac{1}{B}\sum_{\boldsymbol{k}'_{\perp}+\boldsymbol{k}''_{\perp}=\boldsymbol{k}_{\perp}}\boldsymbol{b}\cdot(\boldsymbol{k}'_{\perp}\times\boldsymbol{k}''_{\perp})J_0(k'_{\perp}\rho_{\mathrm{s}})\delta\phi_{\boldsymbol{k}'_{\perp}}\delta f_{\mathrm{s}\boldsymbol{k}''_{\perp}}\\
=\ &\frac{e_{\mathrm{s}}F_{\mathrm{Ms}}}{T_{\mathrm{s}}}(i\omega_{*T\mathrm{s}}+i\omega_{\mathrm{Ds}}-v_{\parallel}\nabla_{\parallel})J_0(k_{\perp}\rho_{\mathrm{s}})\delta\phi_{\boldsymbol{k}_{\perp}}+C_{\mathrm{s}},
\end{aligned}$$

$$\begin{aligned}
&\left[k_{\perp}^2+\frac{1}{\varepsilon_0}\sum_{\mathrm{s}}\frac{e_{\mathrm{s}}^2n_{\mathrm{s}}}{T_{\mathrm{s}}}(1-\Gamma_{0\mathrm{s}\boldsymbol{k}_{\perp}})\right]\delta\phi_{\boldsymbol{k}_{\perp}}\\
&\quad=\frac{1}{\varepsilon_0}\sum_{\mathrm{s}}e_{\mathrm{s}}\int d\boldsymbol{v}\ J_0(k_{\perp}\rho_{\mathrm{s}})\delta f_{\mathrm{s}\boldsymbol{k}_{\perp}},
\end{aligned}$$

where $\delta f_{\mathrm{s}\boldsymbol{k}_{\perp}} = \delta f_{\mathrm{s}\boldsymbol{k}_{\perp}}(z, v_{\parallel}, \mu, t)$ denotes the perturbed gyrocenter distribution function for the particle species "s", which is represented in the fluxtube coordinates. Here, $\boldsymbol{k}_{\perp} = (k_x, k_y)$, $\boldsymbol{b}$, B, $\delta\phi_{\boldsymbol{k}_{\perp}}$, μ, e_{s}, m_{s}, and T_{s} are the perpendicular wavenumber vector, the unit vector parallel to the field line, the magnetic field strength, the electrostatic potential fluctuation, the magnetic moment, the electric charge, the particle mass, and the temperature for each particle species, respectively. The drift frequency, the diamagnetic frequency, and the gyroradius are denoted by ω_{Ds}, $\omega_{*T\mathrm{s}}$, and ρ_{s}, respectively. The finite gyroradius effects are represented by the 0th-order Bessel function J_0 and $\Gamma_0 = e^{-b}I_0(b)$ with $b = (k_{\perp}\rho_{\mathrm{ti}})^2$, where the 0th-order modified Bessel function, the ion thermal speed, and the ion thermal gyroradius are I_0, $v_{\mathrm{ti}} = \sqrt{T_{\mathrm{i}}/m_{\mathrm{i}}}$, and $\rho_{\mathrm{ti}} = m_{\mathrm{i}}v_{\mathrm{ti}}/e_{\mathrm{i}}B$, respectively. Maxwellian distribution and the collision operator are represented by F_{M} and C_{s}, respectively.

The turbulent thermal transport flux in the radial direction Q_r is given by

$$
\begin{aligned}
Q_r &= \mathrm{Re}\left\langle \sum_{\boldsymbol{k}_\perp} \int d\boldsymbol{v} \left(\frac{m_\mathrm{s} v^2}{2} - T_\mathrm{s} \right) \delta f_{\mathrm{s}\boldsymbol{k}_\perp} \delta \boldsymbol{v}^*_{\boldsymbol{E}\boldsymbol{k}_\perp} \cdot \nabla r \right\rangle \\
&= \left\langle \sum_{\boldsymbol{k}_\perp} \int d\boldsymbol{v} \left(\frac{m_\mathrm{s} v^2}{2} - T_\mathrm{s} \right) \frac{\boldsymbol{b} \times \boldsymbol{k}_\perp \cdot \nabla r}{B} \mathrm{Im} \left[\frac{\delta f_{\mathrm{s}\boldsymbol{k}_\perp}}{\delta \phi_{\boldsymbol{k}_\perp}} \right] |\delta \phi_{\boldsymbol{k}_\perp}|^2 \right\rangle.
\end{aligned}
$$

Here, $\delta \boldsymbol{v}_{\boldsymbol{E}\boldsymbol{k}_\perp} = i\boldsymbol{b} \times \boldsymbol{k}_\perp \delta \phi_{\boldsymbol{k}_\perp} / B$ denotes the $\boldsymbol{E} \times \boldsymbol{B}$ drift velocity driven by the electrostatic potential fluctuations. The superscript "$*$" means the complex conjugate. The flux surface average is denoted by $\langle \cdots \rangle$. One finds that the turbulent flux is proportional to the product of the potential fluctuation amplitude $|\delta \phi_{\boldsymbol{k}_\perp}|^2$ and the phase difference of $\mathrm{Im}[\delta f_{\mathrm{s}\boldsymbol{k}_\perp} / \delta \phi_{\boldsymbol{k}_\perp}]$ as shown in the second equality of Eq (1.12). The turbulent diffusivity is defined by $\chi_\mathrm{s} = (Q_r / n_\mathrm{s} T_\mathrm{s} R)(R/L_T)$, where n_s, r, R, and $1/L_T \equiv -(\partial \ln T_\mathrm{s} / \partial r)$ mean the background density, the radial position, major radius of the magnetic axis, and the logarithmic temperature gradient, respectively.

Spatially averaged turbulence potential intensity $\mathcal{T}$ and zonal–flow potential intensity $\mathcal{Z}$ are defined as follows:

$$
\mathcal{T} \equiv \frac{1}{2} \sum_{k_x, k_y \neq 0} \langle |\delta \phi_{k_x, k_y}|^2 \rangle, \tag{2.1}
$$

$$
\mathcal{Z} \equiv \frac{1}{2} \sum_{k_x} \langle |\delta \phi_{k_x, k_y = 0}|^2 \rangle. \tag{2.2}
$$

In order to identify the nonlinear relationship among $\mathcal{T}$, $\mathcal{Z}$, and χ_i, R/L_T-dependence of each quantity is investigated by gyrokinetic turbulence simulations.

As shown in Eq. (1.12), the turbulent heat flux Q_r is generally given by the second order correlation of $\delta \phi_{\boldsymbol{k}_\perp}$ and $\delta f_{\mathrm{s}\boldsymbol{k}_\perp}$. On the other hand, when the nonlinearity in Eq. (1.10) is neglected, the turbulent flux in Eq. (1.12) is reduced to

so–called quasi–linear flux $Q_r^{\rm QL}$ as follows:

$$
\begin{aligned}
Q_r^{\rm QL} &= {\rm Re}\left\langle \sum_{\boldsymbol{k}_\perp} \mathcal{L}_{\boldsymbol{k}_\perp} |\delta\phi_{\boldsymbol{k}_\perp}|^2 \right\rangle, \\
\mathcal{L}_{\boldsymbol{k}_\perp} &= \int d\boldsymbol{v}\; i\frac{e_{\rm s}F_{\rm Ms}k_y}{T_{\rm s}B}\left(\frac{mv^2}{2}\right)\frac{\omega_{*T{\rm s}}+\omega_{\rm Ds}-k_\parallel v_\parallel}{\omega_{\boldsymbol{k}_\perp}-\omega_{\rm Ds}-k_\parallel v_\parallel}.
\end{aligned}
\tag{2.3}
$$

Here, $\omega_{\boldsymbol{k}_\perp} = \omega_r + i\gamma$ denotes the complex frequency that is composed of the mode frequency as the real part and the growth rate as the imaginary part. Through the relation of $|\delta\phi_{\boldsymbol{k}_\perp}|^2 \sim \mathcal{T}$, $Q_r^{\rm QL}$ can be approximated to $Q_r^{\rm QL} \sim C\mathcal{T}^\alpha$, where C is a constant and $\alpha = \mathcal{O}(1)$.

Table 2.1 summarizes the physical parameters used in the gyrokinetic simulation. The linear and nonlinear simulations are performed for a wide range of the ion temperature gradient R/L_T at two normalized radial positions $\rho \equiv r/a$ in a tokamak magnetic configuration as shown in Fig. 2.1, where a is the minor radius of the plasma. The safety factor and the magnetic shear are denoted by q and $\hat{s}$. The logarithmic density gradient R/L_n is fixed to 2.2. The phase-space grid number is $(n_{k_x}, n_{k_y}, n_z, n_{v_\parallel}, n_\mu)$, where $\mu \equiv m_{\rm s}v_\perp^2/2B$. The minimum wavenumbers are represented by Δk_x and Δk_y. The velocity–space domain of $0 \le v_\perp \le 4v_{\rm ti}$, and $-4v_{\rm ti} \le v_\parallel \le 4v_{\rm ti}$ are considered. In total, 17 nonlinear ITG turbulence simulations for weakly collisional plasmas are performed.

Table 2.1: Physical parameters used in the gyrokinetic simulations.

Parameter	value and range			
radial position ρ	0.25	0.5	0.6	0.75
safety factor q	1.00	1.41	1.70	2.39
magnetic shear $\hat{s}$	0.231	0.885	1.23	1.84
temperature gradient R/L_T	5.1 to 12	4.7 to 12	4.25 to 12	4.2 to 9
density gradient R/L_n	2.2	2.2	2.2	2.2
collisionality ν_{ii}^*	0.056	0.056	0.056	0.056
minimum wavenumber $(\Delta k_x, \Delta k_y)$	(0.054, 0.075)	(0.069,0.075)	(0.073,0.075)	(0.072,0.075)
$\boldsymbol{k}$–space grid number (n_{k_x}, n_{k_y})	$(\pm 24, 20)$	$(\pm 64, 20)$	$(\pm 96, 20)$	$(\pm 128, 20)$
field line grid number n_z	64	64	64	64
velocity–space grid number $(n_{v_\parallel}, n_\mu)$	$(\pm 24,12)$	$(\pm 24,12)$	$(\pm 24,12)$	$(\pm 24,12)$

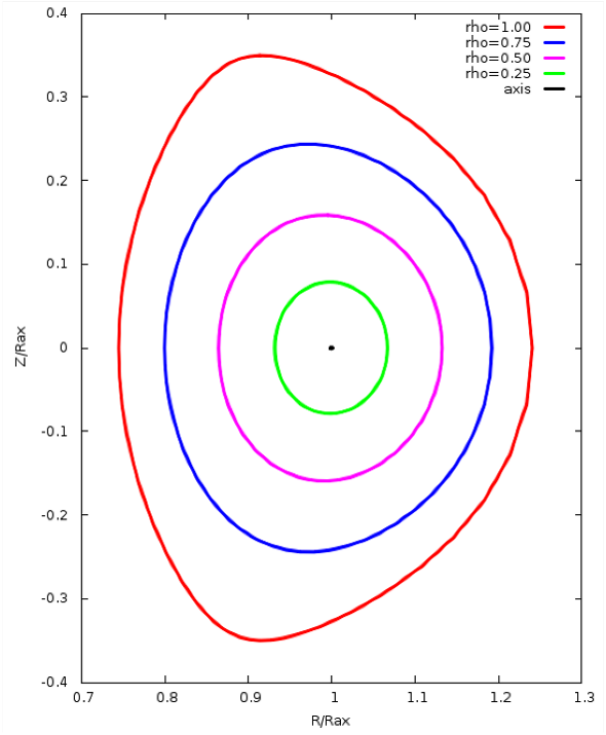

Fig. 2.1: Tokamak geometry used in the gyrokinetic simulation.

Figure 2.2 shows the time evolution of the turbulent heat diffusivity in the gyro-Bohm unit $\chi_{\rm i}/\chi_{\rm i}^{\rm GB}$, where $\chi_{\rm i}^{\rm GB} \equiv \rho_{\rm ti}^2 v_{\rm ti}/R$. Note that the time in the horizontal axis is normalized by the maximum ITG-mode growth rate $\gamma_{\rm max}$. The quasi–steady states for $t\gamma_{\rm max} \geq 50$ are confirmed for all cases. In this study, the time window of $(100 \leq t\gamma_{\rm max} < 300)$ is considered for the average of $\bar{\chi}_{\rm i}/\chi_{\rm i}^{\rm GB}$, $\bar{\mathcal{T}}$, and $\bar{\mathcal{Z}}$. The overline is the time-averaging symbol, which is, hereafter, omitted for simplicity.

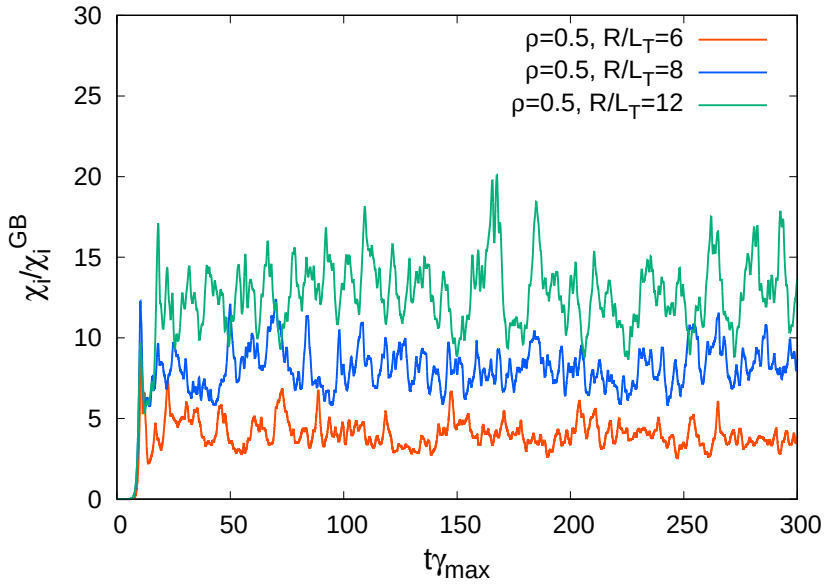

Fig. 2.2: Time evolutions of turbulent heat diffusivity $\chi_{\rm i}/\chi_{\rm i}^{\rm GB}$ at $\rho = 0.5$. Each curve corresponds to the cases for $R/L_T = 6, 8, 12$, respectively.

Figure 2.3(a) shows the R/L_T-dependence of $\chi_{\rm i}/\chi_{\rm i}^{\rm GB}$ and the maximum ITG-mode growth rate $\gamma_{\rm max}$. One can see a slight difference between the critical gradient of the linear ITG instability growth rate and the effective gradient driving the turbulent heat transport near $R/L_T \sim 4$, which is so–called the Dimits–shift [42]. Here, the critical gradient for the ITG instability is estimated by zero value of the fitting function of data for $R/L_T = 4 \sim 5$. The width of the Dimits-shift is evaluated as $\Delta(R/L_T) = R/L_T|_{\text{finite } \chi_{\rm i}/\chi_{\rm i}^{\rm GB}} - R/L_T|_{\text{ITG crit. } \gamma_{\rm max}} = 0.861$ at $\rho = 0.5$ and $\Delta(R/L_T) = 0.296$ at $\rho = 0.75$. The ratio of the zonal–flow potential intensity to the total fluctuations, defined by $\mathcal{Z}/(\mathcal{T} + \mathcal{Z})$, as a function of R/L_T is shown in Fig. 2.3(b). One finds a significantly larger zonal–flow ratio $\mathcal{Z}/(\mathcal{T}+\mathcal{Z})$ near the critical gradient, where the transport reduction can occur. For the larger temperature gradient region of $R/L_T \geq 6$, the zonal flow ratio indicates a moderate dependence. The magnitude of Dimits–shift discussed here indicates

a positive correlation not only to the relative intensity $\mathcal{Z}/(\mathcal{T}+\mathcal{Z})$, but also to the residual zonal–flow level [47–49]. From the linear zonal–flow response calculation, the residual zonal–flow levels $\mathcal{K}$ are evaluated as $\mathcal{K} = 0.0428(\rho = 0.5)$, and $\mathcal{K} = 0.0259(\rho = 0.75)$, where the analytic estimations in the limit of the large–aspect–ratio circular cross section by Rosenbluth and Hinton [47] are $\mathcal{K}_{\rm RH} = 0.145(\rho = 0.5)$, and $\mathcal{K}_{\rm RH} = 0.0558(\rho = 0.75)$. These quantities can be useful to explain the qualitative trends in the nonlinear simulation results in Fig. 2.3.

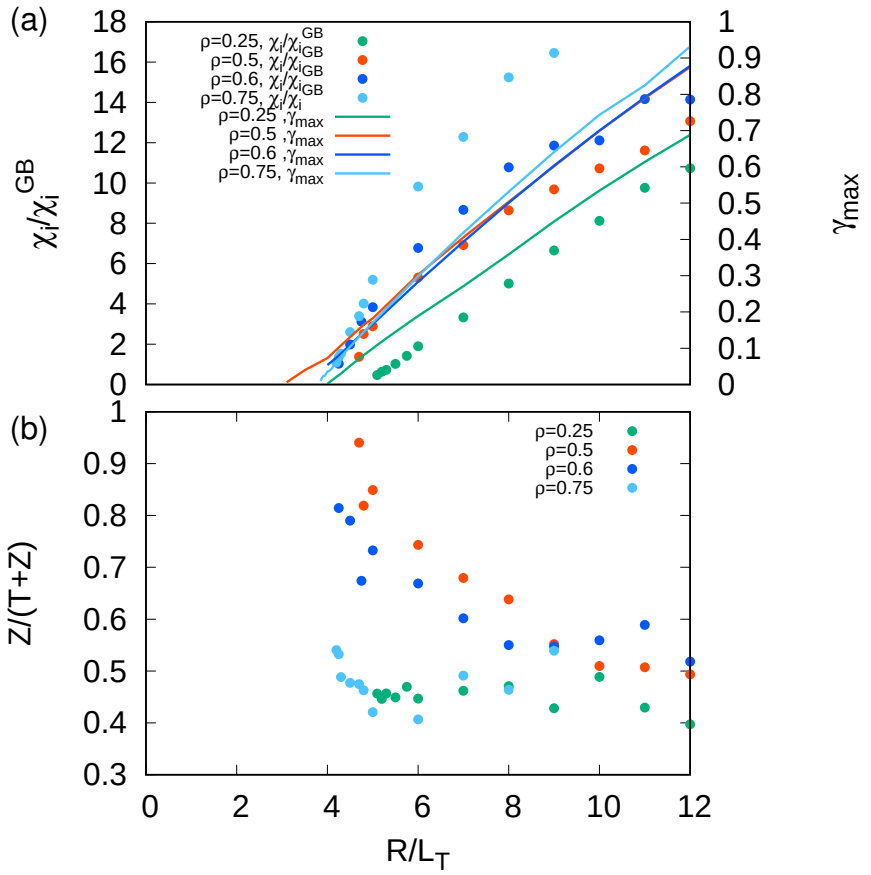

Fig. 2.3: (a)Temperature gradient dependence of $\chi_{\rm i}/\chi_{\rm i}^{\rm GB}$ evaluated by nonlinear simulations (symbols) and $\gamma_{\rm max}$ $[v_{\rm ti}/R]$ by linear analysis (lines). (b)The ratio of the zonal–flow potential intensity $\mathcal{Z}$ to the total fluctuation amplitude $(\mathcal{T}+\mathcal{Z})$.

Furthermore, the spectral shape of the turbulent potential fluctuation in the wavenumber space is exemplified in Fig. 2.4. It can be seen that for the turbu-

lence (non-zonal $k_y \neq 0$) and zonal flow ($k_y = 0$) components, the shape of the spectrum is rather different between the cases with high and low temperature gradients. Such various nonlinear dependence on R/L_T appearing in $\mathcal{T}$, $\mathcal{Z}$, and $\chi_{\rm i}$ is crucial for constructing the simplified transport model, which is valid for a wide parameter range of R/L_T.

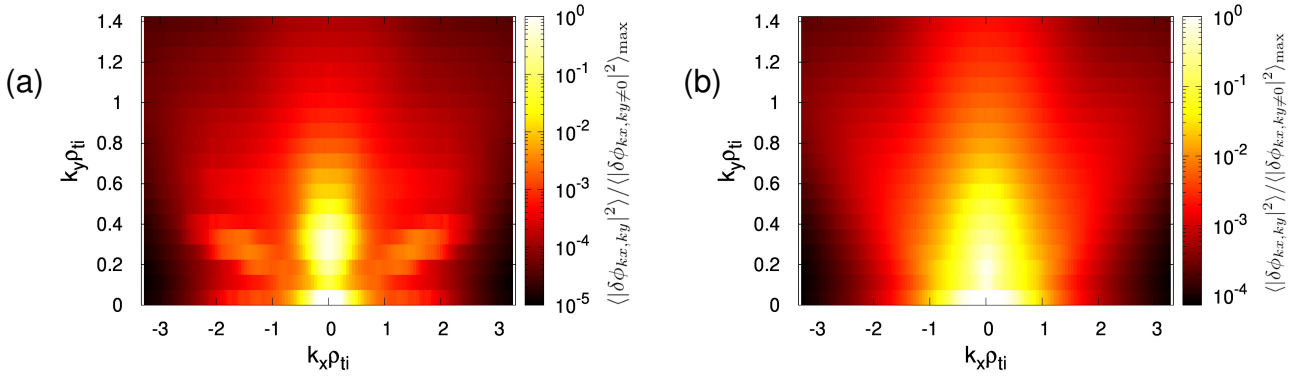

Fig. 2.4: Wavenumber spectra of the turbulent potential fluctuations for (a)$\rho = 0.5, R/L_T = 4.5$, and (b)$\rho = 0.5, R/L_T = 9$

2.3 Construction of NFR using mathematical optimization

Construction of nonlinear functional relation(NFR) between $\mathcal{T}$, $\mathcal{Z}$, and $\chi_{\rm i}$, which accurately reproduce the nonlinear gyrokinetic simulation results, is discussed in this section. Three types of the functional forms $F^{\rm QL}$, $F^{\rm NFR1}$, and $F^{\rm NFR2}$ for the NFR are examined.

First, we consider a functional form $F^{\rm QL}$ that is similar to the quasi–linear approximation [cf. Eq.(2.3)]. $F^{\rm QL}$ is a simple regression to express the turbulent

thermal diffusivity $\chi_{\rm i}/\chi_{\rm i}^{\rm GB}$ only by $\mathcal{T}$, which is defined as

$$\frac{\chi_{\rm i}}{\chi_{\rm i}^{\rm GB}} \sim F^{QL}(\mathcal{T}) = C_1 \mathcal{T}^{\alpha}, \tag{2.4}$$

where C_1 and α correspond to the regression parameters to be determined. The relationship between $\mathcal{T}$ and $\chi_{\rm i}/\chi_{\rm i}^{\rm GB}$ as shown in Fig. 2.5 is useful to determine the regression parameters. As is seen in the figure, there is the refractive behavior at $\chi_{\rm i}/\chi_{\rm i}^{\rm GB} \sim 2.5$, which changes the exponent α remarkably. Indeed, when the simulation data is classified as the near– and far-marginal cases with the boundary of $\chi_{\rm i}/\chi_{\rm i}^{\rm GB} \sim 2.5$, two exponents are evaluated as $\alpha = 0.943$ and $\alpha = 0.608$ for the near– and far–marginal cases, respectively [shown by the two straight lines in light–green(near–marginal) and magenta(far-marginal) in the Fig. 2.5]. It is, therefore, hard to reproduce $\chi_{\rm i}/\chi_{\rm i}^{\rm GB}$ over a wide parameter range including near– and far–marginal ITG stability by using the functional form of Eq.(2.4) with only turbulence potential intensity $\mathcal{T}$. Indeed, as will be discussed later in Tab. 3.5, relatively larger regression error is found for $F^{\rm QL}$ with $C_1 = 0.208$ and $\alpha = 0.733$.

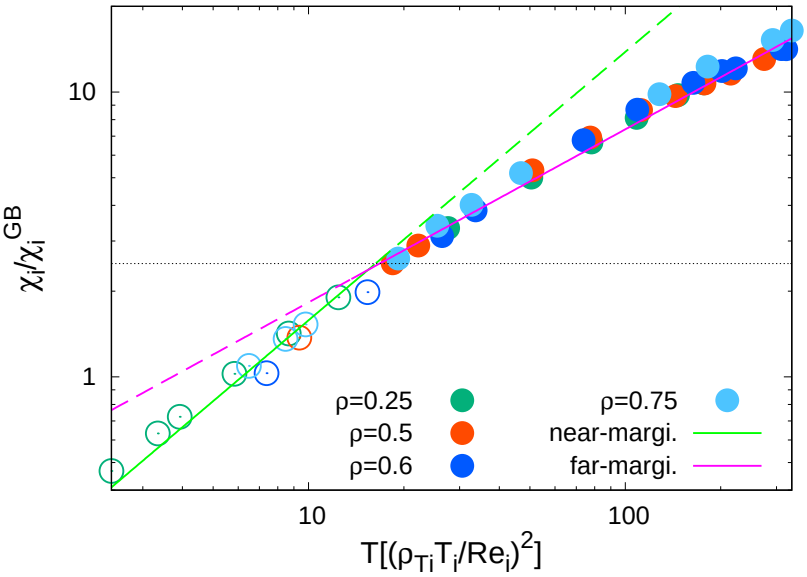

Fig. 2.5: Relation of turbulent potential intensity $\mathcal{T}$ and the turbulent heat diffusivity $\chi_{\rm i}/\chi_{\rm i}^{\rm GB}$ calculated by gyrokinetic simulations.

On the other hand, the strong correlation between $\mathcal{Z}/(\mathcal{T}+\mathcal{Z})$ and $\chi_{\rm i}/\chi_{\rm i}^{\rm GB}$ is shown in Figs. 2.3(a) and 2.3(b) motivate us to consider another type of the functional form, which is applicable for both near- and far-marginal cases. Here, two nonlinear functional forms of $F^{\rm NFR1}$ and $F^{\rm NFR2}$ are defined as follows:

$$\frac{\chi_{\rm i}}{\chi_{\rm i}^{\rm GB}} \sim F^{\rm NFR1}(\mathcal{T},\mathcal{Z}) = \frac{C_1\mathcal{T}^{\alpha}}{1+C_2(\mathcal{Z}^{\beta}/\mathcal{T})}, \tag{2.5}$$

$$\frac{\chi_{\rm i}}{\chi_{\rm i}^{\rm GB}} \sim F^{\rm NFR2}(\mathcal{T},\mathcal{Z}) = \frac{C_1\mathcal{T}^{\alpha}}{1+C_2(\mathcal{Z}/\mathcal{T})^{\beta}}, \tag{2.6}$$

where the zonal flow intensity is explicitly incorporated. Note that the choice of functional forms are not unique, but the above forms still satisfy the fundamental

phenomenological requirements of

$$
\begin{aligned}
F^{\mathrm{NFR1,2}}(\mathcal{T},\mathcal{Z}) &\geq 0, \\
\lim_{\mathcal{T}\to 0} F^{\mathrm{NFR1,2}}(\mathcal{T},\mathcal{Z}) &= 0, \\
\lim_{\mathcal{T}\to \infty} F^{\mathrm{NFR1,2}}(\mathcal{T},\mathcal{Z}) &= F^{\mathrm{QL}}(\mathcal{T}), \\
\lim_{\mathcal{Z}\to 0} F^{\mathrm{NFR1,2}}(\mathcal{T},\mathcal{Z}) &= F^{\mathrm{QL}}(\mathcal{T}), \\
\lim_{\mathcal{Z}\to \infty} F^{\mathrm{NFR1,2}}(\mathcal{T},\mathcal{Z}) &= 0.
\end{aligned}
\tag{2.7}
$$

Here, $(C_1, C_2, \alpha, \beta)$ in Eq.(2.5) and (2.6) are the regression parameters to be determined such that the NFR reproduces the nonlinear gyrokinetic simulation data. F^{NFR1} is inspired by the previous research [30] corresponding to the model for the far-marginal parameter regime. In this study, a more generalized form is considered, where the exponent of the second term of the denominator is changed from the fixed value of $1/2$ used in Ref. [30] to a variable β. A slightly modified form of F^{NFR2} is also considered to treat more explicitly the impact of intensity ratio of $\mathcal{Z}/\mathcal{T}$ in the denominator. For both functional forms, the second term in the denominator plays a role in describing the transport suppression effect by the zonal–flows, where the importance of the relative zonal–flow intensity in near–marginal cases has been demonstrated in Sec. 2.2.

The regression error σ to evaluate the reproduction accuracy is defined by the arithmetic average of the root–mean–square deviations as follows:

$$
\sigma = \sqrt{\frac{1}{n}\sum_{j=1}^{n}\left(\frac{F(\mathcal{T}_j,\mathcal{Z}_j)}{\chi_{\mathrm{i},j}/\chi_{\mathrm{i}}^{\mathrm{GB}}} - 1\right)^2}, \tag{2.8}
$$

where F means the nonlinear function shown in Eqs. (2.4)–(2.6) with no explicit labels. The total data number and the data index are expressed by n and j, respectively. The identification of the NFR to minimize σ is equivalent to the problem of finding the optimal regression parameters $(C_1, C_2, \alpha, \beta)$. An extremal value of

σ is given by the solution of a non–convex mathematical optimization problem, where the word "solution" hereafter means the optimal parameters in F^{NFR1} and F^{NFR2}.

Since the regression error $\sigma = \sigma(C_1, C_2, \alpha, \beta)$, which is the objective function in the context of mathematical optimization, is a nonlinear multi–modal function in the 4–dimensional parameter space, a lot of local minima exists in general. Then, depending on the choice of the initial condition, gradient–descent–based searching algorithms often lead to the trapping by a single local minimum. Figure 2.6(a) shows the example of the initial–value scan with respect to C_1 and C_2, where the contour indicates the different converged values of σ. The existence of several local minima is also emphasized by the histogram $P(\sigma)$ shown in Fig. 2.6(b), indicating a multi–modal distribution. Note that the initial values for β and α are fixed to $\beta_0 = 0$ and $\alpha_0 = 0$ in this visualization, where the subscript " 0 " means the initial value.

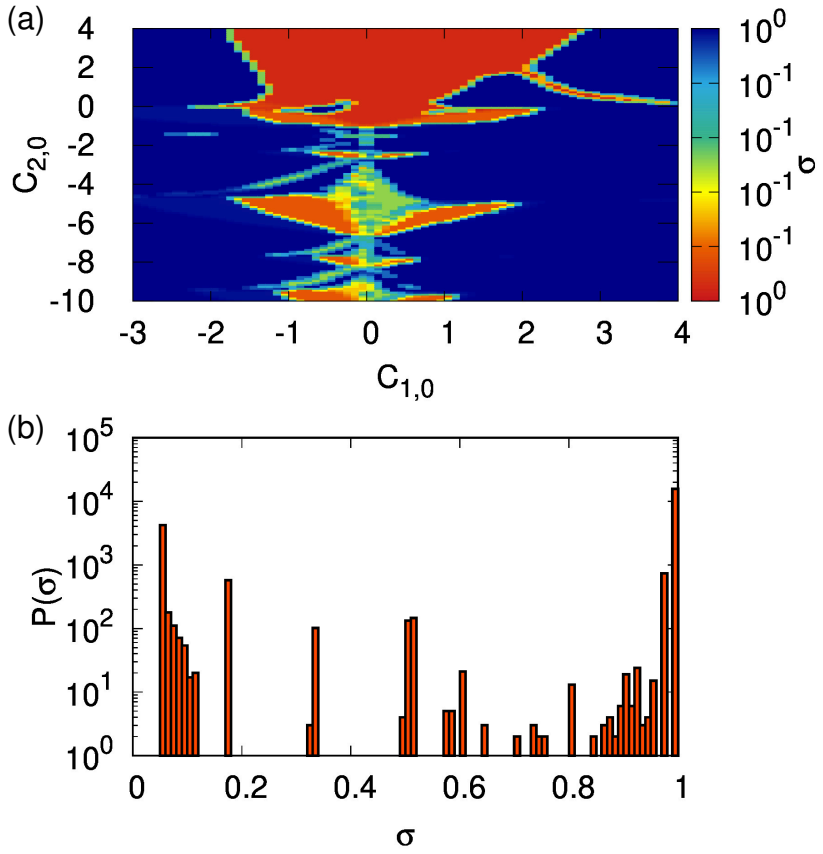

Fig. 2.6: (a)Visualization of the existence of multiple local minima at $(C_{1,0}, C_{2,0})$ with $\alpha_0 = \beta_0 = 0$ fixed. The variations of color correspond to each local optimal solution. (b)Histogram of σ for the $(C_{1,0}, C_{2,0})$ subspace.

In order to search the high dimensional solution space as broadly as possible, systematic scans of the initial values should be performed. However, the discretized grid scan for $(C_{1,0}, C_{2,0}, \alpha_0, \beta_0)$ requires huge computational costs even for the 4-dimensional cases. Thus, we introduce a technique to scan a broader parameter range while reducing computational costs. Here, 6 possible combinations of the 2–dimensional initial–value subspaces of $(C_{1,0}, \alpha_0)$,$(C_{1,0}, \beta_0)$, $(C_{1,0}, C_{2,0})$, $(C_{2,0}, \alpha_0)$, $(C_{2,0}, \beta_0)$, and (α_0, β_0), which are chosen from the original parameters, are numerically scanned. The other remaining 2 initial values are fixed as

$(C_{1,0}, C_{2,0}, \alpha_0, \beta_0) = (1, 1, 0, 0)$. The numerical scan of each initial value set is performed in the condition of 200×200 meshes for $-1 \leq \alpha_0 \leq 1$, $-1 \leq \beta_0 \leq 1$, $-10 \leq C_{1,0} \leq 10$, and $-10 \leq C_{2,0} \leq 10$. Then, the best optimal solution $(C_1, C_2, \alpha, \beta)$ and σ are selected from 6 results of the 2-dimensional scans. The present searching scheme performs the scans in a broader parameter space, but not whole 4–dimensional space. Thus, the optimal solution may not be necessarily a unique global solution.

The mathematical optimization algorithm is similar to Levenberg-Marquardt method [50, 51] which combines gradient descent method and Gauss–Newton method. Although the Hessian matrix is approximated by using the Jacobian matrix in Levenberg-Marquardt method, our algorithm directly calculates the Hessian matrix to hold the fast convergence near the local minimum. Then, the Newton method is used if the Hessian matrix is positive definite. Otherwise, the steepest descent method is applied. Typically, 1.4×10^9 steps are needed for one calculation.

The optimal solution $(C_1, C_2, \alpha, \beta)$ and σ for three nonlinear functional forms F^{QL}, F^{NFR1}, and F^{NFR2} are summarized in Tab. 2.2. One finds the smallest regression error of 0.0569 for F^{NFR1}. As shown in Figs. 2.7(a) and 2.7(b), the reproduction accuracy of $\chi_{\mathrm{i}}/\chi_{\mathrm{i}}^{\mathrm{GB}}$ is examined, where the estimation by NFR is compared to the nonlinear gyrokinetic simulation results shown in the horizontal axis. The deviation from $\chi_{\mathrm{i}}/\chi_{\mathrm{i}}^{\mathrm{GKV}} = 1$ in the vertical axis indicates the magnitude of local errors. It is clarified from the comparison between F^{QL} and $F^{\mathrm{NFR1,2}}$ that the explicit treatment of zonal–flow potential intensity is crucial for improving the reproduction accuracy of the NFR. In addition, we found that the form of intensity ratio of $\mathcal{Z}$ to $\mathcal{T}$ in the denominator of NFR has a large impact on the regression error. It is emphasized that $\sigma = 0.0569$ for F^{NFR1} is more than 2.79 times smaller than that in the previous work[$\sigma = 0.159$(Ref. [30]), 0.12(Ref. [31]), 0.15(Ref. [32]), 0.30(Ref. [34])], and is valid for wider parameter range including the near– and far–marginal linear ITG stability.

Table 2.2: Optimal regression parameters and the regression errors.

parameter	F^{QL}	F^{NFR1}	F^{NFR2}
C_1	0.208	0.485	0.264
C_2	-	1.30	0.0142
α	0.733	0.611	0.732
β	-	0.243	1.37
σ	0.178	0.0569	0.133

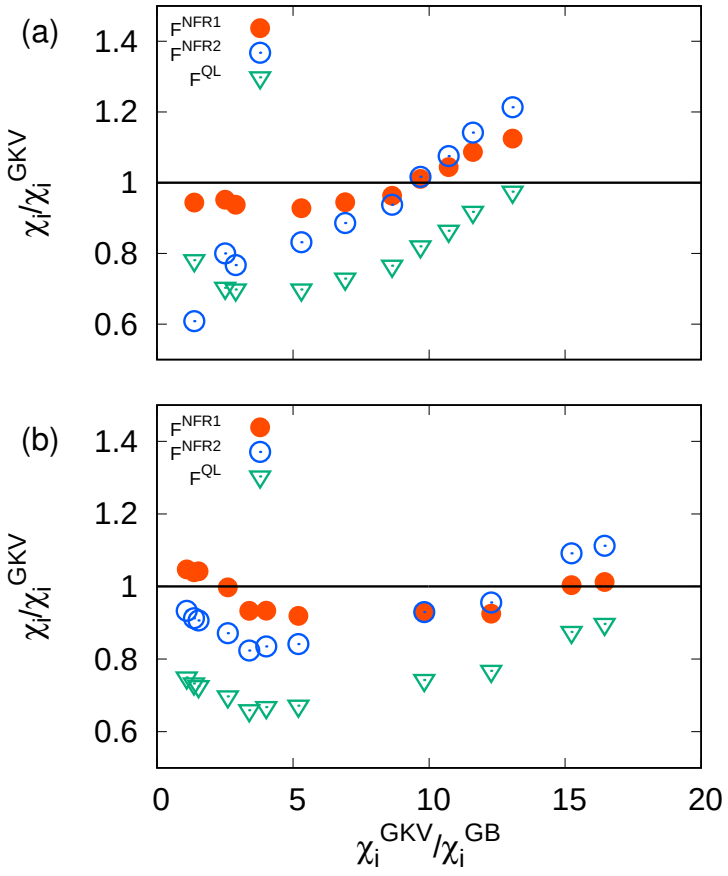

Fig. 2.7: Comparison between the heat diffusivity approximated by NFR(shown by χ_{i}) and the gyrokinetic simulation results(shown by χ_{i}^{GKV}) at (a)$\rho = 0.5$ and (b)$\rho = 0.75$. The deviation from line $\chi_{\mathrm{i}}/\chi_{\mathrm{i}}^{\mathrm{GKV}} = 1$ indicates the local error.

2.4 Impact of zonal–flow effects

As is shown in Tab. 3.5, the regression error of F^{NFR1} is smaller than that of F^{NFR2}, where the variation of the zonal–flow potential intensity $\mathcal{Z}$ in the denominator is slightly different. In this section, the impact of the intensity ratio of $\mathcal{Z}$ to $\mathcal{T}$ on the regression accuracy is examined in more detail to find the reason why F^{NFR1} is more accurate. This enables us to find further optimal parameters. To this end, we define F^{NFR3} as follows:

$$\frac{\chi_{\mathrm{i}}}{\chi_{\mathrm{i}}^{\mathrm{GB}}} \sim F^{\mathrm{NFR3}}(\mathcal{T}, \mathcal{Z}) = \frac{C_1 \mathcal{T}^{\alpha}}{1 + C_2 (\mathcal{Z}^{\xi}/\mathcal{T})^{\beta}}, \tag{2.9}$$

where the additional parameter ξ is introduced. Using ξ, F^{NFR1} and F^{NFR2} are reproduced by setting $\xi = 0.243$ with $\beta = 1$ and $\xi = 1$ with $\beta = 1.37$, respectively, so that F^{NFR3} is regarded as a combined from of F^{NFR1} and F^{NFR2}.

Figure 2.8 shows the regression error of F^{NFR3} as a function of ξ, where σ and the other 4 parameters $(C_1, C_2, \alpha, \beta)$ for given ξ are determined by the same method in Sec. 2.3. One finds a nonlinear ξ-dependence of the regression error in the domain of $0 < \xi \leq 1$. Even though the regression error for F^{NFR1} is enough small compared to that for F^{NFR2}, a slightly more optimal solution at $\xi = 0.2$ is identified, where $\sigma = 0.0527$.

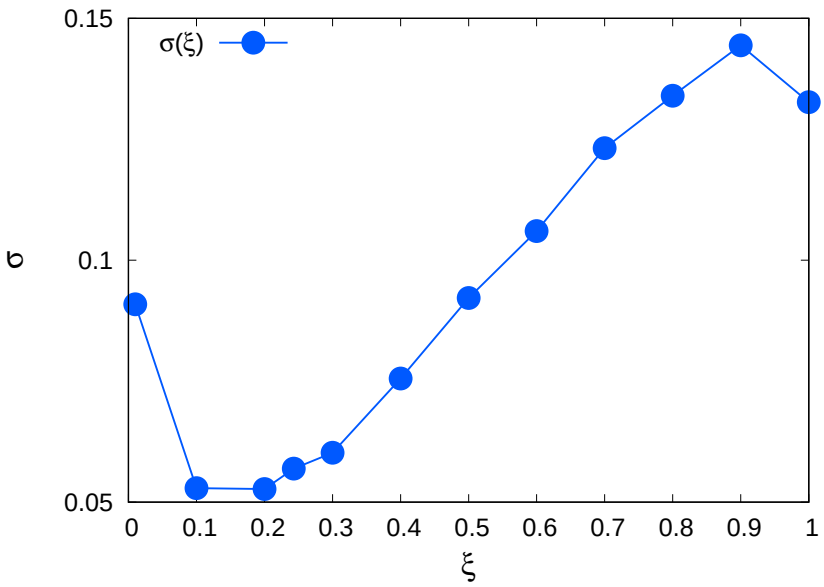

Fig. 2.8: Dependence of the error for F^{NFR3} on ξ, where the cases with $\xi = 0.243$ and $\xi = 1$ correspond to F^{NFR1} and F^{NFR2}, respectively.

As can be seen in Eq. (2.9), the parameter ξ characterizes the relative magnitude of $\mathcal{Z}$ in the intensity ratio of $\mathcal{Z}$ to $\mathcal{T}$. Indeed, Fig. 2.8 suggests the importance of considering the appropriate ξ. By introducing $\Lambda \coloneqq \mathcal{Z}^{\xi}/\mathcal{T}$, the parameter dependence of Λ for large– and small–σ is compared. This can clarify the non–negligible physics that improves the accuracy of the NFR. Here, we choose $\xi = \{0.1, 0.2, 0.243\}$ and $\xi = \{0.8, 0.9, 1\}$ as the representative subsets for the cause with small– and large–σ, respectively.

Figures 2.9(a) and 2.9(b) show Λ for the two subsets as a function of the temperature gradient R/L_T. It is demonstrated that the strongly decaying characteristic appears for the subset of $\xi = \{0.1, 0.2, 0.243\}$ with small σ, while nearly flat behavior for $R/L_T > 5$ is observed for the subset of $\xi = \{0.8, 0.9, 1\}$ with larger σ. Then, we can discuss more quantitatively the different behavior of Λ for the various ξ, by assuming $\Lambda \propto (R/L_T)^{-\eta}$. The fitting exponent η is evaluated as ~ 4.5 for high accuracy cases in Fig.2.9(a), and as ~ 1.5 for low accuracy cases

in Fig.2.9(b). The tendency in the former cases with the small regression error is qualitatively consistent with the nonlinear simulation results shown in Fig. 2.3(b), indicating that the intensity of relative zonal flow becomes significant in the near–marginal regime with the Dimits-shift. On the other hand, for the latter cases with larger errors, the nearly flat R/L_T-dependence of Λ, i.e., $\Lambda \sim \mathrm{const.}$, implies that these nonlinear functional relations are effectively equivalent to the quasi–linear form of Eq.(2.4). Indeed, the regression errors for $\xi = \{0.8, 0.9, 1\}$ are similar to that for F^{QL}, where $C_1 \sim 0.2$, $\alpha \sim 0.7$, and $C_2 \sim 0$. These observations emphasize the importance of capturing steep behaviors in Λ around the critical gradient for improing the accuracy of NFR.

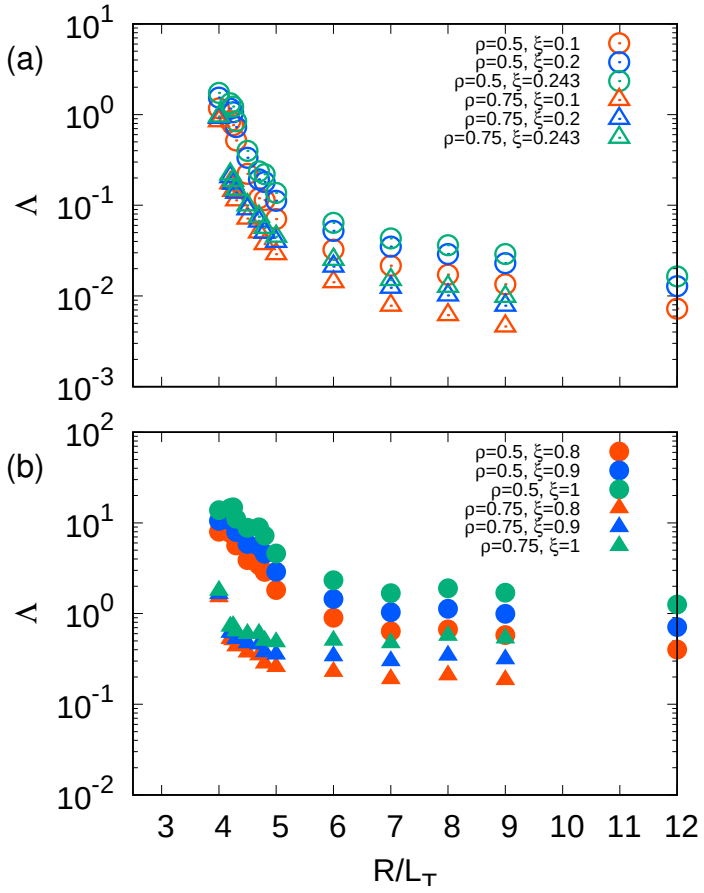

Fig. 2.9: R/L_T-dependence of the intensity ratio $\Lambda = \mathcal{Z}^{\xi}/\mathcal{T}$ in the subsets of (a)$\xi = \{0.1, 0.2, 0.243\}$ in small–σ and (b)$\xi = \{0.8, 0.9, 1\}$ in large–σ.

2.5 Verification of regression accuracy

In the previous section, the most optimal NFR was identified. The functional form is same as Eq.(2.9) where $(C_1, C_2, \alpha, \beta, \xi) = (0.602, 2.01, 0.571, 0.898, 0.2)$ and the regression error $\sigma = 0.0527$. By using the nonlinear simulation data for $\rho = 0.25,\ 0.5,\ 0.6,\ \text{and}\ 0.75$, the verification of reproduction accuracy is carried out to examine the versatility of radial direction and temperature gradient. Note that, the data for $\rho = 0.25$ and $\rho = 0.6$ are not included in the present regression for the NFR, so that we can evaluate the prediction capability of NFR as well.

Figure 2.10 shows the turbulent heat diffusivity as a function of the temperature gradient R/L_T, where the estimations by the NFR are compared with the gyrokinetic simulation results. It is found that the NFR well reproduces the simulation results for $\rho = 0.25$ and $\rho = 0.6$ with the prediction error of $\sigma = 0.0658$ and $\sigma = 0.0782$, as well as the cases for $\rho = 0.5$ and $\rho = 0.75$. In order to verify the accuracy in near-marginal region, the Dimits-shift widths in the NFR and gyrokinetic simulation are compared. The Dimits–shift widths evaluated by the NFR are $\Delta(R/L_T) = 0.868$ at $\rho = 0.5$, $\Delta(R/L_T) = 0.294$ at $\rho = 0.75$, and $\Delta(R/L_T) = 0.888$ at $\rho = 0.25$. These results well reproduce the gyrokinetic simulation results $\Delta(R/L_T) = 0.861$(at $\rho = 0.5$), 0.296(at $\rho = 0.75$), and 0.9(at $\rho = 0.25$), respectively, as discussed in Sec. 2.2. From these results, the accuracy and versatility of the NFR covering near- and far-marginal ITG stability for the several radial positions are demonstrated.

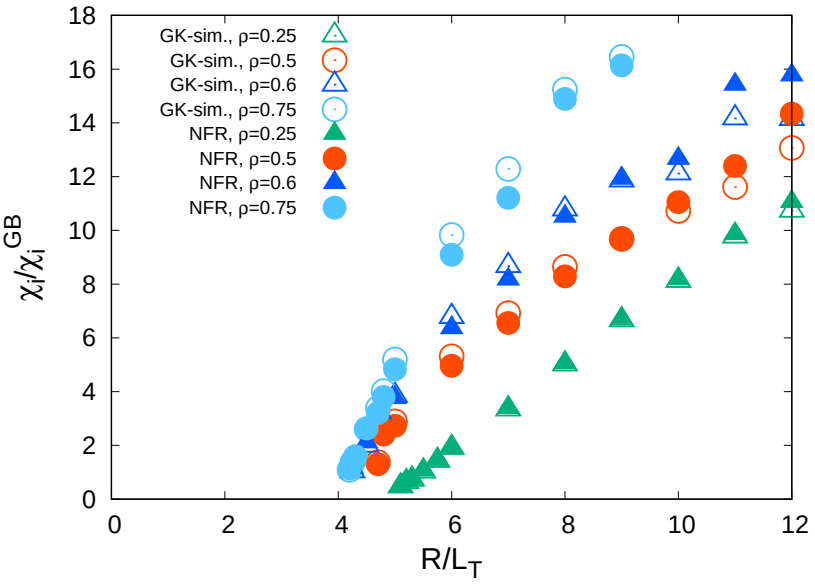

Fig. 2.10: Comparison between NFR and the gyrokinetic simulation results for $\chi_{\rm i}$ at three different radius positions, where the data for $\rho = 0.25$ and $\rho = 0.6$ are not used in the regression for NFR.

To verify the applicability of NFR in slightly more collisional cases [10], the collisionality ν^* is changed under the conditions of $\rho = 0.5$ and $R/L_T = 4.5$, where $\nu^* = 0.0824, 0.109, 0.162$ is considered. Figure 2.11(a) shows the heat diffusivity and the relative zonal–flow intensity for each collisionality. As collisionality increases, the heat diffusivity increases while the relative zonal–flow intensity decreases. The collisional decay of zonal flows and enhanced transport have been reported in several earlier works [52]. Figure 2.11(b) shows the results of applying the NFR to the present slightly collisional cases. It is demonstrated that the accuracy of the present NFR gradually decreases toward the collisional regime, but still keeps a reasonable reproductivity. Such an insensitive feature is attributed to the fact that the statistically averaged quantities $\mathcal{T}$ and $\mathcal{Z}$ in which the various parameter dependencies like the collisionality and configuration parameters do not appear explicitly in the functional form of the NFR. Hereafter,

we focus on the turbulent transport in the weakly collisional regime, where the degraded accuracy is negligibly small.

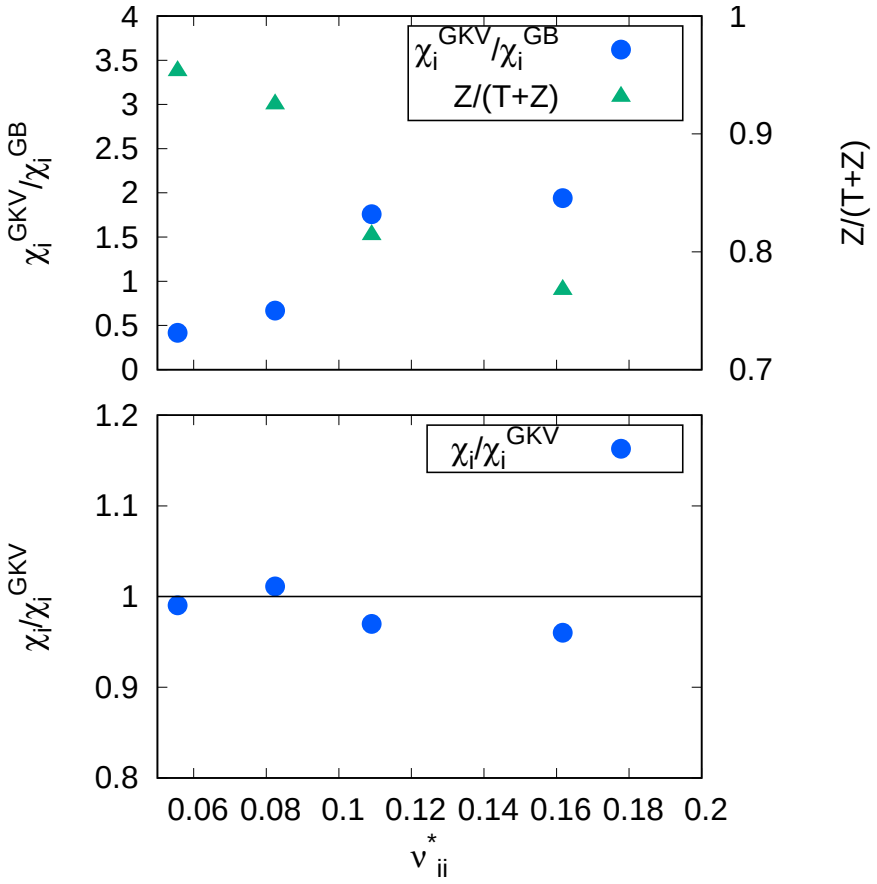

Fig. 2.11: (a)Collisionality dependence of the heat diffusivity $\chi_{\rm i}^{\rm GKV}/\chi_{\rm i}^{\rm GB}$ and the relative zonal–flow intensity $\mathcal{Z}/(\mathcal{T}+\mathcal{Z})$. (b)The regression error of applying the NFR to obtained data. The deviation from $\chi_{\rm i}/\chi_{\rm i}^{\rm GKV}=1$ indicates the local error.

2.6 Robustness of regression parameters in NFR

The parameter ξ, which indicates the magnitude of the zonal–flow contribution, should also be a free continuous parameter. To verify the robustness of

optimal regression parameters in the NFR against the case to include ξ as another continuous variable in first place, the five–dimensional optimization for $(C_1, C_2, \alpha, \beta, \xi)$ is examined. The functional form is same as Eq. (2.9), and mathematical optimization is performed by using techniques described in Sec. 2.3. We found that the optimal regression parameters and the regression error are $(C_1, C_2, \alpha, \beta, \xi) = (0.500, 1.06, 0.595, 0.854, 0.201)$ and $\sigma_{\rm NFR} = 0.0778$, respectively. Althogh a slighted difference appears in C_1, and C_2, the overall accuracy of reproduction by the NFR does not degrade, as shown in Fig. 2.12. From this figure, one finds the robustness of the optimal regression parameters in the present NFR.

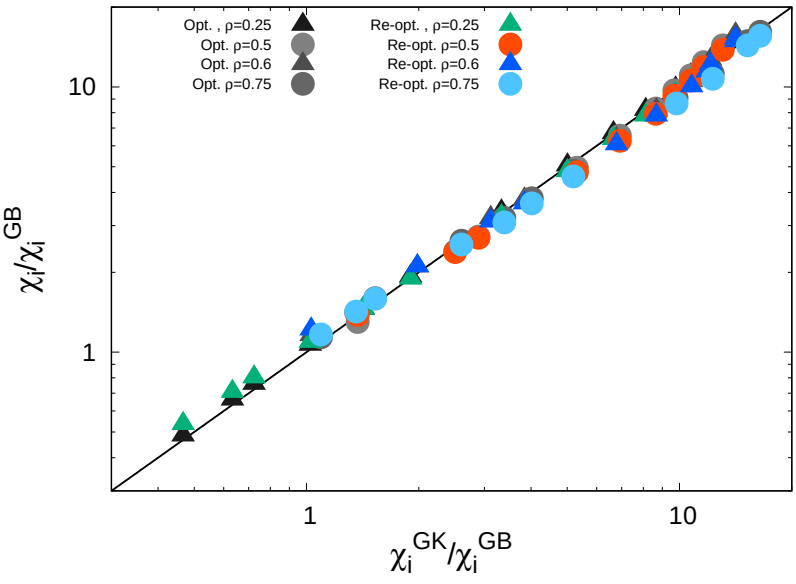

Fig. 2.12: Turbulent heat diffusivity estimated by NFR(shown by $\chi_{\rm i}$) with ξ as an additional optimization variable(color plot). Gray plot is the original case of NFR identified in Sec. 2.3.

Chapter 3

Turbulent transport modeling based on NFR

3.1 Introduction

In general, quantitative analysis and prediction of turbulent transport using gyrokinetic models requires a large computational cost. Since the accurate predictions of kinetic profile formations can determine the burning efficiency and its control in fusion plasmas, turbulent transport models, which can quickly be evaluated and be applicable to a wide parameter range, play a crucial role in integrated transport simulation studies. There are many earlier works on constructing the simplified turbulent transport models in a wide variety of approaches, e.g., quasi-linear gyrokinetic and gyrofluid modeling [23–27]. Some works have devoted to include the effects of multi-scale fluctuations [28], mean $\boldsymbol{E} \times \boldsymbol{B}$ flow shear [29], and turbulence nonlinearity [30–34, 53] cross–field fluxes in the edge and scrape–off layer (SOL) region [54, 55] had also been modeled. Although the local transport approximation in terms of the turbulent diffusivity is often discussed, the importance of non–local and non-diffusive nature in a global turbulence system has also been revealed in several earlier works [10, 56–58]. The modeling studies with deep neural networks [20, 21, 36–40], which allow to rapidly estimate the tur-

bulent diffusivities from the several known physical parameters, recently become more active.

In the previous chapter, by means of the nonlinear gyrokinetic turbulence simulations, a novel regression model that describes a nonlinear functional relation(NFR) between the turbulent heat diffusivity, the turbulence intensity, and the zonal-flow intensity was proposed. The NFR is identified by using mathematical optimization techniques to find the optimal parameter sets as the extremum point in the multi–dimensional solution space. Then, the NFR successfully reproduced the turbulent diffusivity in the nonlinear gyrokinetic simulations for a wide range of physical parameters and the radial domains, including near– and far–marginal ITG stability. However, it should be noted that the NFR is a regression model which still needs the nonlinear simulation data of the turbulence and zonal–flow intensities. Further modeling is thus necessary to reduce the NFR to the turbulent transport model that can be applied to the integrated transport simulations.

To this end, we propose an extended modeling to realize a novel simplified turbulent transport model [59]. Here, the turbulence intensity and the zonal-flow intensity are represented by nonlinear functions of the instability growth rate and the zonal-flow decay time obtained from the "linear" gyrokinetic simulations, whose computational costs are 1/200 times less than the typical nonlinear simulations. Particularly, the turbulence suppression by the zonal flows and its temperature-gradient dependence, which have been ignored in earlier works [30–34], are incorporated. The optimal parameters in the nonlinear model functions are determined by using the mathematical optimization technique which is partly extended from that used in the previous chapter.

The rest of this chapter is organized as follows. In Sec. 3.2, we define the physical quantity to be used in the modeling. The turbulence intensity and zonal–flow intensity are modeled in Sec. 3.3 and 3.4, respectively. Finally, they are combined to a simplified transport model based on the NFR in Sec. 3.5.

3.2 Fundamental variables for simplified modeling

In the previous chapter, a good reproduction accuracy of the NFR was demonstrated, where the turbulent heat diffusivity is estimated by Eq. (2.9). Here, the additional modeling for the $\mathcal{T}$ and $\mathcal{Z}$ appearing in Eq. (2.9) is proposed for constructing a novel turbulent transport model.

Following earlier works [30–34], $\mathcal{T}$ and $\mathcal{Z}$ are approximated by the quantities obtained only by the "linear" gyrokinetic simulations, such as the linear growth rate γ of the ITG instability and the linear response function of zonal flows $\mathcal{R}_{k_x}(t) \equiv \langle \delta\phi_{k_x,k_y=0}(t)\rangle / \langle \delta\phi_{k_x,k_y=0}(0)\rangle$. The examples of the wavenumber spectrum of γ for several R/L_T parameters and the zonal–flow response function $\mathcal{R}_{k_x}(t)$ for several radial positions are shown in Fig. 3.1 (a) and (b), respectively. For the ITG instability, only the most unstable modes with $k_x = 0$ are considered. For the zonal–flow response, k_x is fixed to $k_x \sim 0.1{\rho_{Ti}}^{-1}$ that is a typical radial scale of zonal flows in the ITG turbulence. Note also that the linear zonal–flow response function does not depend on the temperature and density gradients, but depends on the radial positions. On the other hand, the simulation results[see Fig.2.3 (b)] for nonlinearly–generated zonal flows indicate the strong gradient dependence. Thus, one need a special care of incorporating the gradient dependence to the modeling of the zonal–flow response, but earlier works ignored the gradient dependence.

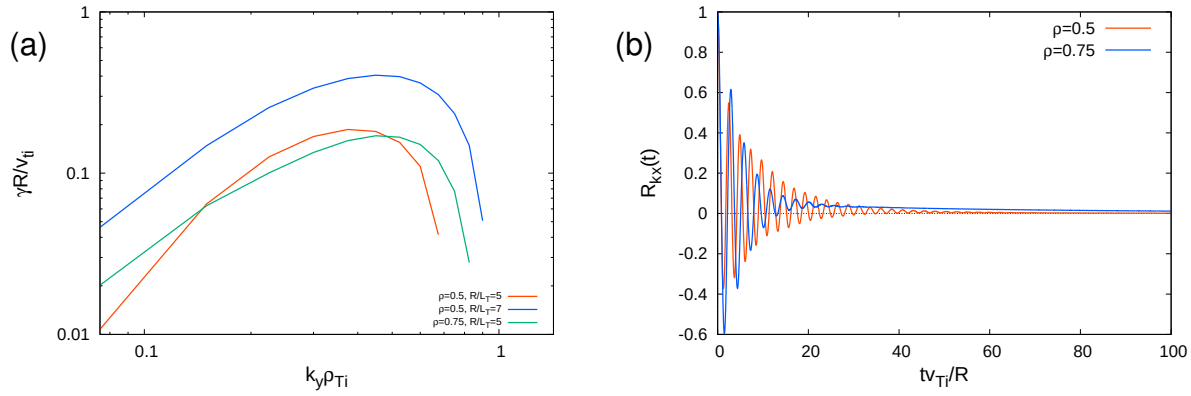

Fig. 3.1: (a)The wavenumber spectra of the ITG instability growth rate γ at the $\rho = 0.5$, 0.75 and (b)zonal–flow response function $\mathcal{R}_{kx}(t)$ at each radial positions, calculated by the linear gyrokinetic simulations.

In order to approximate $\mathcal{T}$ and $\mathcal{Z}$ by the quantities obtained from the linear calculations, the mixing–length diffusivity [53] $\mathcal{L}$ and the zonal–flow decay time $\tau_{\rm ZF}$ are introduced:

$$\mathcal{L} \equiv \sum_{k_y} \frac{\gamma}{{k_y}^2}, \tag{3.1}$$

$$\tau_{\rm ZF} \equiv \int_0^{\tau_{\rm f}(\gamma_{\rm max})} dt\, \mathcal{R}_{k_x}(t), \tag{3.2}$$

where the upper limit of the integral interval $\tau_{\rm f}(\gamma_{\rm max})$ is given by a typical time scale of the turbulence growth and the correlation, i.e., $\tau_{\rm f} = C/\gamma_{\rm max}$ with a constant C. It is noted that, in contrast to $\mathcal{R}_{k_x}(t)$, the zonal–flow decay time $\tau_{\rm ZF}$ is a gradient–dependent quantity through the temperature and density gradient dependence appearing in the maximum ITG growth rate $\gamma_{\rm max}$. Indeed, the R/L_T–dependence found in the nonlinear simulations[Fig. 2.3 (b)] is qualitatively reproduced, as shown in Fig. 3.2 (a), where $C = 10$. For comparison, the gradient-independent $\tau_{\rm ZF}$ used in the earlier works is also displayed by the horizontal lines in the figure. Although $\tau_{\rm f}$ includes a control parameter C, one can see

that, as shown in Fig. 3.2(b), the qualitative characteristic of R/L_T–dependence still holds even for $C = 2.5$. In the present study, $C = 10$ is chosen from the reproduction accuracy point of view.

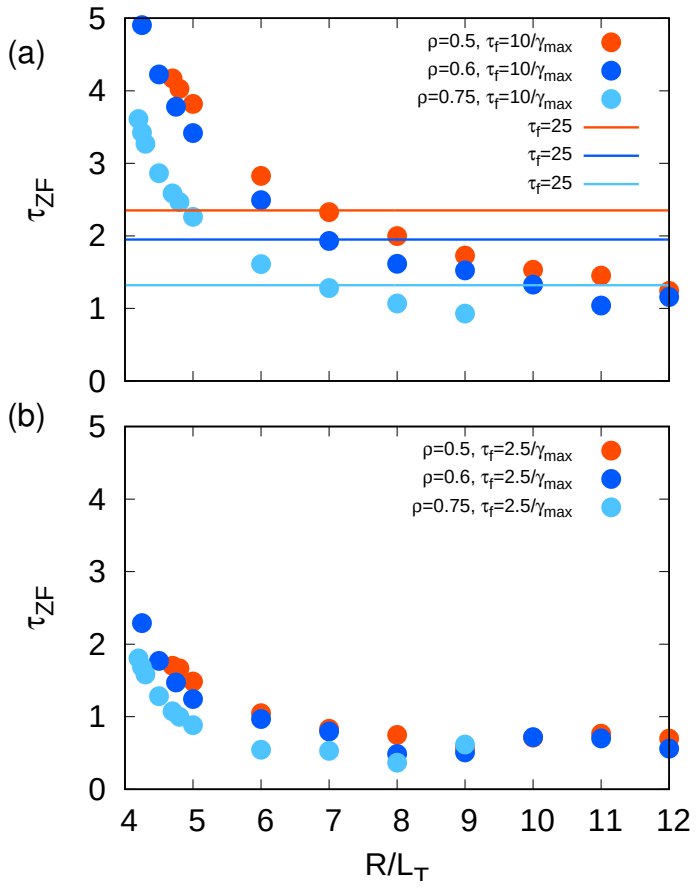

Fig. 3.2: Temperature gradient dependence of zonal–flow decay time $\tau_{\rm ZF} \equiv \int_0^{\tau_{\rm f}} dt \mathcal{R}_{kx}(t)$ (symbols), where $\tau_{\rm f} \equiv C/\gamma_{\rm max}$. (a)$C = 10$ and (b)$C = 2.5$. The horizontal lines in (a) indicate the gradient–independent $\tau_{\rm ZF}$, assumed in earlier works.

3.3 Modeling of turbulence intensity $\mathcal{T}$

A model for the turbulence intensity $\mathcal{T}$ is discussed in this section. It is stressed that the modeling only by $\mathcal{L}$ (or similarly by the linear growth rate γ) is not appropriate particularly for the cases in the near–marginal stability, because

the turbulence intensity $\mathcal{T}$ is influenced by the suppression effects of zonal flows through the nonlinear interactions. Indeed, the distribution of $\mathcal{T}$ in $\mathcal{L}$–$\tau_{\rm ZF}$ space shown by the symbols in Fig. 3.3 indicates a strong dependence on both $\mathcal{L}$ and $\tau_{\rm ZF}$. Especially, in the low–$\tau_{\rm ZF}$ region($\tau_{\rm ZF} < 2$), $\mathcal{T}$ shows a significant decay in comparison to that in high–$\tau_{\rm ZF}$ region($\tau_{\rm ZF} \geq 2$). Therefore, the model function for $\mathcal{T}$ has to reproduce such tendency. Two kinds of the model function in the similar manner for the NFR that satisfies the phenomenological requirements as discussed in the previous chapter is considered. The model functions $f_{\mathcal{T}1}$ and $f_{\mathcal{T}2}$ are defined as:

$$\mathcal{T} \sim f_{\mathcal{T}1}\left(\mathcal{L}, \tau_{\rm ZF}\right) = \frac{C_{\mathcal{T}1}\mathcal{L}^{\alpha_\mathcal{T}}}{1 + C_{\mathcal{T}2}{\tau_{\rm ZF}}^{\beta_\mathcal{T}}}, \tag{3.3}$$

$$\mathcal{T} \sim f_{\mathcal{T}2}\left(\mathcal{L}, \tau_{\rm ZF}\right) = \frac{C'_\mathcal{T}\mathcal{L}^{\alpha'_\mathcal{T}}}{\exp(\beta'_{\mathcal{T}1}{\tau_{\rm ZF}}^{\beta'_{\mathcal{T}2}})}, \tag{3.4}$$

where $(C_{\mathcal{T}1}, C_{\mathcal{T}2}, \alpha_\mathcal{T}, \beta_\mathcal{T})$ and $(C'_\mathcal{T}, \alpha'_\mathcal{T}, \beta'_{\mathcal{T}1}, \beta'_{\mathcal{T}2})$ are regression parameters to be determined. The zonal–flow effects corresponding to the strong decay of $\mathcal{T}$ in the low–$\tau_{\rm ZF}$ region are treated in the form of a rational or an exponential function in $f_{\mathcal{T}1}$ and $f_{\mathcal{T}2}$, respectively.

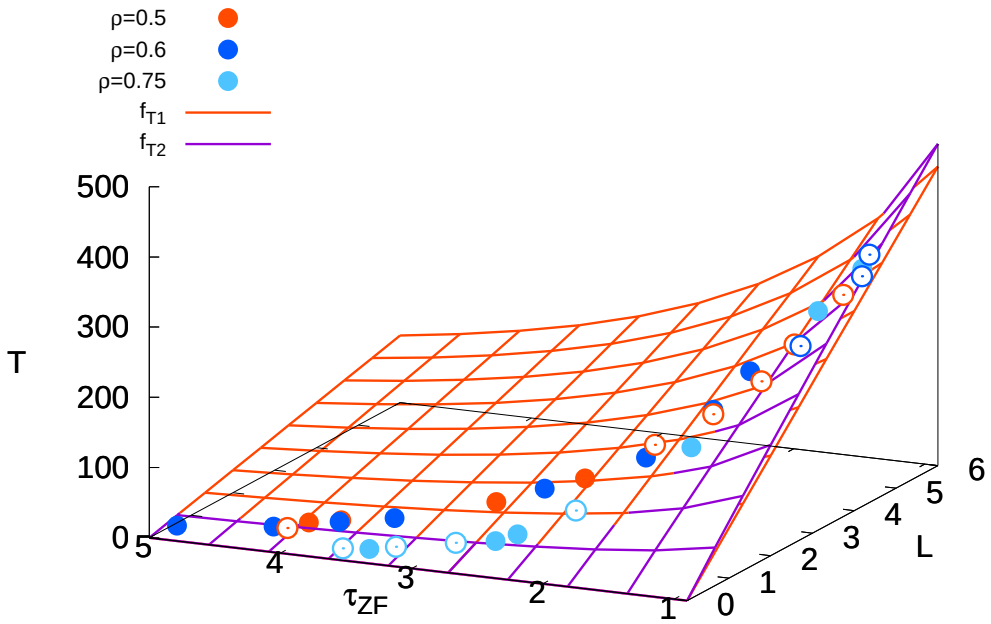

Fig. 3.3: Distribution of $\mathcal{T}$ in $\mathcal{L}$–$\tau_{\rm ZF}$ space, and overplot of the surfaces [Eqs. (3.3) and (3.4)] to reproduce $\mathcal{T}$. The open symbols denote the data points located behind the surfaces.

The optimal parameters are identified by the mathematical optimization in similar way discussed in Sec. 2.3, where the regression error $\sigma_{\mathcal{T}}$ is defined as follows:

$$\sigma_{\mathcal{T}}{}^2 = \frac{1}{n}\sum_j^n \left(\frac{f_{\mathcal{T}}\left(\mathcal{L}_j, \tau_{{\rm ZF},j}\right)}{\mathcal{T}_j} - 1 \right)^2, \tag{3.5}$$

for $f_{\mathcal{T}} = f_{\mathcal{T}1}$ or $f_{\mathcal{T}} = f_{\mathcal{T}2}$. The optimal regression parameters are identified as $(C_{\mathcal{T}1}, C_{\mathcal{T}2}, \alpha_{\mathcal{T}}, \beta_{\mathcal{T}}) = (100, 0.472, 0.996, 1.50)$ and $(C'_{\mathcal{T}}, \alpha'_{\mathcal{T}}, \beta'_{\mathcal{T}1}, \beta'_{\mathcal{T}2}) = (520, 0.970, 1.93, 0.365)$ for $f_{\mathcal{T}1}$ and $f_{\mathcal{T}2}$, respectively, where the regressions error are $\sigma_{\mathcal{T}} = 0.181$ for $f_{\mathcal{T}1}$, and $\sigma_{\mathcal{T}} = 0.179$ for $f_{\mathcal{T}2}$. As shown by the surfaces in Fig.

3.3, either functional form of $f_{\mathcal{T}1}$ or $f_{\mathcal{T}2}$ reasonably reproduces the nonlinear simulation dataset $\mathcal{T}$. Equation (3.4), which has a slightly smaller error, is considered in the followings.

3.4 Modeling of zonal–flow intensity $\mathcal{Z}$

In this section, the modeling for the zonal–flow suppression effect $\mathcal{Z}^{\xi}/\mathcal{T}$ appearing in the NFR[Eq. (2.9)] is presented. From the view point of the similarity to the zonal–flow response function $\mathcal{R}_{k_x}(t)$, the relative zonal–flow intensity $\mathcal{Z}/\mathcal{T}$ [or equivalently $\mathcal{Z}/(\mathcal{T}+\mathcal{Z})$ in Fig. 2.3(b)] is modeled here. Since the parameter ξ is an optimal parameter in the determination of the NFR, the parameter may change for rather different magnetic configuration such as stellarators. Thus, the model function for the zonal–flow suppression effect should not include ξ explicitly. To treat ξ separately, the zonal–flow suppression term in NFR is rewritten as:

$$\begin{aligned} \frac{\mathcal{Z}^{\xi}}{\mathcal{T}} &= \mathcal{T}^{(\xi-1)}\left(\frac{\mathcal{Z}}{\mathcal{T}}\right)^{\xi} \\ &\sim \left[f_{\mathcal{T}2}(\mathcal{L},\tau_{\mathrm{ZF}})\right]^{(\xi-1)}\left[\mathcal{H}(\tau_{\mathrm{ZF}})\right]^{\xi}, \end{aligned} \tag{3.6}$$

where Eq. (3.4) is used for $\mathcal{T}^{(\xi-1)}$. Also, $\mathcal{H}(\tau_{\mathrm{ZF}})$ is an additional model function to approximate $\mathcal{Z}/\mathcal{T}$ by τ_{ZF}. Figure 3.4 shows the relation between τ_{ZF} and $\mathcal{Z}/\mathcal{T}$. It shows that $\mathcal{Z}/\mathcal{T} \sim \mathrm{const.}$ in the region of $\tau_{\mathrm{ZF}} < 2$, and increases with τ_{ZF} in the region of $\tau_{\mathrm{ZF}} \geq 2$. From this observation, the functional form of $\mathcal{H}$ is defined as follows:

$$\frac{\mathcal{Z}}{\mathcal{T}} \sim \mathcal{H}(\tau_{\mathrm{ZF}}; C_{\mathcal{Z}1}, C_{\mathcal{Z}2}, \alpha_{\mathcal{Z}}, \beta_{\mathcal{Z}}) = C_{\mathcal{Z}1} + C_{\mathcal{Z}2}\exp\left(\alpha_{\mathcal{Z}}{\tau_{\mathrm{ZF}}}^{\beta_{\mathcal{Z}}}\right). \tag{3.7}$$

In the similar manner for F^{NFR} and $\mathcal{T}$, the optimal parameter are identified as $(C_{\mathcal{Z}1}, C_{\mathcal{Z}2}, \alpha_{\mathcal{Z}}, \beta_{\mathcal{Z}}) = (0.883, 0.0236, 0.140, 2.47)$ with the error $\sigma_{\mathcal{Z}} = 0.354$. A

relatively larger error compared to the modeling for $\mathcal{T}$ is associated with scattered distribution of $\mathcal{Z}/\mathcal{T}$ for $\tau_{\rm ZF} \geq 2$ in Fig. 3.4. On the other hand, a nearly–constant characteristic for the smaller $\tau_{\rm ZF}$ is well described in Eq. (3.7).

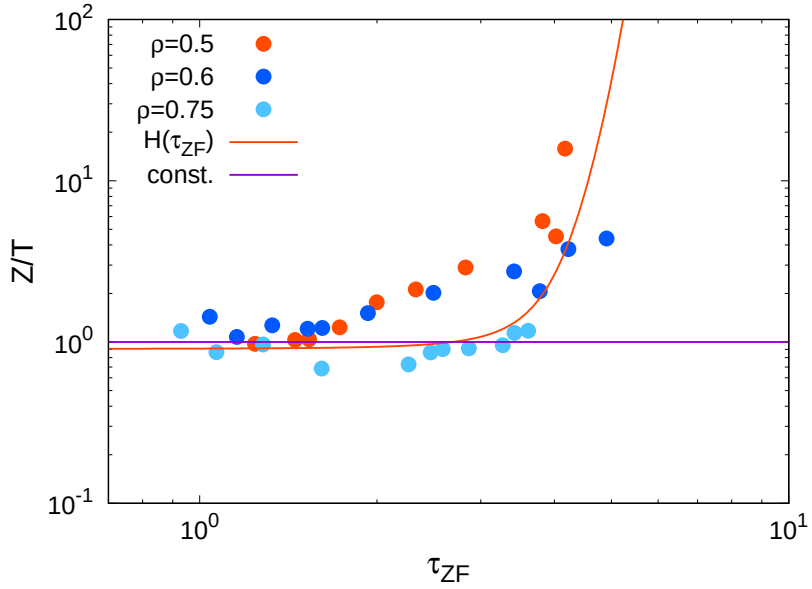

Fig. 3.4: $\tau_{\rm ZF}$–dependence of $\mathcal{Z}/\mathcal{T}$. The model function $\mathcal{H}$ is shown by the curve. The horizontal line means the constant value of 1 for the reference.

3.5 Simplified transport model

Finally, the above modeling for $\mathcal{T}$ and $\mathcal{Z}$ are combined to the NFR in this section. Substituting the model functions Eqs. (3.4) and (3.7) into Eq. (2.9), a new transport model for the ITG driven turbulent heat diffusivity is expressed as follows:

$$\frac{\chi_{\rm i}}{\chi_{\rm i}^{\rm GB}} \sim \frac{\chi_{\rm i}^{\rm model}}{\chi_{\rm i}^{\rm GB}}\left(\mathcal{L}, \tau_{\rm ZF}\right) = \frac{\Theta_1 \mathcal{L}^{\Theta_2} \exp\left(\Theta_3 {\tau_{\rm ZF}}^{\Theta_4}\right)}{1 + \Theta_5 \mathcal{L}^{\Theta_6} \exp\left(\Theta_7 {\tau_{\rm ZF}}^{\Theta_4}\right) \left[\mathcal{H}(\tau_{\rm ZF})\right]^{\Theta_8}}. \tag{3.8}$$

Here, $\{\Theta_i\}$ for $1 \leq i \leq 8$ are the parameters, which were already determined by the combinations of the regression parameters summarized in Tab. 3.1. The model function $\mathcal{H}(\tau_{ZF})$ with $(C_{\mathcal{Z}1}, C_{\mathcal{Z}2}, \alpha_{\mathcal{Z}}, \beta_{\mathcal{Z}})$ is given by Eq. (3.7).

Table 3.1: Parameters in the simplified transport model

Parameter	Expression	Value
Θ_1	$C_1 {C'_{\mathcal{T}}}^{\alpha}$	20.7
Θ_2	$\alpha\alpha'_{\mathcal{T}}$	0.577
Θ_3	$-\alpha\beta'_{\mathcal{T}1}$	-1.15
Θ_4	$\beta'_{\mathcal{T}2}$	0.365
Θ_5	$C_2 {C'_{\mathcal{T}}}^{\beta(\xi-1)}$	0.0127
Θ_6	$\beta\alpha'_{\mathcal{T}}(\xi-1)$	-0.662
Θ_7	$-\beta\beta'_{\mathcal{T}1}(\xi-1)$	1.32
Θ_8	$\beta\xi$	0.172

The regression error of the transport model Eq. (3.8), $\sigma_{\rm model}$, is evaluated as $\sigma_{\rm model} = 0.157$ for the regression datasets($\rho = 0.5$, 0.6, and 0.75), and $\sigma_{\rm model} = 0.211$ for extrapolation dataset($\rho = 0.25$). Figure 3.5 shows the comparison between the newly constructed transport model and the nonlinear gyrokinetic simulations. The result demonstrates that the present transport model has a good accuracy for the turbulent heat diffusivity $\chi_i/\chi_i^{\rm GB}$. The total regression error is similar or less compared to those in the earlier works [$\sigma = 0.129$(Ref. [30]), 0.16(Ref. [31]), 0.20(Ref. [32]), 0.27(Ref. [34])]. It is however emphasized that the present transport model is much improved to be valid for the range of $0.4 < \chi_i/\chi_i^{\rm GB} < 17$ corresponding to wider parameter regions including near- and far-marginal ITG stability. Indeed, as shown by grey symbols in Fig. 3.5, a significant deviation for $\chi_i/\chi_i^{\rm GB} \lesssim 4$ appears when the previously proposed functional form [30] is applied to the datasets in this work. Note again that, the nonlinear turbulent heat diffusiv-

ity $\chi_{\rm i}/\chi_{\rm i}^{\rm GB}$ is reproduced only by linear gyrokinetic calculations with Eq. (3.8), where the computational amount is reduced to $\sim 1/200$ of that in the nonlinear simulations.

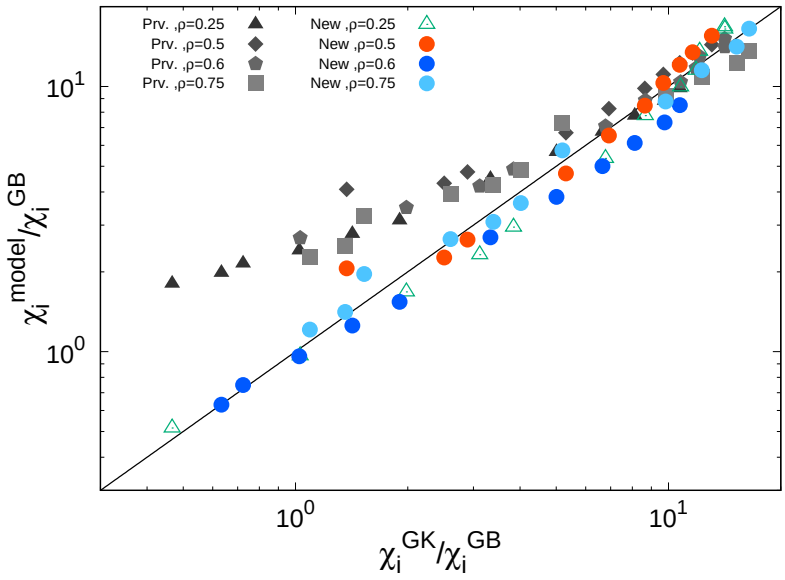

Fig. 3.5: Comparison of the turbulent heat diffusivities between the nonlinear gyrokinetic simulation results $\chi_{\rm i}^{\rm GK}/\chi_{\rm i}^{\rm GB}$ and simplified transport model $\chi_{\rm i}^{\rm model}/\chi_{\rm i}^{\rm GB}$ (colored symbols). The conventional model in the earlier work [30] is displayed by grey symbols. The circle and triangle symbols correspond to the data for regression and prediction, respectively.

An alternative form is also derived by imposing the approximation of $\mathcal{H}(\tau_{\rm ZF}) \sim 1$ when one focuses on the feature of $\mathcal{Z}/\mathcal{T} \sim {\rm const.}$ in low–$\tau_{\rm ZF}$ region (see Fig. 3.4). Such approximation leads to

$$\frac{\chi_{\rm i}}{\chi_{\rm i}^{\rm GB}} \sim \frac{\chi_{\rm i}^{\rm model}}{\chi_{\rm i}^{\rm GB}}(\mathcal{L}, \tau_{\rm ZF}) = \frac{\Theta_1 \mathcal{L}^{\Theta_2} \exp\left(\Theta_3 {\tau_{\rm ZF}}^{\Theta_4}\right)}{1 + \Theta_5 \mathcal{L}^{\Theta_6} \exp\left(\Theta_7 {\tau_{\rm ZF}}^{\Theta_4}\right)}. \tag{3.9}$$

Here, the parameters are the same as Tab. 3.1. The above more simplified form with 7 parameters indicates a slight increase of the regression error $\sigma_{\rm model} = 0.161$ and $\sigma_{\rm model} = 0.280$ for extrapolation dataset($\rho = 0.25$), but still holds a reason-

able applicability to the practical analysis. It is also noted that further extensions are necessary to include the particle transport and electron thermal transport, but the similar ways in Refs. [31–34] can straightforwardly be applicable.

Chapter 4

Co–simulation framework with simplified transport model

4.1 Introduction

In fusion burning plasmas, the confinement performance and the burning efficiency are dominantly governed by the turbulent thermal and mass transport, where the global analysis of kinetic profile formations becomes more crucial than the local analysis of turbulent transport properties. The integrated transport simulation approach(e.g., Refs. [15–17, 60]) is a typical way to address such issues. Also, global full-f gyrokinetic simulations(e.g., Ref. [9–14, 61–63]) are the other powerful approach to elucidate the non-local dynamics of global transport and profile formations in confined plasmas. However, they often require enormous computational costs, and comprehensive studies for the various operation scenarios in burning plasmas are still limited.

As another promising approach is so–called co–simulation framework [64], which is widely utilized to solve fluid–structure interactions in e.g., fluid engineering [65, 66], geophysics [67, 68], and biomedical science [69, 70]. In the co-simulation, several different physical models, coupled each other, are solved in parallel, and the information are mutually exchanged at appropriate frequen-

cies. There is an earlier work on developing the co-simulation framework with a particular focus on turbulent transport in fusion plasmas [71], where the nonlinear local turbulence simulations are directly coupled to 1–dimensional temperature profile solver.

As shown above, the global transport dynamics has extensively been investigated so far from several different aspects, e.g., integrated simulation, global full-f simulation, co-simulation, towards the high–performance plasmas. However, the stationary situations have often been assumed for the macroscopic quantities such as the heating deposition inside the plasma and the confinement magnetic fields.

In the fusion burning plasma, one can expect non-negligible spatio-temporal variations of the heating deposition, plasma current, and confinement magnetic fields, which are mutually coupled through the turbulent transport processes. For instance, the absorption power from the external heating and/or fusion reaction can vary in time, depending on the kinetic profiles (density and temperature profiles) in plasmas. Also, more than about 60% of the total plasma current is supposed to be sustained by the pressure-gradient driven bootstrap current. The variations of the plasma current yield fluctuations in confinement magnetic fields, and consequently the microinstabilities and turbulent transport to determine the kinetic profile evolutions are affected.

In this study, a novel co–simulation framework, AGITO, for global turbulent transport and profile formation is developed by utilizing the simplified transport model in Chap. 3., where the spatio–temporal variation effects of the heating and confinement magnetic fields are incorporated. The basic concept and numerical setup are presented in this chapter, and the first application to practical problems will be discussed in Chap. 5.

The rest of this chapter is organized as follows. In Sec. 4.2, the basic concept of the new co–simulation is presented. The physical models and other numerical schemes used in the co–simulation are described in Sec. 4.3. Finally, some numerical verifications with the stationary heating are shown in Sec. 4.4.

4.2 Concept of AGITO(Alterable Gyrokinetics-Integrated Transport cO-simulation)

As a novel co-simulation framework for the global turbulent transport, an Alterable Gyrokinetics-Integrated Transport cO-simulation(abbreviated as AGITO) is developed, where the dynamical variations of heating and confinement magnetic fields, which have been ignored in earlier works, are taken into account. The highlighted features of AGITO are summarized as follows:

(I) Direct coupling of a 1-dimiensional transport solver TRESS [72], gyrokinetic solver GKV [46], and neoclassical transport solver [73] enables us to calculate the global evolutions of transport and kinetic profiles over the energy confinement time, under the stationary/non-stationary heating and sink profiles.

(II) Fast turbulent transport calculations by the NFR-based simplified transport model presented in Chap. 3, and the combinational usage with fully nonlinear gyrokinetic calculations are possible.

(III) High extensibilities hold by utilizing so–called MPMD(Multiple Program Multiple Data) parallelization, where the separation or further coupling of the other physical effects or simulation codes is easily achieved.

It also should be emphasized that AGITO with the new simplified transport model enables us to evaluate not only turbulent diffusivity $\chi_{\rm i}$ but also zonal–flow related quantities such as $\mathcal{Z}/\mathcal{T}$ or $\tau_{\rm ZF}$. As shown in Fig. 4.1, the several gyrokinetic calculations are discretely located in the radial direction. They evaluate the local turbulent diffusivity at each position, where the instantaneous local density and temperature gradients are used as the input parameters. Then, the evaluated

turbulent diffusivities are transferred to the 1–dimensional global transport solver to compute the time evolution of the pressure profile towards the next time step.

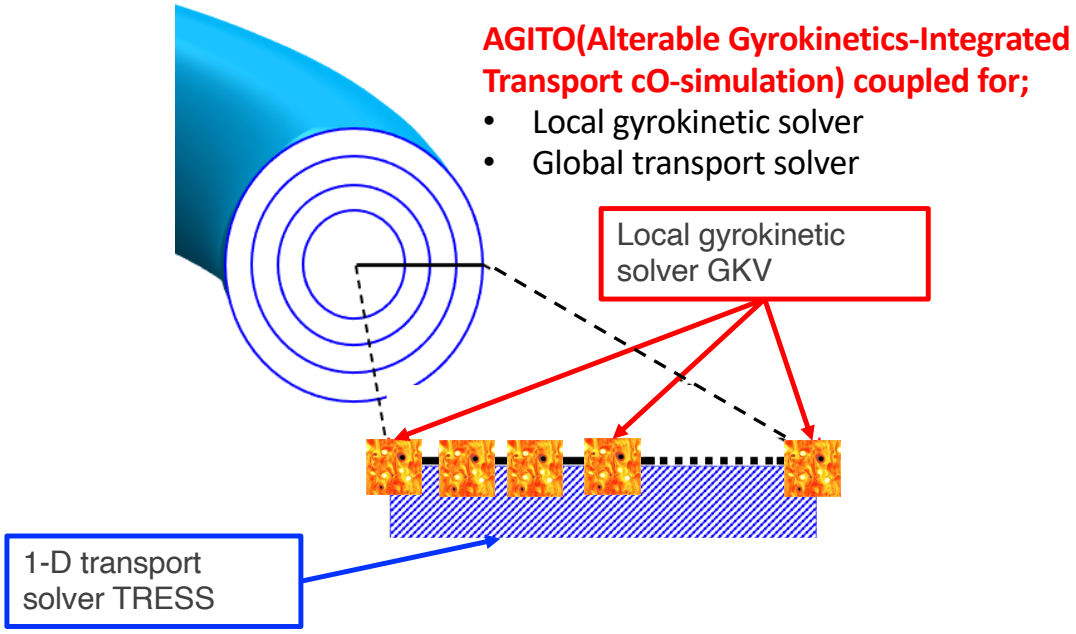

Fig. 4.1: Schematic image of co–simulation AGITO.

It is noted that both the simplified transport model with the linear calculation and the fully nonlinear turbulence simulation are applicable in the evaluation of turbulent diffusivities. This is a remarkable point of this study that has not been addressed in the previous studies. This realizes a flexible switching of the turbulent transport model during the global simulation. For instance, after the global simulation to nearly steady–state profile based on the simplified model, more accurate calculations can seamlessly be carried out by using the nonlinear gyrokinetic calculations. AGITO can provide a fast global profile prediction with nearly first-principle-based evaluations of turbulent transport including the zonal-flow effects.

4.3 Physical model and numerical setup

A theoretical framework of AGITO and the numerical set up are presented in this section. The calculation of turbulent transport is based on Eqs. (1.10), and (1.11), where the equations are shown again for completeness:

$$\begin{aligned}
&\left[\frac{\partial}{\partial t}+v_{\parallel}\nabla_{\parallel}+i\omega_{\mathrm{Ds}}-\left(\frac{e_{\mathrm{s}}\mu}{m_{\mathrm{i}}}\nabla_{\parallel}B\right)\frac{\partial}{\partial v_{\parallel}}\right]\delta f_{\mathrm{s}\boldsymbol{k}_{\perp}}\\
-\ &\frac{1}{B}\sum_{\boldsymbol{k}'_{\perp}+\boldsymbol{k}''_{\perp}=\boldsymbol{k}_{\perp}}\boldsymbol{b}\cdot(\boldsymbol{k}'_{\perp}\times\boldsymbol{k}''_{\perp})J_0(k'_{\perp}\rho_{\mathrm{s}})\delta\phi_{\boldsymbol{k}'_{\perp}}\delta f_{\mathrm{s}\boldsymbol{k}''_{\perp}}\\
=\ &\frac{e_{\mathrm{s}}F_{\mathrm{Ms}}}{T_{\mathrm{s}}}(i\omega_{*T\mathrm{s}}+i\omega_{\mathrm{Ds}}-v_{\parallel}\nabla_{\parallel})J_0(k_{\perp}\rho_{\mathrm{s}})\delta\phi_{\boldsymbol{k}_{\perp}}+C_{\mathrm{s}},
\end{aligned}$$

$$\left[k_{\perp}^2+\sum_{\mathrm{s}}\frac{1}{\lambda_{D\mathrm{s}}}(1-\Gamma_{0\mathrm{s}\boldsymbol{k}_{\perp}})\right]\delta\phi_{\boldsymbol{k}_{\perp}}\ =\ \frac{1}{\varepsilon_0}\sum_{\mathrm{s}}e_{\mathrm{s}}\int d\boldsymbol{v}\ J_0\delta f_{\mathrm{s}\boldsymbol{k}_{\perp}},$$

Then, the turbulent heat flux $Q_{\mathrm{trb,s}}$ is calculated by the perturbed distribution function $\delta f_{\mathrm{s},\boldsymbol{k}_{\perp}}$ and the potential fluctuation $\delta\phi_{\boldsymbol{k}_{\perp}}$ based on Eq. (1.12). Then, substituting into the 1–dimensional transport equation in Eq. (1.9) as well as the neoclassical flux $Q_{\mathrm{NC,s}}$, the time evolution of the pressure profile $p_{\mathrm{s}}(r,t)=n_{\mathrm{s}}(r,t)T_{\mathrm{s}}(r,t)$ is calculated. The transport equation is also shown again for completeness:

$$\frac{3}{2}\frac{\partial}{\partial t}p_{\mathrm{s}}=-\frac{1}{V'}\frac{\partial}{\partial r}V'\left(\frac{5}{2}T_{\mathrm{s}}\Gamma_{\mathrm{s}}+Q_{\mathrm{NC,s}}+Q_{\mathrm{trb,s}}\right)+S_{\mathrm{s}},\tag{4.1}$$

where, Γ_{s} and S_{s} denote the particle flux and the external heating source/sink, respectively. Although the particle flux is evaluated in gyrokinetic simulations with the kinetic electron response, we impose $\Gamma_{\mathrm{s}}=0$ by the assumption of adiabatic electron response. Therefore, the density profile does not change in time.

The convective form of Eq. (4.1) can be rewritten as the following diffusion

form with the effective thermal diffusivity $\chi_{\rm s} = Q_{\rm s}/(-n_{\rm s}\nabla T_{\rm s}\cdot\nabla r)$:

$$\frac{3}{2}\frac{\partial}{\partial t}p_{\rm s} = \frac{1}{V'}\frac{\partial}{\partial\rho}V'\left(\langle|\nabla\rho|^2\rangle(\chi_{\rm trb,s}+\chi_{\rm NC,s})n_{\rm s}\frac{\partial T_{\rm s}}{\partial\rho}\right) + S_{\rm s}, \tag{4.2}$$

where ρ denotes the normalized radius defined by flux surface label in general non–circular tokamak geometry. Note that the turbulent diffusivities are calculated at discrete radial locations. Then, they are treated as a system-wide continuous turbulent diffusivity profile by Akima interpolation [74, 75] which is a piecewise cubic interpolation with the advantages of "always passing through a given data point", "hard to overshooting", and "unaffected by distant interpolation points". These characteristics contribute to numerically stable calculations.

The turbulent heat diffusivity $\chi_{\rm trb,s}$ generally has a strong nonlinear dependence on the local temperature gradient. When a numerical time–integration scheme, such as backward–time centered–space method and Crank–Nicolson method, is used without accounting for this nonlinearity, a numerical instability can occur. A simple prescription for this problem is to update the profile evolution with a time scale as much as shorter than that of turbulent transport. However, this is often not practicable for long–time simulations because of a significant increase of computational iterations. In this study, we introduce a stabilization technique called Newton iteration [76], which treats the turbulent diffusivity in an implicit form. Indeed, the turbulent heat diffusivity is Taylor expanded in time so as to be evaluated implicitly, as follows:

$$\chi_{\rm s}^{n+1} = \chi_{\rm s}^{n+1} + \sum_j \frac{\partial\chi_{\rm s}^n}{\partial {T'}_j}\left({T'}_j^{n+1} - {T'}_j^{n}\right). \tag{4.3}$$

Here, n, j, and $T' \equiv \partial T/\partial\rho$ mean time step, species index, and, the temperature gradient, respectively. Equation (4.3) introduces a nonlinear temperature gradient dependence of thermal diffusivity, which can stabilize time integration in Eq. (4.2). As for the neoclassical transport, $\chi_{\rm NC,s}$ is evaluated by the matrix inversion

method based on the moment approach [73]. Also, the pressure–gradient driven bootstrap current is obtained in the same manner.

For the spatial discretization, the Galerkin method with Hermite basis functions is used to solve the transport equation as a partial differential equation. This is a special type of finite element methods that utilizes a structured/unstructured mesh to find a weak–form solution of the partial differential equation with spatially discretized variables. For the boundary condition, the symmetric condition at the magnetic axis of $\rho = 0$ is imposed for the profiles and heat diffusivity [76], while the Neumann or Dirichlet condition is selected at the plasma edge of $\rho = 1$, depending on the problem.

Because of the implicit treatment to solve Eq. (4.2), a convergence criteria ϵ_T is necessary to ensure the calculation accuracy. Here, we consider $\epsilon_T = 0.01$ for the maximum residual error in $T_{\rm s}(\rho, t)$ at each time step.

4.4 Numerical verification of AGITO

In this section, numerical verifications of newly developed AGITO are presented. First, the convergence of the turbulent diffusivity profile regarding the number of gyrokinetic calculation points in the radial direction is investigated. Secondly, global profile evolutions under the stationary heating are examined, as well as including the heating power scan.

The initial conditions of kinetic profiles, safety factor profile, and heating profile are summarized in Fig. 4.2. Here, since the electron response is assumed to be adiabatic, the particle transport does not occur. Thus, the density profile is fixed in time. The turbulent diffusivity is evaluated by the simplified transport model in Eq. (3.8). We consider a tokamak configuration which is same as considered in Chap. 2 and Chap. 3. The heating and magnetic fields are assumed to be stationary. The Dirichlet boundary is imposed at the plasma edge of $\rho = 1$. The time step of global transport solver is assumed as $\Delta t = 1$ msec, which is determined such

that Δt is enough smaller than the energy confinement time, but enough larger than the characteristic time scale of turbulence in the order of $1/\gamma$. Therefore, the turbulent transport level is treated to be constant within Δt.

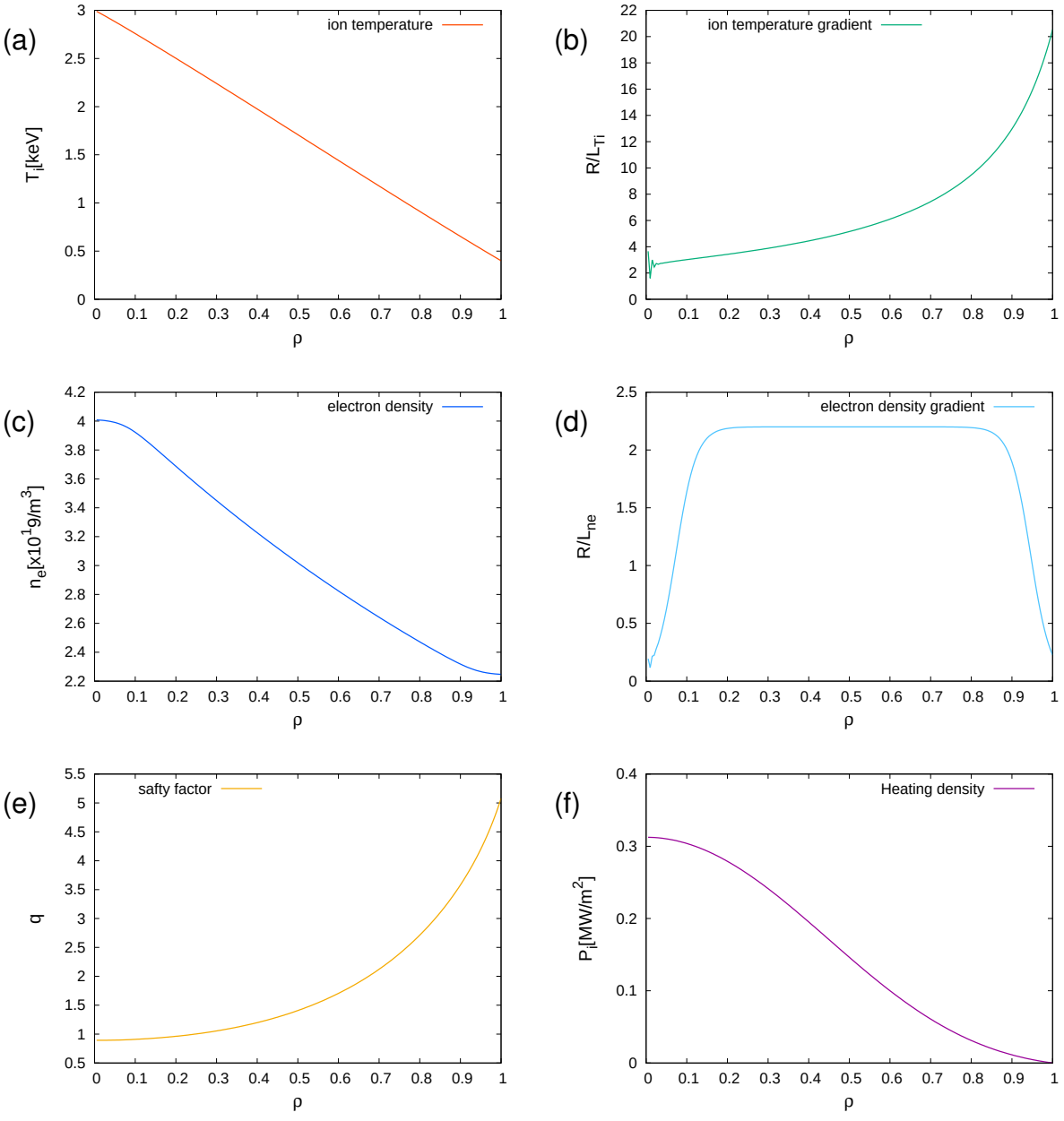

Fig. 4.2: Initial profiles of (a) ion temperature, (b) ion temperature gradient, (c) electron density, (d) electron density gradient, (e) safety factor, and (f) heating flux.

4.4.1 Radial resolution of turbulent transport calculations

In AGITO, the turbulent diffusivity is evaluated by several local simulations distributed in the radial direction. Then, the global profile is obtained by Akima interpolation. In this subsection, the convergence regarding the number of gyrokinetic calculation points is examined.

The number of gyrokinetic calculation points in the radial direction can be regarded as the radial resolution of the turbulent transport profile. To understand the convergence regarding the resolution, a comparison of the turbulent heat diffusivity profile evaluated by varying the number of local gyrokinetic simulations is performed. The comparisons are made by calculating one time step from the initial profile. The local simulations of 5, 9, and 17 points are distributed in equal spacing from $\rho = 0.1$ to 0.9. As shown in Fig. 4.3, the turbulent diffusivity profiles are almost identical, regardless of the number of local simulations in the radial direction. It should be noted that Akima interpolation is not applicable for $\rho < 0.1$ and $\rho > 0.9$ since there are no gyrokinetic calculation in those regions. Then, the extrapolation is performed such that the transport flux is zero at the magnetic axis of $\rho = 0$. On the other hand, on the boundary side, the value is assumed to be constant toward the plasma edge of $\rho = 1$ In the following, 9 points calculation is employed from the view point of the both resolution and computational cost.

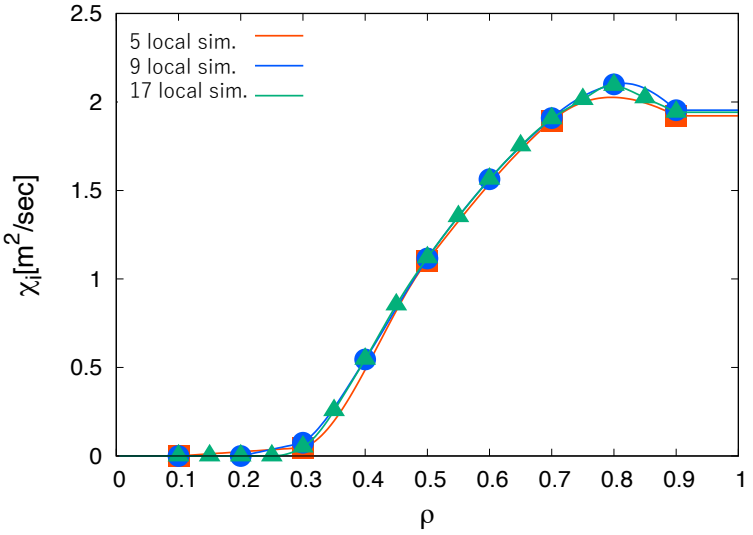

Fig. 4.3: Comparison of the turbulent diffusivity profiles for the cases with different number of local simulations. The symbols and lines represent gyrokinetic calculations and interpolated data, respectively.

4.4.2 Global transport simulation with stationary heating

In this subsection, we discuss the numerical verifications of AGITO in terms of global profile evolutions towards the power-balanced steady state with and without heating. As shown in Fig. 4.4, three heating flux profiles, which are constant in time, are considered, i.e., decaying simulation with zero heating, 5MW stationary heating, and 8MW case. The total heating power (in MW unit) is obtained by the volume integral of the heating flux profile. Any sink regions are not considered in these simulations, and Dirichlet boundary condition is imposed at the plasma edge. We also assume that the heating flux is totally absorbed in the plasma without any losses.

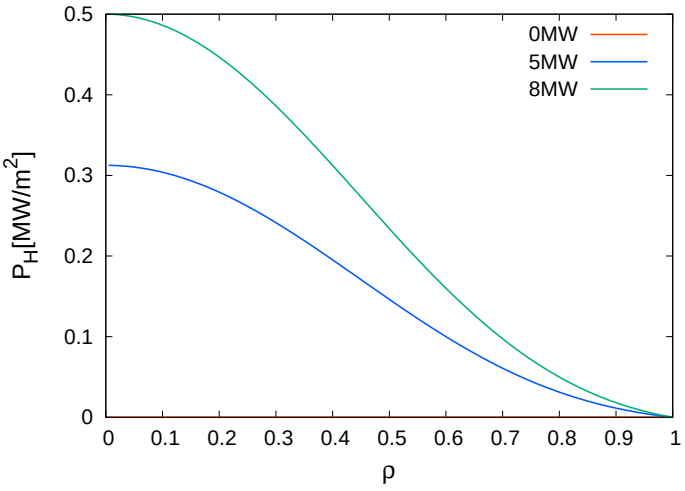

Fig. 4.4: Heating flux profiles for stationary heating simulations

Figure 4.5 shows the spatio-temporal profile evolutions in the case without the external heating. The initial profiles continuously decay in time, and eventually relax into a critical state where the turbulent transport vanishes, as expected. Then, the temperature profile is determined by the marginal condition of the linear ITG instability , i.e., $R/L_T \leq R/L_T|_{\rm crit.}$, when the neoclassical transport is negligibly small compared to the turbulent transport. Indeed, one can see that the heat diffusivity profile χ_i significantly decays at $t = 0.5$, but not strictly indicates the zero state. It still needs a time for fully relaxed state. From the simulation results, the temperature gradients R/L_T for the inner core region of $\rho = 0.25, 0.5$ at $t = 0.5$sec are evaluated as 4.76, 4.66, respectively. These values are consistent with the ITG critical gradients $R/L_T|_{\rm crit.}$ calculated from the local nonlinear gyrokinetic simulation as discussed in Chap. 2. For the outer core region of $\rho = 0.6, 0.75$, we observe R/L_T as 4.97 and 5.83, respectively, which is slightly larger compared to that in the ITG critical gradients. The difference is attributed to the fact that the temperature profile is not yet a fully relaxed state with vanished turbulent transport. It is noted that the time evolution of the bootstrap current

is determined by the neoclassical transport coefficient and the pressure gradient profile that is dominantly determined by the turbulent transport.

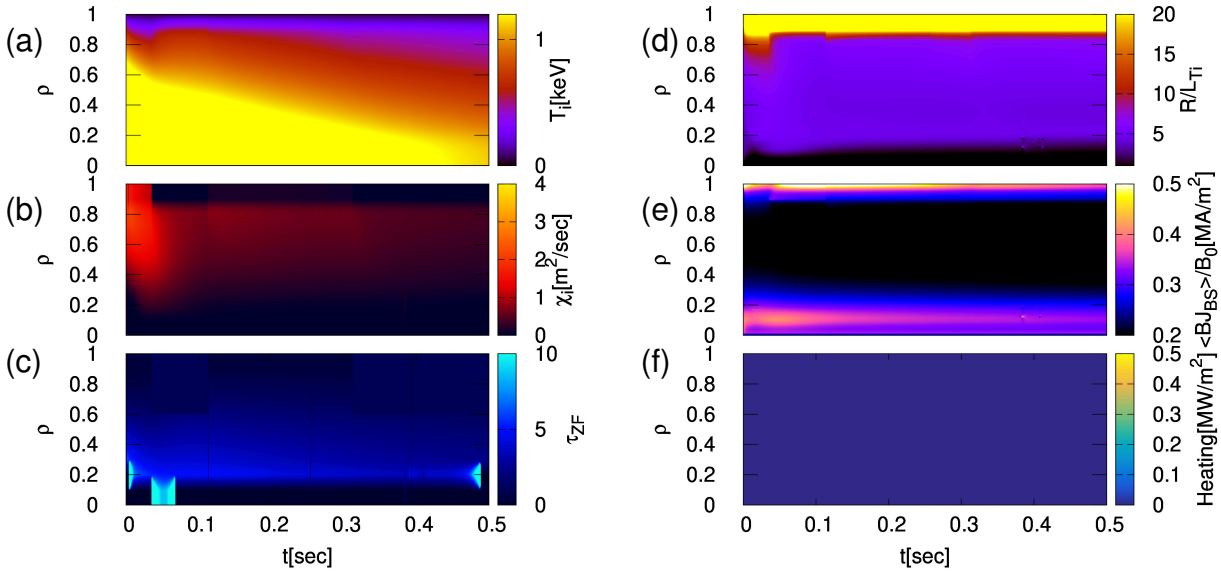

Fig. 4.5: Spatio–temporal evolution of the profiles in decaying transport simulation without heating. (a) ion temperature, (b) turbulent heat diffusivity, (c) τ_{ZF} defined by Eq. (3.2), (d) ion temperature gradient, (e) bootstrap current, (f)heating flux(constant in time).

As for the cases with stationary heating, the spatio-temporal profile evolutions in 5MW heating are shown in Fig. 4.6. Unlike the previous decaying simulations, one finds a significant drive of the turbulent transport. In this case, the profiles quickly develop towards a steady state that the total transport flux is balanced with the external heating flux. This is confirmed from the integrated heating flux profiles at $t = 0.4$sec, as shown in Fig. 4.7. One also finds the large $\tau_{\rm ZF}$ in the inner core region, where the strong generation of zonal flows is expected. It is noted that the fine oscillations of $\tau_{\rm ZF}$ is attributed to a numerical oscillation of the ITG growth rate $\gamma_{\rm max}$, which appears in the integral interval of $\tau_{\rm ZF}$ in Eq. (3.2) in the inner core region. Indeed, since the ITG instability becomes marginal around the magnetic axis, the numerical convergence for the growth rate tends to de-

grade in the initial–value gyrokinetic solver. This will be improved by using more long–time linear gyrokinetic simulations or imposing more elaborate convergence criteria.

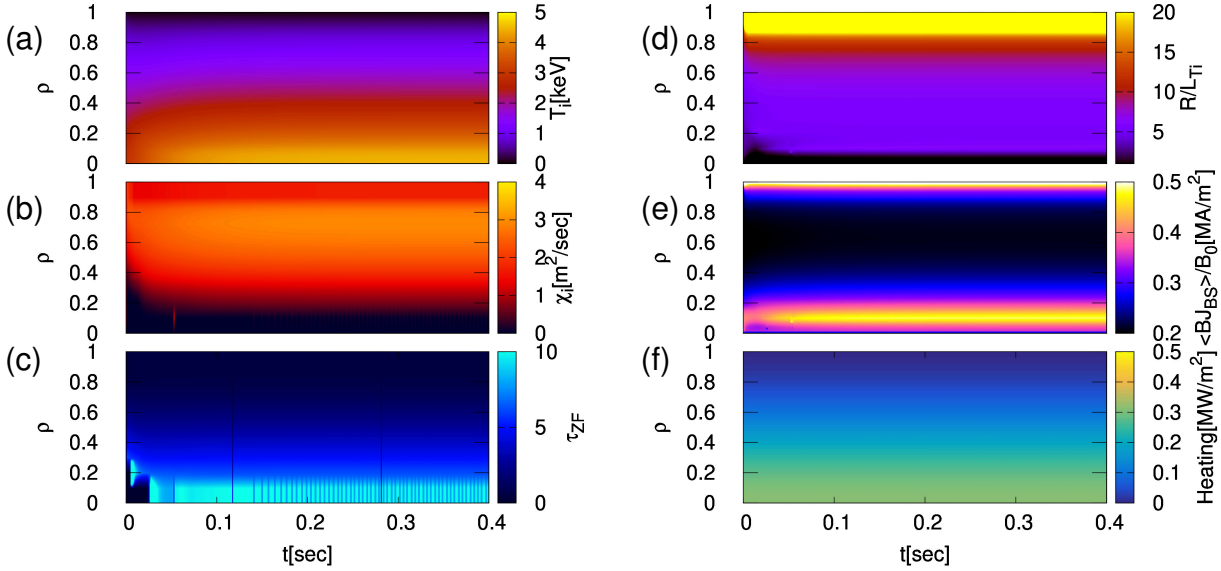

Fig. 4.6: Spatio–temporal evolution of the profiles in decaying transport simulation with 5MW heating. (a) ion temperature, (b) turbulent heat diffusivity, (c) τ_{ZF} defined by Eq. (3.2), (d) ion temperature gradient, (e) bootstrap current, (f)heating flux(constant in time).

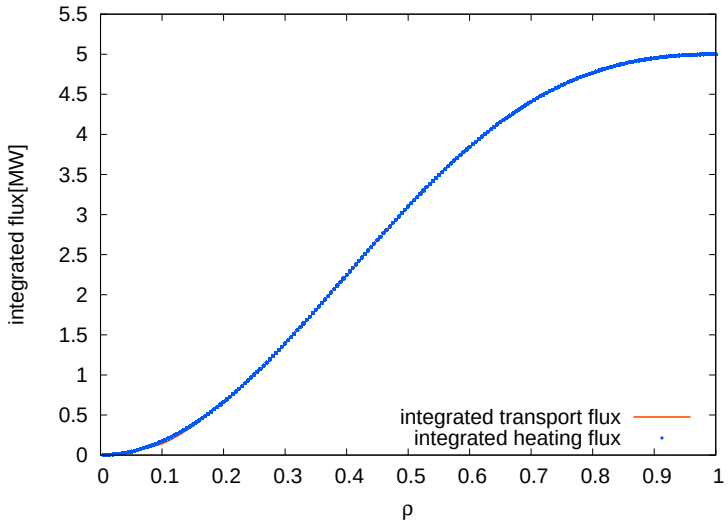

Fig. 4.7: Comparison of transport flux and integrated heating flux at $t = 0.4$sec in Fig. 4.6.

The results of 8MW heating simulation are shown in Fig. 4.8, where a qualitatively similar time evolution of the profiles compared to 5MW case is observed. The power balanced steady temperature profiles and turbulent diffusivity profiles evaluated at t=0.4sec are compared in Fig. 4.9. One can see a physically reasonable tendency of the heating power dependence of the steady temperature profiles. Note that the increaseing temperature gradient around the plasma edge is resulting from the Dirichlet boundary condition, i.e., $T_{\rm i}(\rho = 1, t) = T_{\rm i}(\rho = 1, 0)$. Although the numerical verification is successfully confirmed, further validations with comparisons to the experiments are needed to confirm the quantitative reproducibility in further works. It is also noted that the physical effect of zonal flows is taken into account in the simplified transport model constructed in Chap. 3, and cannot be reproduced by a turbulent transport model that ignores nonlinearities [23–27], especially in near–marginal stability regimes around the magnetic axis of $\rho \sim 0.1$.

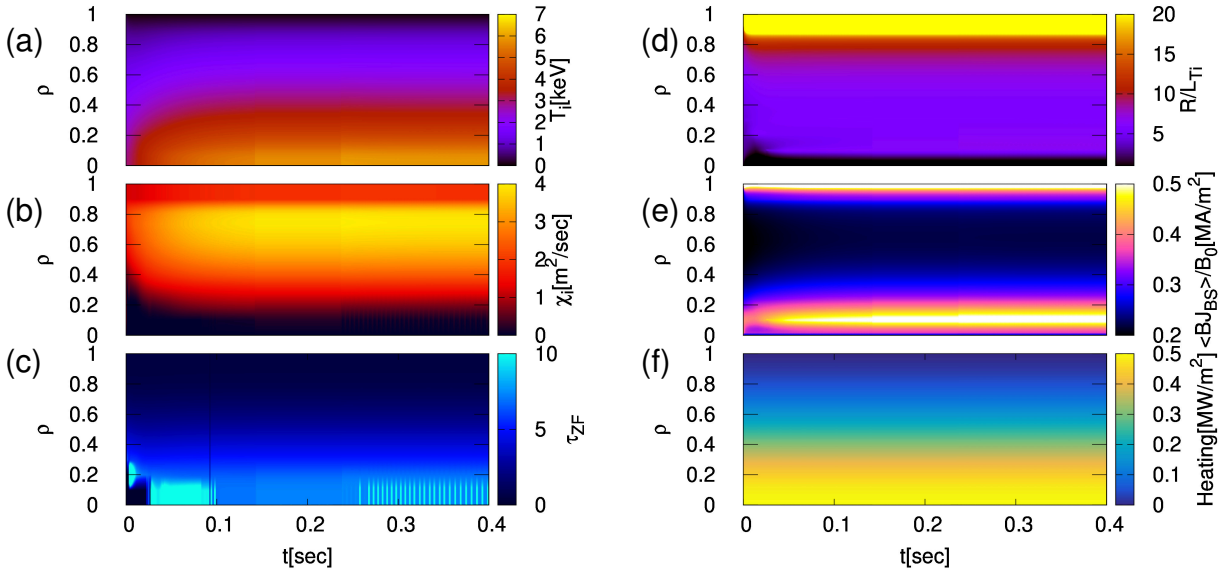

Fig. 4.8: Spatio–temporal evolution of the profiles in decaying transport simulation with 8MW heating. (a) ion temperature, (b) turbulent heat diffusivity, (c) τ_{ZF} defined by Eq. (3.2), (d) ion temperature gradient, (e) bootstrap current, (f) heating flux(constant in time).

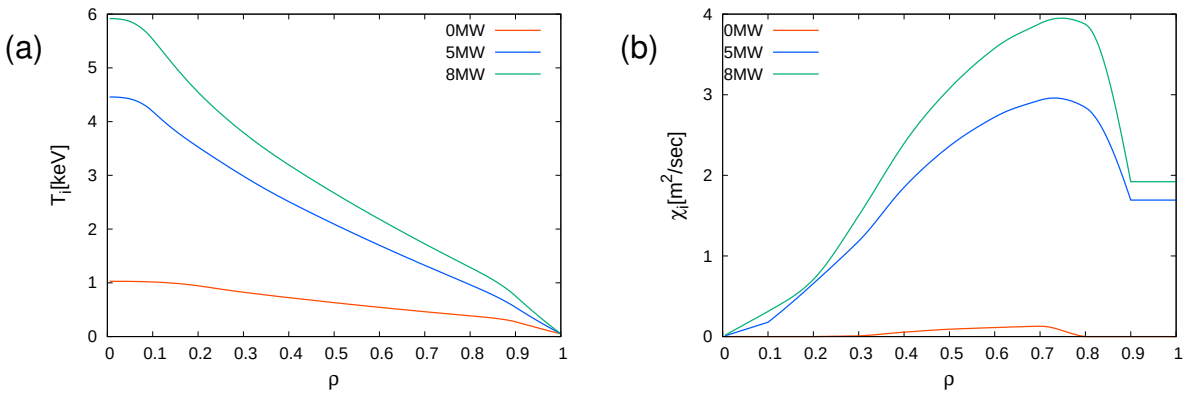

Fig. 4.9: Comparison of the power-balanced steady profiles. (a) ion temperature, (b) turbulent heat diffusivity.

Chapter 5

Impacts of background variations on profile formation

5.1 Introduction

As a powerful approach to study the global transport and profile formation in fusion plasmas, global full–f gyrokinetic simulations have been developed. Then, the various non–local dynamics of turbulent transport, including the radial electric fields [77, 78], avalanche [79–82], and ballistic propagation of fluctuations [83–85] has been revealed. Since such global simulation requires the huge computational cost, the comprehensive scan of the various heating scenarios is still limited. Also, the macroscopic background quantities such as the heating and confinement magnetic fields have been assumed to be stationary.

In burning plasmas, not only the global turbulence dynamics described above, but also spatio-temporal variations of the background quantities coupled with turbulent transport through the pressure profile formation are expected. In order to explore such unrevealed interactions between the turbulent transport and the variations of heating and magnetic fields, a novel co–simulation for the global transport analysis, AGITO, was developed. The numerical verifications with the stationary heating were discussed in Chap. 4. Then, this chapter presents the AGITO cal-

culations for primitive cases with (i)heating power variation or (ii)magnetic field variation, which can interact with the turbulent transport and profile formation.

The rest of this chapter is organized as follows. The AGITO simulation results with background variations are presented in Sec. 5.2. Some further discussions for more practical problems are given in Sec. 5.3.

5.2 AGITO simulation with background variations

Impacts of background variations on global transport and profile formation are investigated by means of AGITO, where the temporal variations of the heating power and magnetic fields are treated as sinusoidal modulations. In this study, to elucidate the fundamental impacts from the modulations, an analytic time dependence is imposed to the modulation without any feedback from the kinetic profiles. The other simulation conditions are assumed to be the same as in Sec. 4.4.

5.2.1 Heating power modulation

In this subsection, the impact of the heating power modulation is investigated. The temporal variation of the heating power $P_{\mathrm{H}}(t)$ is given by the following expression:

$$P_{\mathrm{H}}(t) = (1 + \lambda_{\mathrm{H}} \sin(2\pi\omega_{\mathrm{H}} t))\, P_{\mathrm{ave}}, \tag{5.1}$$

where, λ_H, ω_{H}, and P_{ave} correspond to the modulation amplitude, the modulation frequency, and the average heating power, respectively. Table 5.1 summarizes the values used in the present simulations. Except for the amplitude, the radial profile of the heating density is the same as in Sec. 4.4.

The simulation results of heating power modulation in case 1 to 4 are shown

Table 5.1: Parameters for heating power modulation

	λ_H	$\omega_{\rm H}$ [sec^{-1}]	$P_{\rm ave}$[MW]
case 1	0.4	5	5
case 2	0.4	10	5
case 3	0.4	100	5
case 4	0.6	5	5
case 5	0.4	5	8

in Figs. 5.1 to 5.4, respectively. Note that, in order to highlight the fluctuation components, the steady–state profile in the stationary 5MW heating (Fig. 4.6) is subtracted from the contour maps in the figures. The result of the case 5 is shown in Fig. 5.5, where the similar subtraction is applied with the steady–state profile in the stationary 8MW heating(Fig. 4.8). The fluctuation component is expressed by the symbol Δ for each physical quantity. For example, the fluctuation component of ion temperature $\Delta T_i(\rho, t)$ is defined as

$$\Delta T_{\rm i}(\rho, t) = T_{\rm i}^{\rm mod.}(\rho, t) - T_{\rm i}^{\rm steady}(\rho). \tag{5.2}$$

Here, $T_{\rm i}^{\rm mod.}$ and $T_{\rm i}^{\rm steady}$ correspond to the ion temperature in the heating power modulation case and the steady–state profile in the steady heating case, respectively. The steady profile $T_{\rm i}^{\rm steady}$ is evaluated at $t = 0.4$sec in the steady heating case, as shown in Fig. 4.9. It is found that, in all cases, the physical quantities are affected by the heating power modulation involving a time delay. Focusing this point, Fig. 5.6 shows the time evolutions of the heating density, ion temperature, and turbulent diffusivity at $\rho = 0.2$ in the cases of heating frequencies $\omega_{\rm H} = 5$ and 10. We can see that the negative phase shift, i.e., time delay, against the sinusoidal heating modulation becomes large for the turbulent diffusivity following the ion temperature. Note also that the time delay indicates a radial dependence. Especially in the inner core region, we can see a moderate radial propagation of the turbulent diffusivity in the case 1, 2, and 4. In the case 3 with higher frequency modulation, the fluctuation amplitude is relatively small compared to that in the

cases with lower frequency. This suggests the existence of an upper limit for the heating modulation frequency to be responded by the other physical quantities. The time delays and frequencies of temperature profiles and turbulent diffusivity at $\rho = 0.2$(inner core) and $\rho = 0.5$(mid–radius) are summarized in Tabs. 5.2 and 5.3. Here, the time delay and frequency for the turbulent diffusivity and ion temperature are denoted by Δt_χ, Δt_T, ω_χ and ω_T, respectively. Note that these parameters are normalized by the heating modulation frequency $\omega_{\rm H}$. First, we find that the normalized frequencies $\omega_\chi/\omega_{\rm H}$ and $\omega_{\rm T}/\omega_{\rm H}$ show the almost unity for both the inner core and mid–radius regions, indicating that the period of the fluctuating quantities matches with the heating power modulation. On the other hand, as for the time delay, we can see a significant difference between $\Delta t_\chi \omega_{\rm H}$ and $\Delta t_{\rm T}\omega_{\rm H}$, where a drastic change appears in the turbulent diffusivity depending on the modulation scenario. In particular, we observe that the time delay of heat diffusivity in the inner core region is larger than mid–radius, corresponding to the propagation of heat diffusivity from the edge side to the core region. In case 3, such propagation becomes less significant compared to the temporal variation of the heating, resulting in a relatively larger normalized time delay.

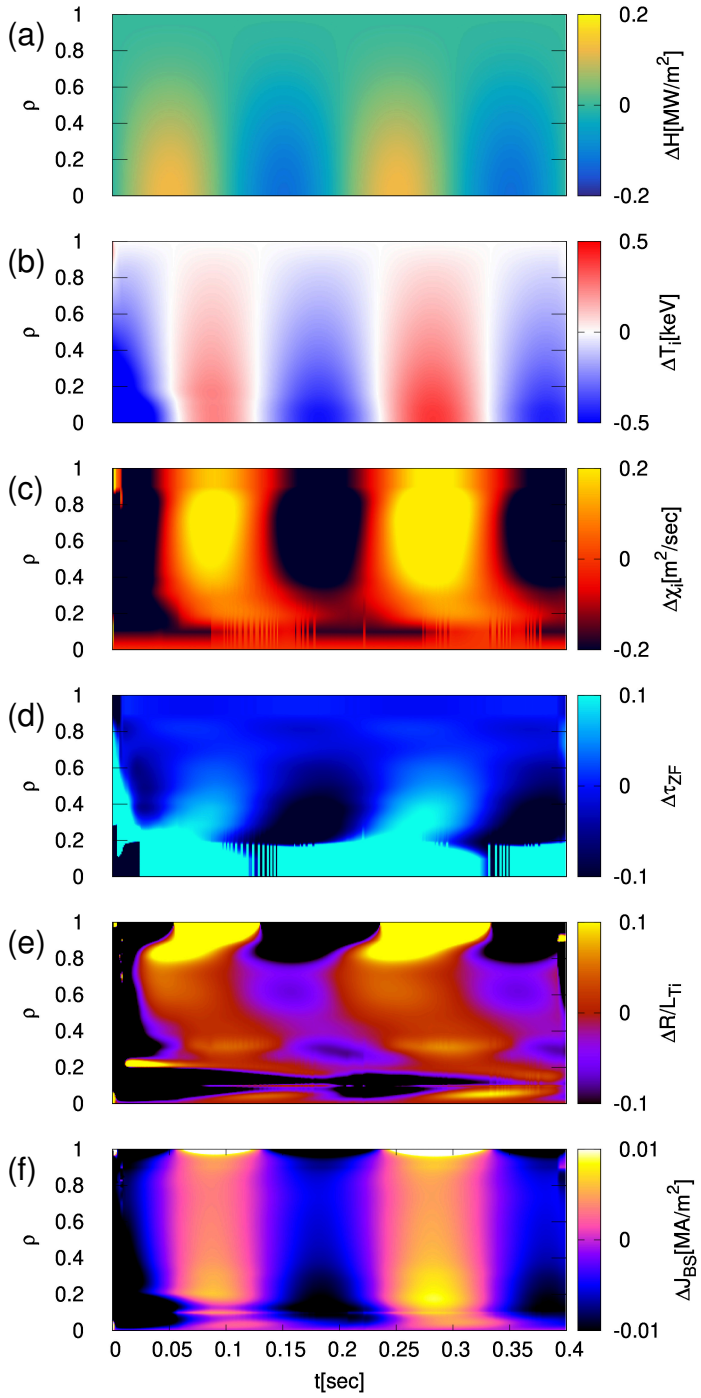

Fig. 5.1: Spatio-temporal evolutions in heating modulation with case 1, where the fluctuation component is displayed. Amplitude, frequency, and average heating power are, $\lambda_{\rm H} = 0.4$, $\omega_{\rm H} = 5{\rm sec}^{-1}$, and $P_{\rm ave} = 5MW$, respectively. (a) heating density, (b) ion temperature, (c) turbulent diffusivity, (d) zonal–flow decay time, (e) ion temperature gradient, (f) bootstrap current.

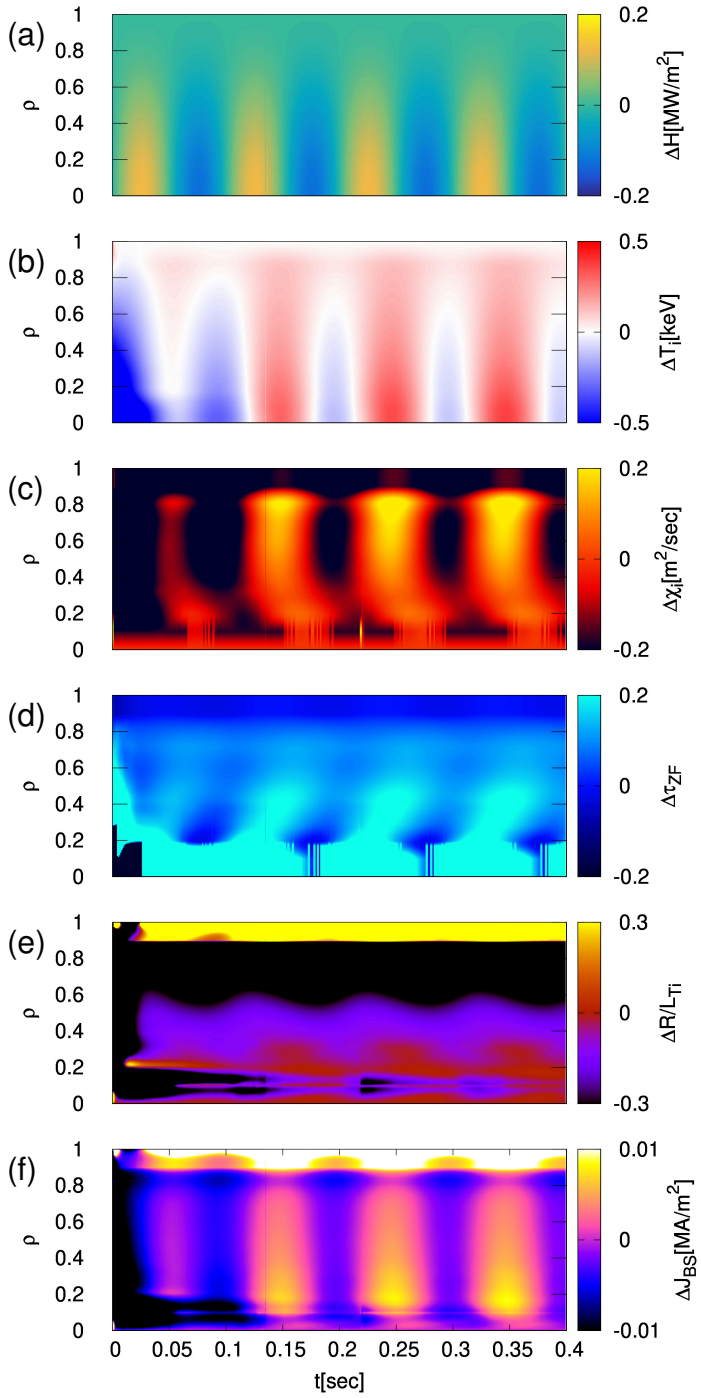

Fig. 5.2: Spatio-temporal evolutions in heating modulation with case 2, where the fluctuation component is displayed. Amplitude, frequency, and average heating power are, $\lambda_{\rm H} = 0.4$, $\omega_{\rm H} = 10{\rm sec}^{-1}$, and $P_{\rm ave} = 5MW$, respectively. (a) heating density, (b) ion temperature, (c) turbulent diffusivity, (d) zonal–flow decay time, (e) ion temperature gradient, (f) bootstrap current.

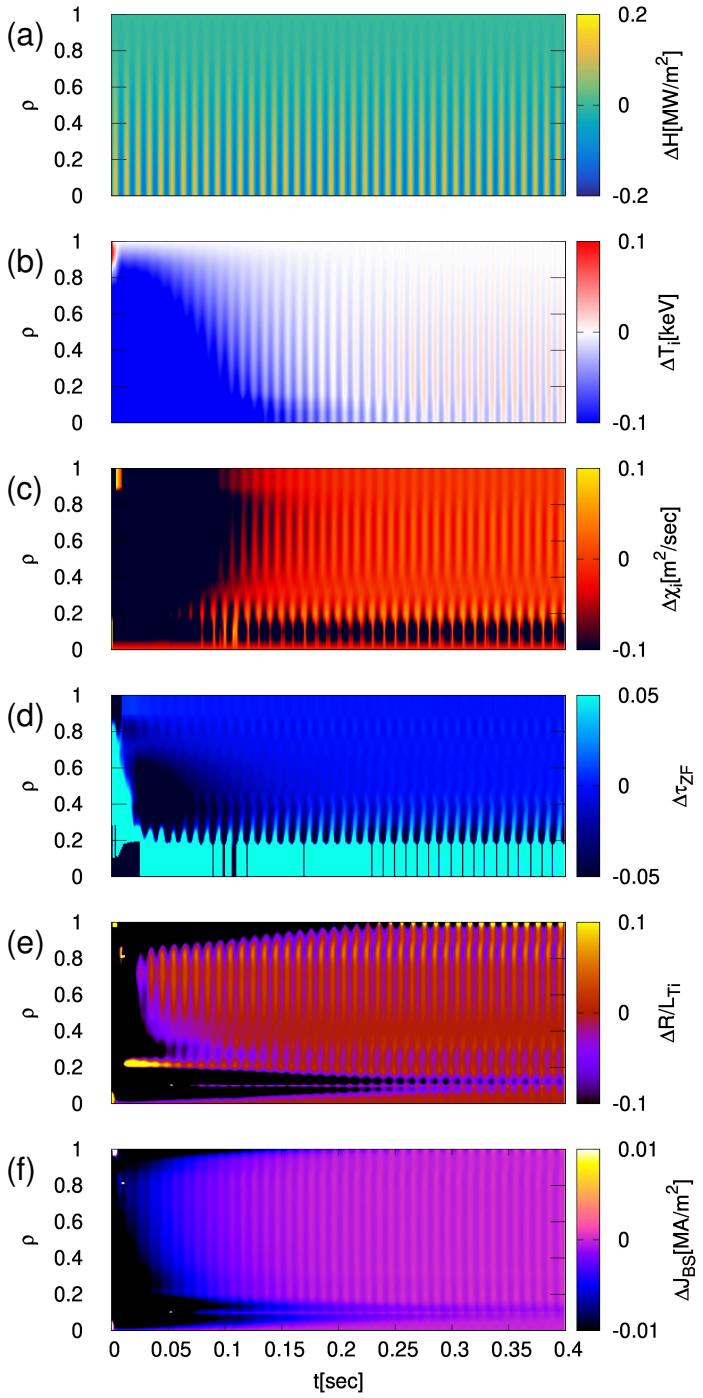

Fig. 5.3: Spatio-temporal evolutions in heating modulation with case 3, where the fluctuation component is displayed. Amplitude, frequency, and average heating power are, $\lambda_{\rm H} = 0.4$, $\omega_{\rm H} = 100{\rm sec}^{-1}$, and $P_{\rm ave} = 5MW$, respectively. (a) heating density, (b) ion temperature, (c) turbulent diffusivity, (d) zonal–flow decay time, (e) ion temperature gradient, (f) bootstrap current.

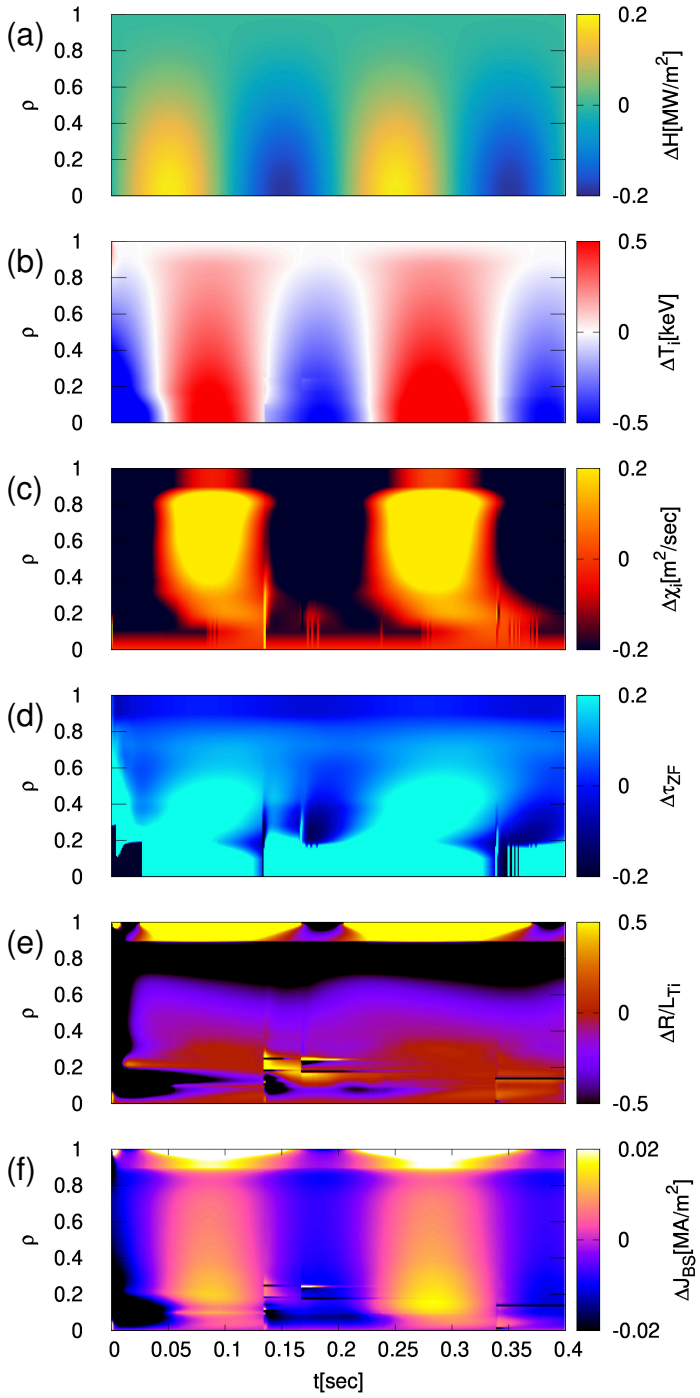

Fig. 5.4: Spatio-temporal evolutions in heating modulation with case 4, where the fluctuation component is displayed. Amplitude, frequency, and average heating power are, $\lambda_{\rm H} = 0.6$, $\omega_{\rm H} = 5{\rm sec}^{-1}$, and $P_{\rm ave} = 5MW$, respectively. (a) heating density, (b) ion temperature, (c) turbulent diffusivity, (d) zonal–flow decay time, (e) ion temperature gradient, (f) bootstrap current.

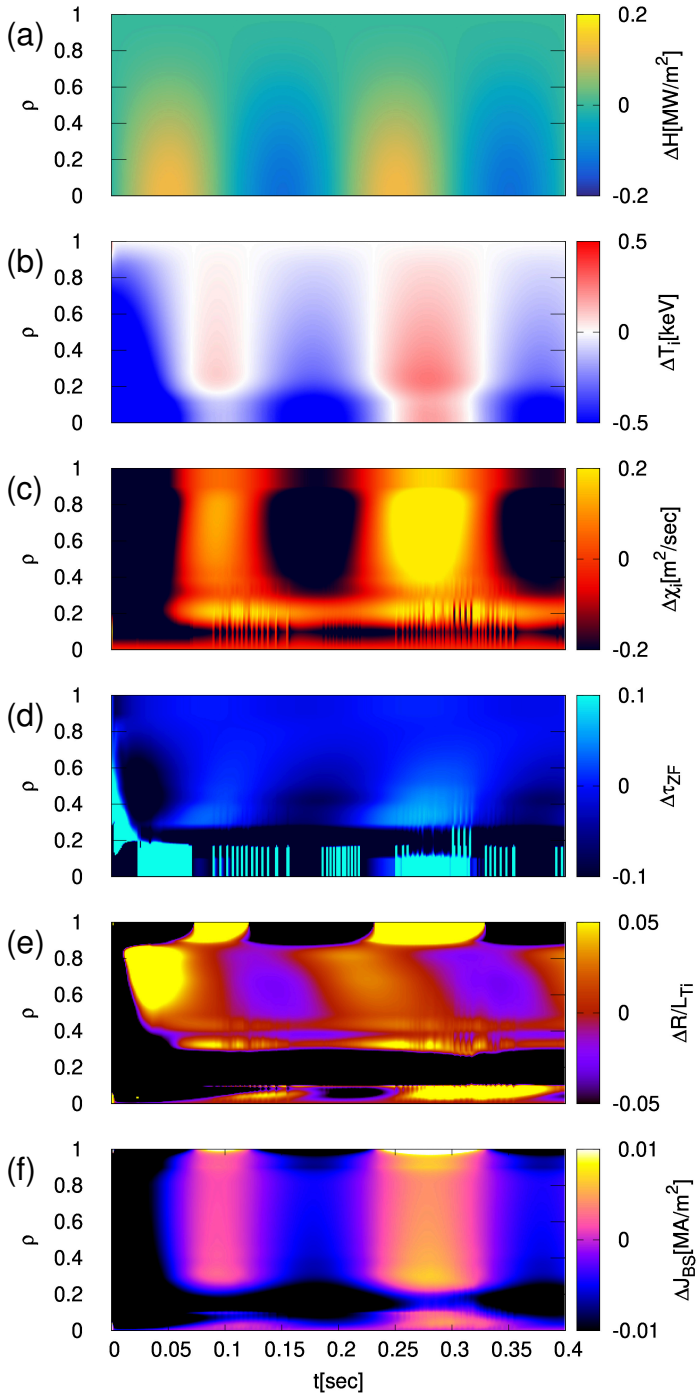

Fig. 5.5: Spatio-temporal evolutions in heating modulation with case 5, where the fluctuation component is displayed. Amplitude, frequency, and average heating power are, $\lambda_{\rm H} = 0.4$, $\omega_{\rm H} = 5{\rm sec}^{-1}$, and $P_{\rm ave} = 8MW$, respectively. (a) heating density, (b) ion temperature, (c) turbulent diffusivity, (d) zonal–flow decay time, (e) ion temperature gradient, (f) bootstrap current.

Table 5.2: Normalized time delay and frequency at $\rho = 0.2$

	case 1	case 2	case 3	case 4	case 5
$\Delta t_\chi \omega_{\mathrm{H}}$	0.25	0.36	0.60	0.26	0.21
$\Delta t_T \omega_{\mathrm{H}}$	0.16	0.21	0.20	0.15	0.15
$\omega_\chi / \omega_{\mathrm{H}}$	1.04	0.99	1.0	1.01	1.10
$\omega_T / \omega_{\mathrm{H}}$	1.03	1.0	1.0	1.02	1.07

Table 5.3: Normalized time delay and frequency at $\rho = 0.5$

	case 1	case 2	case 3	case 4	case 5
$\Delta t_\chi \omega_{\mathrm{H}}$	0.16	0.20	0.20	0.155	0.14
$\Delta t_T \omega_{\mathrm{H}}$	0.16	0.20	0.20	0.16	0.14
$\omega_\chi / \omega_{\mathrm{H}}$	1.01	1.01	1.0	1.02	1.09
$\omega_T / \omega_{\mathrm{H}}$	1.03	1.02	1.0	1.01	1.08

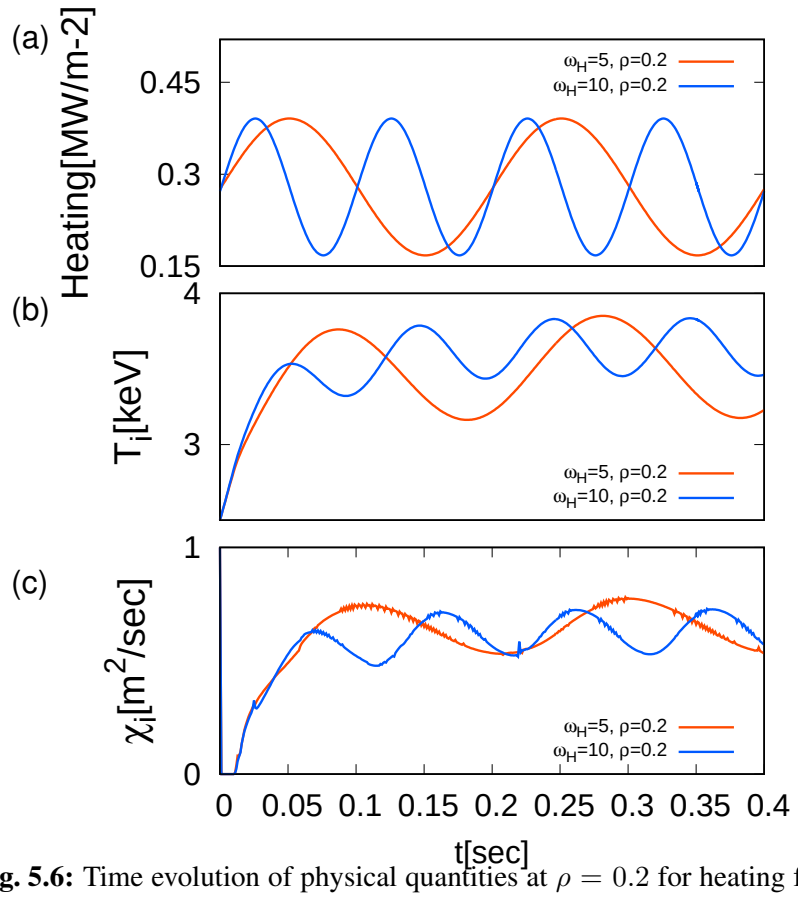

Fig. 5.6: Time evolution of physical quantities at $\rho = 0.2$ for heating frequency $\omega_{\mathrm{H}} = 5$ and 10. (a) heating density, (b) ion temperature, (c) turbulent diffusivity.

For comparisons with the stationary heating case, the time evolution of ion temperature at $\rho = 0.2$ and 0.5 is shown in Fig. 5.7. We can see that the case 2 and 4 indicate a stronger deviation from the stationary heating case, while the other cases show oscillation around the stationary heating case. Although the deviation amplitude is not so large in the present simulation settings, the above feature appears in the time-averaged temperature profile $t \geq 0.2$sec, as shown in Fig. 5.8.

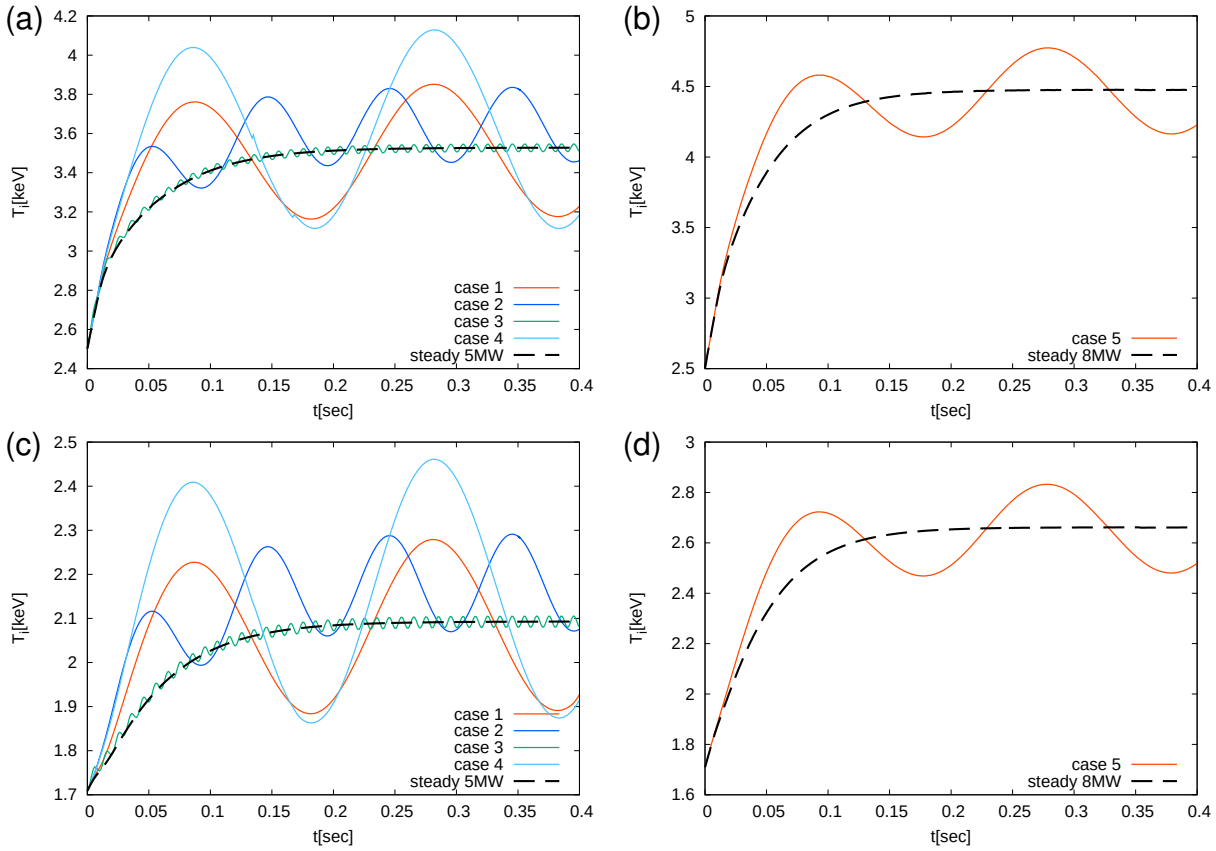

Fig. 5.7: Time evolution of ion temperature (a) at $\rho = 0.2$, $P_{\rm ave} = 5$MW, (b) at $\rho = 0.2$, $P_{\rm ave} = 8$MW, (c) at $\rho = 0.5$, $P_{\rm ave} = 5$MW, and (d) at $\rho = 0.5$, $P_{\rm ave} = 8$MW.

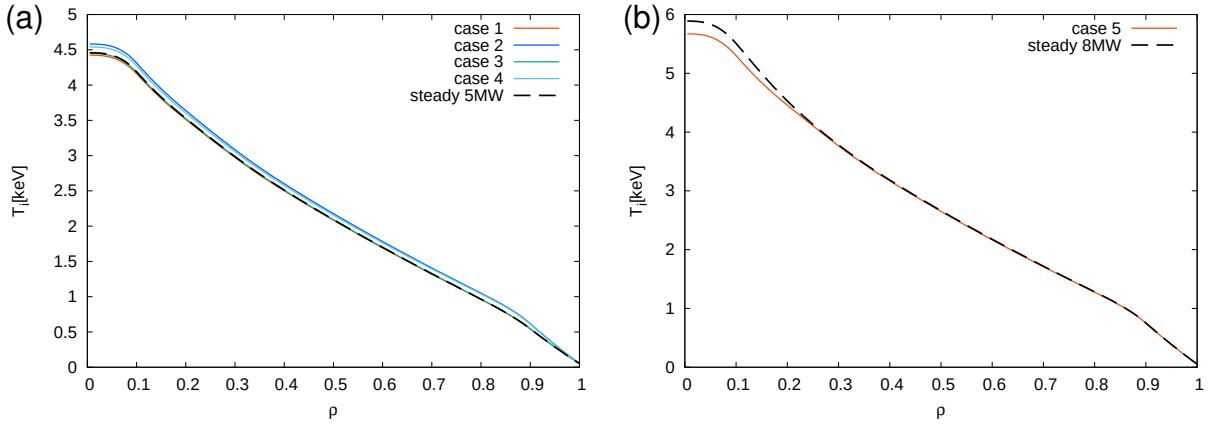

Fig. 5.8: Time averaged temperature profiles in a time window of $t \geq 0.2$sec, (a) $P_{\rm ave} = 5$MW, and (b) $P_{\rm ave} = 8$MW.

5.2.2 Magnetic field modulation

In this subsection, magnetic field modulation is considered. Since the geometry of confinement magnetic fields has stronger impacts on the transport dynamics in comparison to the heating modulation, we first start to treat the sinusoidal modulation of the several metric tensor components rather than directly varying the whole magnetic fields. Here, the three components in the metric tensor g^{xx}, g^{xy}, and g^{yy} are modulated by the following expression,

$$g^{ij}(t) = \left(1 + \lambda_{\mathrm{B}} \sin(2\pi\omega_{\mathrm{B}} t)\right) g^{ij}_{\mathrm{ave}}, \tag{5.3}$$

where $(i,j) = \{(x,x),(x,y),(y,y)\}$. The metric tensor g^{ij} is defined by the contravariant basis vector $\boldsymbol{e}^i$, $g^{ij} \equiv \boldsymbol{e}^i \cdot \boldsymbol{e}^j (i,j = \{x,y,z\})$, and (x,y,z) represents the fluxtube coordinates in the toroidal magnetic geometry. The magnetic field strength and the metric tensor components satisfy the following relation,

$$\begin{aligned} B &= RB_0 \left(1 + \lambda_{\mathrm{B}} \sin(2\pi\omega_{\mathrm{B}} t)\right) \left(g^{yy}_{\mathrm{ave}} g^{xx}_{\mathrm{ave}} - \left(g^{xy}_{\mathrm{ave}}\right)^2\right)^{\frac{1}{2}} \\ &= C_B(t) \left(g^{yy}_{\mathrm{ave}} g^{xx}_{\mathrm{ave}} - \left(g^{xy}_{\mathrm{ave}}\right)^2\right)^{\frac{1}{2}}, \end{aligned} \tag{5.4}$$

where, $C_B(t) \equiv RB_0 \left(1 + \lambda_{\mathrm{B}} \sin(2\pi\omega_{\mathrm{B}} t)\right)$ is the modulation coefficient of magnetic field. Thus, the periodic modulation in the three metric tensor components yields the periodic modulation in the magnetic field intensity as well. The conditions of the magnetic modulation are summarized in Tab. 5.4. Here, the heating is treated to be stationary in 5MW.

Table 5.4: Parameters for magnetic modulation

	λ_B	ω_{B} [sec^{-1}]
case 1	0.3	5
case 2	0.3	10
case 3	0.3	100

The simulation results for cases 1 to 3 are shown in Figs. 5.9 to 5.11, respec-

tively. As in Sec. 5.2.1, the fluctuating components are displayed by subtracting the steady–state profiles in the case with stationary heating. Unlike the heating power modulation, one finds complicated spatio–temporal evolutions rather than a simple sinusoidal response. Nevertheless, the turbulent diffusivity and zonal–flow decay time are periodically suppressed or enhanced. It is noted that the fluctuation amplitude of $\tau_{\rm ZF}$ is larger in comparison to that in the heating power modulation case. This is because the zonal-flow response is nonlinearly influenced by the magnetic geometry [86, 87]. As a result, relatively stronger transport suppression occurs in the magnetic modulation cases. It is however noted that some discontinuous–like behaviors are also observed in, e.g., the temperature gradient and bootstrap current, and one needs to optimize the numerical conditions (time step, radial resolution, etc.) to examine them.

The time evolution of the ion temperature for $\rho = 0.2$ and 0.5 is shown in Fig. 5.12, where the stationary heating case is also displayed for comparison. It is found that, in all cases, the time evolution of ion temperature in the magnetic modulation cases much deviates from the stationary heating case. This point is also reflected in the time-averaged temperature profile shown in Fig. 5.13, where almost similar profiles are observed in the magnetic modulation cases regardless of ω_B. Even though fully consistent modulations of the whole confinement magnetic fields are not treated in the present study, the simulation results imply a nonlinear impact of the magnetic modulation on the transport reduction to improve the thermal confinement.

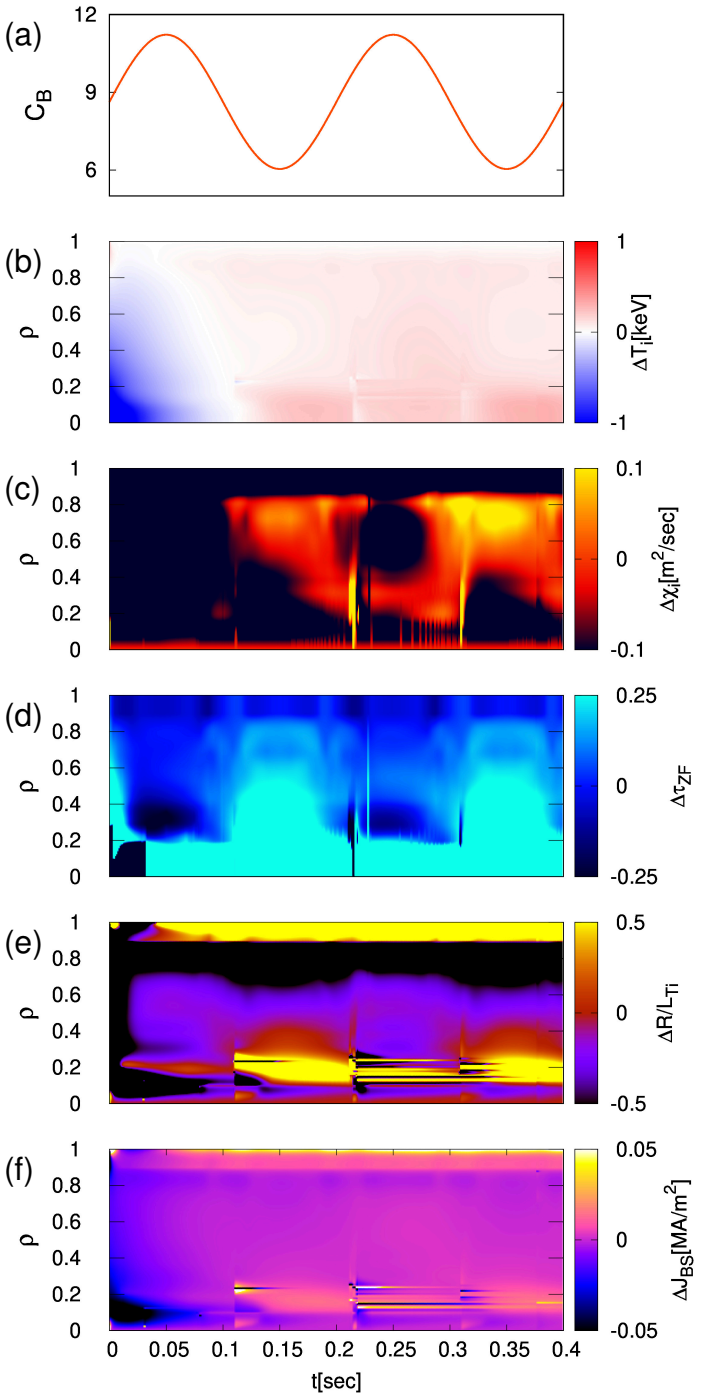

Fig. 5.9: Spatio-temporal evolutions in magnetic modulation with case 1, where the fluctuation components are displayed. Amplitude, frequency, and average heating power are, $\lambda_{\rm B} = 0.3$, and $\omega_{\rm B} = 5{\rm sec}^{-1}$, respectively. (a) modulation coefficient of magnetic field, (b) ion temperature, (c) turbulent diffusivity, (d) zonal–flow decay time, (e) ion temperature gradient, (f) bootstrap current.

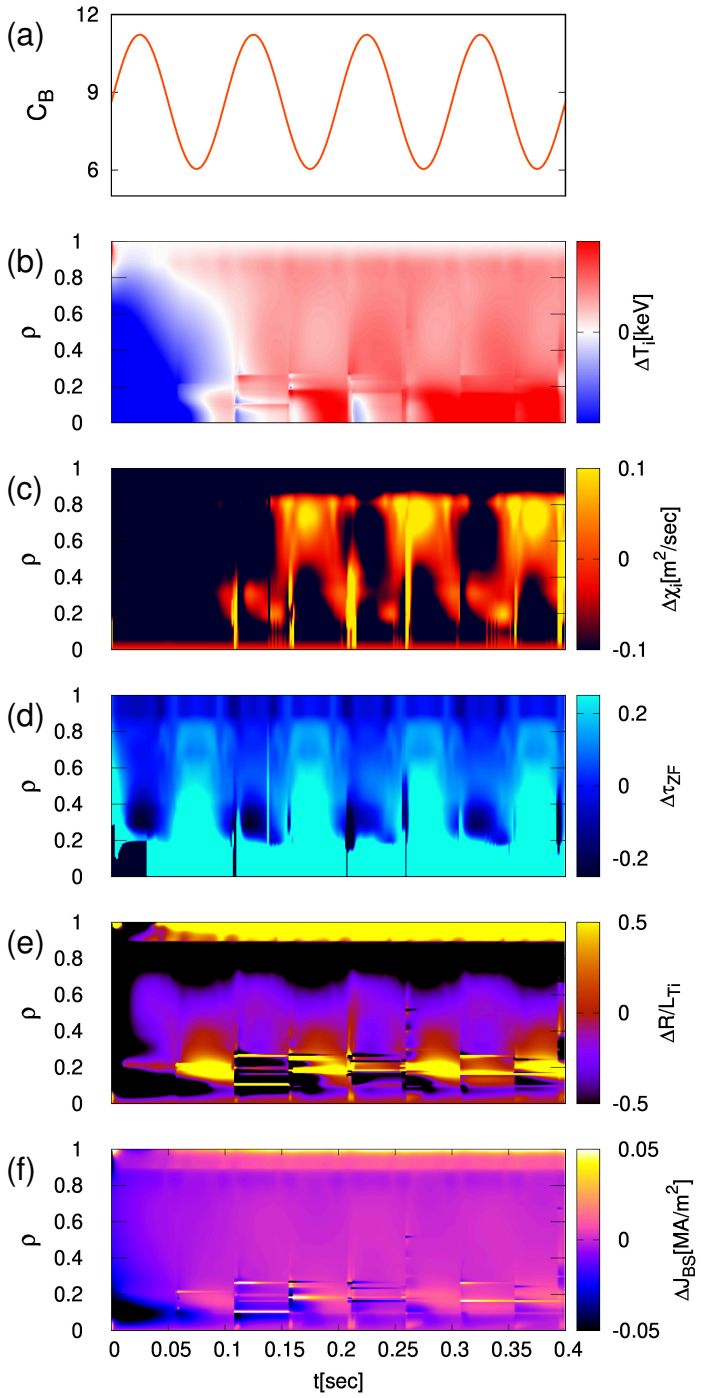

Fig. 5.10: Spatio-temporal evolutions in magnetic modulation with case 2, where the fluctuation components are displayed. Amplitude, frequency, and average heating power are, $\lambda_{\rm B} = 0.3$, and $\omega_{\rm B} = 10{\rm sec}^{-1}$, respectively. (a) modulation coefficient of magnetic field, (b) ion temperature, (c) turbulent diffusivity, (d) zonal–flow decay time, (e) ion temperature gradient, (f) bootstrap current.

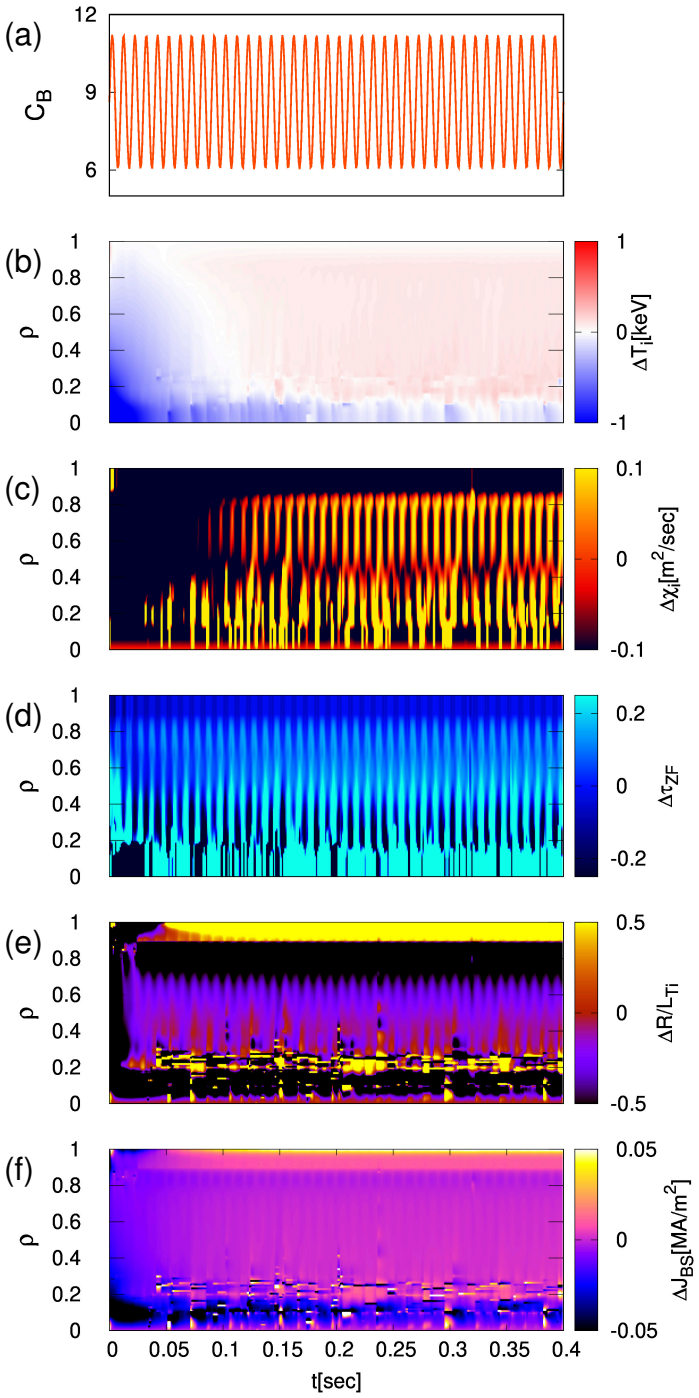

Fig. 5.11: Spatio-temporal evolutions in magnetic modulation with case 3, where the fluctuation components are displayed. Amplitude, frequency, and average heating power are, $\lambda_{\rm B} = 0.3$, and $\omega_{\rm B} = 100{\rm sec}^{-1}$, respectively. (a) modulation coefficient of magnetic field, (b) ion temperature, (c) turbulent diffusivity, (d) zonal–flow decay time, (e) ion temperature gradient, (f) bootstrap current.

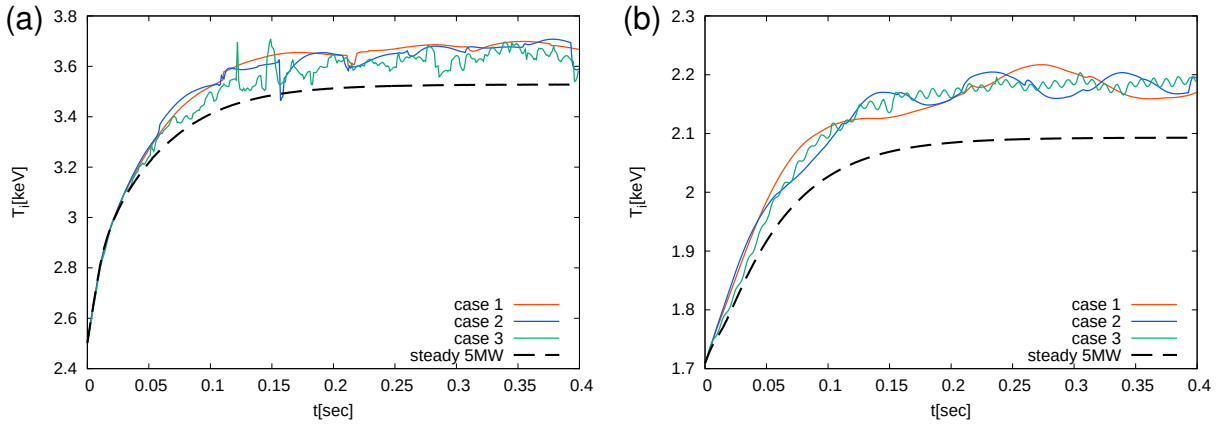

Fig. 5.12: Time evolution of ion temperature at (a)$\rho = 0.2$ and (b)$\rho = 0.5$ with the magnetic modulation.

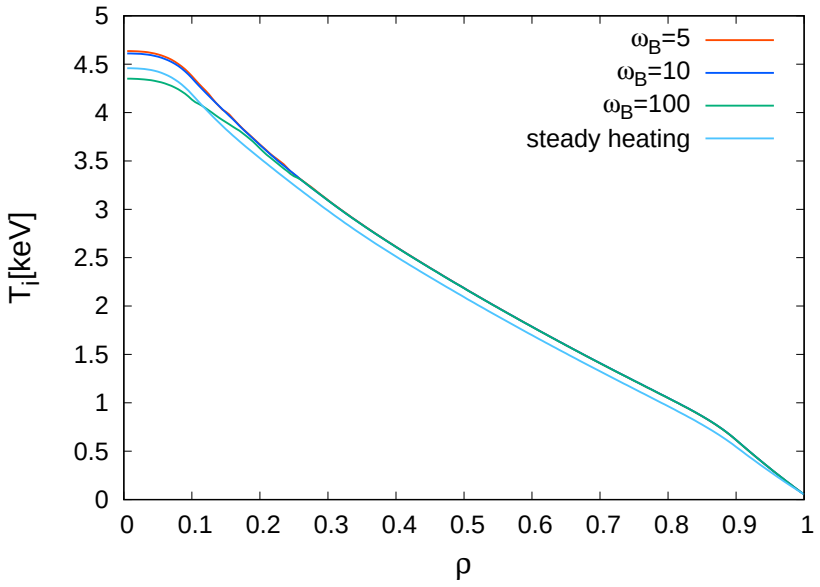

Fig. 5.13: Time averaged temperature profiles in a time window of $t \geq 0.2$sec, with the magnetic modulation.

5.3 Discussion

In this chapter, a new global transport simulation based on the co–simulation framework and the simplified turbulent transport model is presented. Then, the impacts of the temporal modulation in the heating power and the magnetic fields on the turbulent diffusivity, zonal-flows, and pressure profiles are investigated. Although the modulation considered here, which is analytically given, is not influenced by the feedback from the pressure profile formation, the several fundamental behaviors in the global transport with background variations are revealed as follows:

(i) Profile formation responds to the heating power modulation, where the time delay appears depending on the modulation frequency.

(ii) A slight radial propagation of turbulent thermal diffusivity was observed.

(iii) An increase in the average temperature profile was observed in the case with heating power modulation.

(iv) Temporal modulation of the magnetic field directly affects turbulent thermal diffusivity and zonal flows.

(v) Non–sinusoidal temperature profile response is found even in the case with sinusoidal magnetic field modulation.

In the present analysis, we consider separately the heating modulation and magnetic modulation, and the different magnitude of fluctuation amplitude are observed in the physical quantities. It should be noted that these two modulation effects are not independent, but couple each other through the variation of the bootstrap current determined by the pressure profile evolution. To evaluate the consistent magnetic modulation from the bootstrap current, one needs to couple the MHD equilibrium solver with AGITO by utilizing MPMD advantages. Also,

the magnetic modulation can be extended to the 3-dimensional variations which are inspired from the RMP control magnetic coils and fully 3-dimendional stellarators.

Since the pressure profile evolution depends not only on the temperature profile but also the density profile, the extension of incorporating the turbulent particle transport and the fueling modulation effects is another important task. There are many capabilities to explore the new scenarios of the global profile evolution with background variation in fusion burning plasmas by these extensions. These issues will be addressed in future works.

The AGITO code is based on the local gyrokinetic model connected through the radial diffusion of the temperature profile. When increasing the number of local gyrokinetic calculations with enough small time steps, non–local turbulent transport is expected to be more significant. In particular, comparing such results with global full–f simulation results can highlight the origin of turbulence locality/non–locality. The transient behavior of non–local turbulence and its relationship to the internal transport barrier(ITB) formation has also been suggested [88], and such dedicated comparisons to explore new physical insights to control the turbulent transport.

Chapter 6

Summary

One of the most important issues in fusion plasma research is to clarify global dynamics of turbulent transport and profile formations. Particularly, the impacts of background variation on the global transport dynamics, which is expected in burning plasmas, are still unclear. For instance, the background variation appears as a spatio–temporal variation of the heating, fueling, and confinement magnetic fields, which is strongly coupled with the pressure profile evolution in plasmas. The conventional approaches based on the integrated transport simulation or the global full–f gyrokinetic simulation have often ignored this point.

In this study, a novel global transport simulation code, AGITO, is developed by utilizing the co–simulation framework, where discretely distributed local gyrokinetic calculations are directly coupled with a 1–D transport calculation to solve the time evolution of kinetic profiles. An extended simplified modeling of the ITG driven turbulent transport and zonal flows, which enable us to accurately evaluate the nonlinear gyrokinetic simulation results, plays a crucial role in the establishment of the new global transport simulation mentioned above. This simplified transport model introduces a zonal–flow decay time related to the correlation time between zonal–flow and turbulence, which has not been considered in the previous fluid–based models such as TGLF [24]. In addition to the phenomenological arguments, mathematical optimization techniques are utilized to identify

an optimal formula for the simplified turbulent transport model. By means of AGITO, which solves global profile evolutions based on the co-simulation framework, several new findings on the impacts of the heating power modulation and the magnetic modulation on the turbulent transport are obtained in this study.

Highlighted findings are summarized as follows:

(i) A nonlinear functional relation(NFR), which describes a phenomenological functional relation among the turbulent diffusivity, turbulence intensity, and zonal–flow intensity observed in the nonlinear gyrokinetic ITG turbulence simulation, has successfully been identified by means of mathematical optimization techniques.

(ii) A novel simplified turbulent transport model based on the NFR has been constructed by further modeling of the turbulence intensity and zonal–flow intensity with quantities in the linear gyrokinetic calculations. It reproduces the results of nonlinear simulations from linear calculations and significantly reduces computational costs. An improved reproduction accuracy for a wider parameter range including near– and far–marginal ITG stability has also been verified.

(iii) A new global transport simulation, AGITO, has been developed by utilizing a co–simulation framework with the simplified turbulent transport model developed above. The numerical verification of AGITO is successfully confirmed by global ITG–driven turbulence simulations with the stationary heating.

(iv) The impacts of the heating power modulation and background magnetic modulation on the global profile evolutions in turbulent plasmas have been also investigated. A significant deviation from the cases with the stationary heating has been identified. In some cases, heating power modulation causes an increase in the temperature profile even though the average heating power remains the same.

There are still some capabilities of extending the present study. Here, we focused on the simplified modeling of the local turbulent heat diffusivity, but the simultaneous modeling with the turbulent particle transport is an important task for more quantitative predictions including the density profile evolution. Also, the consideration of electromagnetic turbulence appearing in high–beta plasmas is another work to be addressed. As for the AGITO, some optimizations of numerical scheme including more robust convergence criteria are necessary to enhance the applicability to wider practical problems e.g. magnetic field modulation driven by bootstrap currents. As discussed in Sec. 5.3, the self–consistent coupling between background variation and the pressure profile evolution through the turbulent transport should be incorporated in future works. We expect that these new frameworks on the modeling and simulation contribute to explore further possibilities of the plasma confinement in the burning plasmas.

List of publications

[1] Tomonari Nakayama, Motoki Nakata, Mitsuru Honda, Masanori Nunami, and Seikichi Matsuoka, “Nonlinear functional relation covering near- and far-marginal stability in ion temperature gradient driven turbulence”, Plasma Physics and Controlled Fusion, **64**(7):075007, 2022.

[2] Emi Narita, Mitsuru Honda, Motoki Nakata, Nobuhiko Hayashi, Tomonari Nakayama, and Maiko Yoshida, “Modification of a machine learning-based semi-empirical turbulent transport model for its versatility”, Contributions to Plasma Physics, **63**(5-6):e202200152, 2023.

[3] Tomonari Nakayama, Motoki Nakata, Masanori Nunami, Mitsuru Honda, Emi Narita, and Seikichi Matsuoka, “A simplified model to estimate nonlinear turbulent transport by linear dynamics in plasma turbulence”, Scientific Reports, **13** 2319, 2023.

Bibliography

[1] W. Horton, "Drift waves and transport," *Reviews of Modern Physics*, vol. 71, pp. 735–778, 1999.

[2] X. Garbet, Y. Idomura, L. Villard, and T. Watanabe, "Gyrokinetic simulations of turbulent transport," *Nuclear Fusion*, vol. 50, p. 043002, 2010.

[3] N. Howard, C. Holland, A. White, M. Greenwald, and J. Candy, "Multi-scale gyrokinetic simulation of tokamak plasmas: Enhanced heat loss due to cross-scale coupling of plasma turbulence," *Nuclear Fusion*, vol. 56, p. 014004, 2016.

[4] S. Maeyama, T.-H. Watanabe, Y. Idomura, M. Nakata, A. Ishizawa, and M. Nunami, "Cross-scale interactions between turbulence driven by electron and ion temperature gradients via sub-ion-scale structures," *Nuclear Fusion*, vol. 57, p. 066036, 2017.

[5] S. Maeyama, T.-H. Watanabe, M. Nakata, M. Nunami, Y. Asahi, and A. Ishizawa, "Multi-scale turbulence simulation suggesting improvement of electron heated plasma confinement," *Nature Communications*, vol. 13, p. 3166, 2022.

[6] M. Nakata and M. Honda, "Gyrokinetic Turbulent Transport Simulations on Steady Burning Condition in D-T-He Plasmas," *Plasma and Fusion Research*, vol. 17, pp. 1 403 083–1 403 083, 2022.

[7] M. Nakata, M. Nunami, H. Sugama, and T.-H. Watanabe, "Impact of hydrogen isotope species on microinstabilities in helical plasmas," *Plasma Physics and Controlled Fusion*, vol. 58, p. 074008, 2016.

[8] M. Nakata, K. Nagaoka, K. Tanaka, H. Takahashi, M. Nunami, S. Satake, M. Yokoyama, F. Warmer, and the LHD Experiment Group, "Gyrokinetic microinstability analysis of high- T_{i} and high- T_{e} isotope plasmas in Large Helical Device," *Plasma Physics and Controlled Fusion*, vol. 61, p. 014016, 2019.

[9] Y. Idomura, "Full- f gyrokinetic simulation over a confinement time," *Physics of Plasmas*, vol. 21, p. 022517, 2014.

[10] M. Nakata and Y. Idomura, "Plasma size and collisionality scaling of ion-temperature-gradient-driven turbulence," *Nuclear Fusion*, vol. 53, p. 113039, 2013.

[11] G. Merlo, J. Dominski, A. Bhattacharjee, C. S. Chang, F. Jenko, S. Ku, E. Lanti, and S. Parker, "Cross-verification of the global gyrokinetic codes GENE and XGC," *Physics of Plasmas*, vol. 25, p. 062308, 2018.

[12] G. Dif-Pradalier, G. Hornung, Ph. Ghendrih, Y. Sarazin, F. Clairet, L. Vermare, P. H. Diamond, J. Abiteboul, T. Cartier-Michaud, C. Ehrlacher, D. Estève, X. Garbet, V. Grandgirard, Ö. D. Gürcan, P. Hennequin, Y. Kosuga, G. Latu, P. Maget, P. Morel, C. Norscini, R. Sabot, and A. Storelli, "Finding the Elusive E × B Staircase in Magnetized Plasmas," *Physical Review Letters*, vol. 114, p. 085004, 2015.

[13] B. F. McMillan, S. Jolliet, T. M. Tran, L. Villard, A. Bottino, and P. Angelino, "Avalanchelike bursts in global gyrokinetic simulations," *Physics of Plasmas*, vol. 16, p. 022310, 2009.

[14] Y. Sarazin, V. Grandgirard, J. Abiteboul, S. Allfrey, X. Garbet, Ph. Ghendrih, G. Latu, A. Strugarek, and G. Dif-Pradalier, "Large scale dynamics in flux driven gyrokinetic turbulence," *Nuclear Fusion*, vol. 50, p. 054004, 2010.

[15] "TASK," https:// bpsi.nucleng.kyoto-u.ac.jp/task/.

[16] M. Honda and A. Fukuyama, "Dynamic transport simulation code including plasma rotation and radial electric field," *Journal of Computational Physics*, vol. 227, pp. 2808–2844, 2008.

[17] M. Yokoyama, A. Wakasa, R. Seki, M. Sato, S. Murakami, C. Suzuki, Y. Nakamura, A. Fukuyama, and LHD Experiment Group, "Development of Integrated Transport Code, TASK3D, and Its Applications to LHD Experiment," *Plasma and Fusion Research*, vol. 7, pp. 2 403 011–2 403 011, 2012.

[18] N. Hayashi and JT-60 Team, "Advanced tokamak research with integrated modeling in JT-60 Upgrade," *Physics of Plasmas*, vol. 17, p. 056112, 2010.

[19] M. Honda, S. Satake, Y. Suzuki, G. Matsunaga, K. Shinohara, M. Yoshida, A. Matsuyama, S. Ide, and H. Urano, "Experimental analyses and predictive simulations of toroidal rotation driven by the neoclassical toroidal viscosity in rippled tokamaks," *Nuclear Fusion*, vol. 54, p. 114005, 2014.

[20] M. Honda and E. Narita, "Development of a Surrogate Turbulent Transport Model and Its Usefulness in Transport Simulations," *Plasma and Fusion Research*, vol. 16, pp. 2 403 002–2 403 002, 2021.

[21] M. Honda, "Application of genetic algorithms to modelings of fusion plasma physics," *Computer Physics Communications*, vol. 231, pp. 94–106, 2018.

[22] A. J. Brizard and T. S. Hahm, "Foundations of nonlinear gyrokinetic theory," *Reviews of Modern Physics*, vol. 79, pp. 421–468, 2007.

[23] R. E. Waltz, G. M. Staebler, W. Dorland, G. W. Hammett, M. Kotschenreuther, and J. A. Konings, "A gyro-Landau-fluid transport model," *Physics of Plasmas*, vol. 4, pp. 2482–2496, 1997.

[24] G. M. Staebler, J. E. Kinsey, and R. E. Waltz, "Gyro-Landau fluid equations for trapped and passing particles," *Physics of Plasmas*, vol. 12, p. 102508, 2005.

[25] G. M. Staebler, J. E. Kinsey, and R. E. Waltz, "A theory-based transport model with comprehensive physics," *Physics of Plasmas*, vol. 7, pp. 466–480, 2007.

[26] J. E. Kinsey, G. M. Staebler, and R. E. Waltz, "The first transport code simulations using the trapped gyro-Landau-fluid model," *Physics of Plasmas*, vol. 15, p. 055908, 2008.

[27] C. Bourdelle, X. Garbet, F. Imbeaux, A. Casati, N. Dubuit, R. Guirlet, and T. Parisot, "A new gyrokinetic quasilinear transport model applied to particle transport in tokamak plasmas," *Physics of Plasmas*, vol. 14, p. 112501, 2007.

[28] G. Staebler, N. Howard, J. Candy, and C. Holland, "A model of the saturation of coupled electron and ion scale gyrokinetic turbulence," *Nuclear Fusion*, vol. 57, p. 066046, 2017.

[29] G. M. Staebler, R. E. Waltz, J. Candy, and J. E. Kinsey, "New Paradigm for Suppression of Gyrokinetic Turbulence by Velocity Shear," *Physical Review Letters*, vol. 110, p. 055003, 2013.

[30] M. Nunami, T.-H. Watanabe, and H. Sugama, "A reduced model for ion temperature gradient turbulent transport in helical plasmas," *Physics of Plasmas*, vol. 20, p. 092307, 2013.

[31] S. Toda, M. Nakata, M. Nunami, A. Ishizawa, T.-H. Watanabe, and H. Sugama, "A Reduced Transport Model for Ion Heat Diffusivity by Gyro-

Kinetic Analysis with Kinetic Electrons in Helical Plasmas," *Plasma and Fusion Research*, vol. 12, pp. 1 303 035–1 303 035, 2017.

[32] S. Toda, M. Nakata, M. Nunami, A. Ishizawa, T.-H. Watanabe, and H. Sugama, "Modeling of turbulent particle and heat transport in helical plasmas based on gyrokinetic analysis," *Physics of Plasmas*, vol. 26, p. 012510, 2019.

[33] S. Toda, M. Nakata, M. Nunami, A. Ishizawa, T.-H. Watanabe, and H. Sugama, "Transport Simulation for Helical Plasmas by use of Gyrokinetic Transport Model," *Plasma and Fusion Research*, vol. 14, pp. 3 403 061–3 403 061, 2019.

[34] S. Toda, M. Nunami, and H. Sugama, "Reduced models of turbulent transport in helical plasmas including effects of zonal flows and trapped electrons," *Journal of Plasma Physics*, vol. 86, p. 815860304, 2020.

[35] M. Honda and E. Narita, "Machine-learning assisted steady-state profile predictions using global optimization techniques," *Physics of Plasmas*, vol. 26, p. 102307, 2019.

[36] J. Citrin, S. Breton, F. Felici, F. Imbeaux, T. Aniel, J. Artaud, B. Baiocchi, C. Bourdelle, Y. Camenen, and J. Garcia, "Real-time capable first principle based modelling of tokamak turbulent transport," *Nuclear Fusion*, vol. 55, p. 092001, 2015.

[37] O. Meneghini, S. Smith, P. Snyder, G. Staebler, J. Candy, E. Belli, L. Lao, M. Kostuk, T. Luce, T. Luda, J. Park, and F. Poli, "Self-consistent core-pedestal transport simulations with neural network accelerated models," *Nuclear Fusion*, vol. 57, p. 086034, 2017.

[38] E. Narita, M. Honda, M. Nakata, M. Yoshida, H. Takenaga, and N. Hayashi, "Gyrokinetic modelling of the quasilinear particle flux for plasmas with

neutral-beam fuelling," *Plasma Physics and Controlled Fusion*, vol. 60, p. 025027, 2018.

[39] E. Narita, M. Honda, M. Nakata, M. Yoshida, N. Hayashi, and H. Takenaga, "Neural-network-based semi-empirical turbulent particle transport modelling founded on gyrokinetic analyses of JT-60U plasmas," *Nucl. Fusion*, 2019.

[40] E. Narita, M. Honda, M. Nakata, N. Hayashi, T. Nakayama, and M. Yoshida, "Modification of a machine learning-based semi-empirical turbulent transport model for its versatility," *Contributions to Plasma Physics*, vol. 63, p. e202200152, 2023.

[41] T. Nakayama, M. Nakata, M. Honda, M. Nunami, and S. Matsuoka, "Nonlinear functional relation covering near- and far-marginal stability in ion temperature gradient driven turbulence," *Plasma Physics and Controlled Fusion*, vol. 64, p. 075007, 2022.

[42] A. M. Dimits, G. Bateman, M. A. Beer, B. I. Cohen, W. Dorland, G. W. Hammett, C. Kim, J. E. Kinsey, M. Kotschenreuther, A. H. Kritz, L. L. Lao, J. Mandrekas, W. M. Nevins, S. E. Parker, A. J. Redd, D. E. Shumaker, R. Sydora, and J. Weiland, "Comparisons and physics basis of tokamak transport models and turbulence simulations," *Physics of Plasmas*, vol. 7, pp. 969–983, 2000.

[43] A. A. Schekochihin, E. G. Highcock, and S. C. Cowley, "Subcritical fluctuations and suppression of turbulence in differentially rotating gyrokinetic plasmas," *Plasma Physics and Controlled Fusion*, vol. 54, p. 055011, 2012.

[44] F. van Wyk, E. G. Highcock, A. A. Schekochihin, C. M. Roach, A. R. Field, and W. Dorland, "Transition to subcritical turbulence in a tokamak plasma," *Journal of Plasma Physics*, vol. 82, p. 905820609, 2016.

[45] M. Nakata, M. Nunami, H. Sugama, and T.-H. Watanabe, "Isotope Effects on Trapped-Electron-Mode Driven Turbulence and Zonal Flows in Helical and Tokamak Plasmas," *Physical Review Letters*, vol. 118, p. 165002, 2017.

[46] T.-H. Watanabe and H. Sugama, "Velocity–space structures of distribution function in toroidal ion temperature gradient turbulence," *Nuclear Fusion*, vol. 46, pp. 24–32, 2006.

[47] M. N. Rosenbluth and F. L. Hinton, "Poloidal Flow Driven by Ion-Temperature-Gradient Turbulence in Tokamaks," *Physical Review Letters*, vol. 80, pp. 724–727, 1998.

[48] P. H. Diamond, S.-I. Itoh, K. Itoh, and T. S. Hahm, "Zonal flows in plasma—a review," *Plasma Physics and Controlled Fusion*, vol. 47, pp. R35–R161, 2005.

[49] T. Hahm, L. Wang, W. Wang, E. Yoon, and F. Duthoit, "Isotopic dependence of residual zonal flows," *Nuclear Fusion*, vol. 53, p. 072002, 2013.

[50] K. Levenberg, "A method for the solution of certain non-linear problems in least squares," *Quarterly of Applied Mathematics*, vol. 2, pp. 164–168, 1944.

[51] D. W. Marquardt, "An Algorithm for Least-Squares Estimation of Nonlinear Parameters," *Journal of the Society for Industrial and Applied Mathematics*, vol. 11, pp. 431–441, 1963.

[52] Z. Lin, T. S. Hahm, W. W. Lee, W. M. Tang, and R. B. White, "Gyrokinetic simulations in general geometry and applications to collisional damping of zonal flows," *Physics of Plasmas*, vol. 7, pp. 1857–1862, 2000.

[53] B. B. Kadomtsev, *PLASMA TURBULENCE.*, 1965.

[54] S. Baschetti, H. Bufferand, G. Ciraolo, N. Fedorczak, P. Ghendrih, P. Tamain, and E. Serre, "A κ - ϵ model for plasma anomalous transport

in tokamaks: Closure via the scaling of the global confinement," *Nuclear Materials and Energy*, vol. 19, pp. 200–204, 2019.

[55] S. Baschetti, H. Bufferand, G. Ciraolo, Ph. Ghendrih, E. Serre, P. Tamain, and t. WEST Team, "Self-consistent cross-field transport model for core and edge plasma transport," *Nuclear Fusion*, vol. 61, p. 106020, 2021.

[56] B. F. McMillan, X. Lapillonne, S. Brunner, L. Villard, S. Jolliet, A. Bottino, T. Görler, and F. Jenko, "System Size Effects on Gyrokinetic Turbulence," *Physical Review Letters*, vol. 105, p. 155001, 2010.

[57] F. Rath, A. G. Peeters, R. Buchholz, S. R. Grosshauser, P. Migliano, A. Weikl, and D. Strintzi, "Comparison of gradient and flux driven gyrokinetic turbulent transport," *Physics of Plasmas*, vol. 23, p. 052309, 2016.

[58] A. G. Peeters, F. Rath, R. Buchholz, Y. Camenen, J. Candy, F. J. Casson, S. R. Grosshauser, W. A. Hornsby, D. Strintzi, and A. Weikl, "Gradient-driven flux-tube simulations of ion temperature gradient turbulence close to the non-linear threshold," *Physics of Plasmas*, vol. 23, p. 082517, 2016.

[59] T. Nakayama, M. Nakata, M. Nunami, M. Honda, E. Narita, and S. Matsuoka, "A simplified model to estimate nonlinear turbulent transport by linear dynamics in plasma turbulence," *Scientific Reports*, vol. 13, no. 1, p. 2319, 2023.

[60] J. Artaud, V. Basiuk, F. Imbeaux, M. Schneider, J. Garcia, G. Giruzzi, P. Huynh, T. Aniel, F. Albajar, J. Ané, A. Bécoulet, C. Bourdelle, A. Casati, L. Colas, J. Decker, R. Dumont, L. Eriksson, X. Garbet, R. Guirlet, P. Hertout, G. Hoang, W. Houlberg, G. Huysmans, E. Joffrin, S. Kim, F. Köchl, J. Lister, X. Litaudon, P. Maget, R. Masset, B. Pégourié, Y. Peysson, P. Thomas, E. Tsitrone, and F. Turco, "The CRONOS suite of codes for integrated tokamak modelling," *Nuclear Fusion*, vol. 50, p. 043001, 2010.

[61] K. Imadera, Y. Kishimoto, K. Obrejan, T. Kobiki, and J.-Q. Li, "Global Profile Relaxation Coupled with ExB Staircase in Toroidal Flux-Driven ITG Turbulence," in *25TH IAEA FUSION ENERGY CONFERENCE*, 2014.

[62] K. Imadera, J.-Y. Lin, D. Nakajima, and Y. Kishimoto, "Study of Plasma Shaping Effects on ITG Instability Using Global Gyrokinetic Code GKNET with Analytical Magnetic Equilibrium," *Plasma and Fusion Research*, vol. 15, pp. 1 403 086–1 403 086, 2020.

[63] K. Imadera and Y. Kishimoto, "ITB formation in gyrokinetic flux-driven ITG/TEM turbulence," *Plasma Physics and Controlled Fusion*, vol. 65, p. 024003, 2023.

[64] C. Gomes, C. Thule, D. Broman, P. G. Larsen, and H. Vangheluwe, "Co-simulation: State of the art," 2017.

[65] Y. Yamade, C. Kato, S. Yoshimura, A. Iida, K. Iida, K. Onda, Y. Hashizume, and Y. Gou, "Prediction of Aeroacoustical Interior Noise of a Car, Part-1 Prediction of Pressure Fluctuations on External Surfaces of a Car," in *SAE 2016 World Congress and Exhibition*, 2016, pp. 2016–01–1617.

[66] S. Minami and S. Yoshimura, "Performance evaluation of nonlinear algorithms with line-search for partitioned coupling techniques for fluid–structure interactions," *International Journal for Numerical Methods in Fluids*, vol. 64, pp. 1129–1147, 2010.

[67] P. Braconnot, B. Otto-Bliesner, S. Harrison, S. Joussaume, J.-Y. Peterchmitt, A. Abe-Ouchi, M. Crucifix, E. Driesschaert, Th. Fichefet, C. D. Hewitt, M. Kageyama, A. Kitoh, A. Laîné, M.-F. Loutre, O. Marti, U. Merkel, G. Ramstein, P. Valdes, S. L. Weber, Y. Yu, and Y. Zhao, "Results of PMIP2 coupled simulations of the Mid-Holocene and Last Glacial Maximum – Part 1: Experiments and large-scale features," *Climate of the Past*, vol. 3, pp. 261–277, 2007.

[68] T. D. Scheibe, E. M. Murphy, X. Chen, A. K. Rice, K. C. Carroll, B. J. Palmer, A. M. Tartakovsky, I. Battiato, and B. D. Wood, "An Analysis Platform for Multiscale Hydrogeologic Modeling with Emphasis on Hybrid Multiscale Methods," *Groundwater*, vol. 53, pp. 38–56, 2015.

[69] X. Zuo, Z. Xu, H. Jia, Y. Mu, M. Zhang, M. Yuan, and C. Wu, "Co-simulation of hypertensive left ventricle based on computational fluid dynamics and a closed-loop network model," *Computer Methods and Programs in Biomedicine*, vol. 216, p. 106649, 2022.

[70] J. H. Müller, S. Razu, A. Erdemir, and T. M. Guess, "Prediction of patellofemoral joint kinematics and contact through co-simulation of rigid body dynamics and nonlinear finite element analysis," *Computer Methods in Biomechanics and Biomedical Engineering*, vol. 23, pp. 718–733, 2020.

[71] M. Barnes, I. G. Abel, W. Dorland, T. Görler, G. W. Hammett, and F. Jenko, "Direct multiscale coupling of a transport code to gyrokinetic turbulence codes," *Physics of Plasmas*, vol. 17, p. 056109, 2010.

[72] M. Honda and M. Nakata, "Global transport simulations of electron and ion heat transport in ITG/TEM unstable plasmas using TRESS+GKV code," in *ITPA Transport and Confinement Topical Group, NakaITPA*, 2016.

[73] M. Kikuchi and M. Azumi, "Experimental evidence for the bootstrap current in a tokamak," *Plasma Physics and Controlled Fusion*, vol. 37, pp. 1215–1238, 1995.

[74] H. Akima, "A New Method of Interpolation and Smooth Curve Fitting Based on Local Procedures," *Journal of the ACM*, vol. 17, pp. 589–602, 1970.

[75] H. Akima, "A method of univariate interpolation that has the accuracy of a third-degree polynomial," *ACM Transactions on Mathematical Software*, vol. 17, pp. 341–366, 1991.

[76] S. Jardin, *Computational Methods in Plasma Physics*. CRC Press, 2010.

[77] K. H. Burrell, "Effects of E×B velocity shear and magnetic shear on turbulence and transport in magnetic confinement devices," *Physics of Plasmas*, vol. 4, pp. 1499–1518, 1997.

[78] G. Dif-Pradalier, V. Grandgirard, Y. Sarazin, X. Garbet, Ph. Ghendrih, and P. Angelino, "On the influence of initial state on gyrokinetic simulations," *Physics of Plasmas*, vol. 15, p. 042315, 2008.

[79] Y. Idomura, H. Urano, N. Aiba, and S. Tokuda, "Study of ion turbulent transport and profile formations using global gyrokinetic full-f Vlasov simulation," *Nuclear Fusion*, vol. 49, p. 065029, 2009.

[80] G. Dif-Pradalier, V. Grandgirard, Y. Sarazin, X. Garbet, and Ph. Ghendrih, "Interplay between Gyrokinetic Turbulence, Flows, and Collisions: Perspectives on Transport and Poloidal Rotation," *Physical Review Letters*, vol. 103, p. 065002, 2009.

[81] G. Dif-Pradalier, P. H. Diamond, V. Grandgirard, Y. Sarazin, J. Abiteboul, X. Garbet, Ph. Ghendrih, A. Strugarek, S. Ku, and C. S. Chang, "On the validity of the local diffusive paradigm in turbulent plasma transport," *Physical Review E*, vol. 82, p. 025401, 2010.

[82] S. Ku, J. Abiteboul, P. Diamond, G. Dif-Pradalier, J. Kwon, Y. Sarazin, T. Hahm, X. Garbet, C. Chang, G. Latu, E. Yoon, Ph. Ghendrih, S. Yi, A. Strugarek, W. Solomon, and V. Grandgirard, "Physics of intrinsic rotation in flux-driven ITG turbulence," *Nuclear Fusion*, vol. 52, p. 063013, 2012.

[83] S. Sugita, K. Itoh, S.-I. Itoh, M. Yagi, G. Fuhr, P. Beyer, and S. Benkadda, "Ballistic propagation of turbulence front in tokamak edge plasmas," *Plasma Physics and Controlled Fusion*, vol. 54, p. 125001, 2012.

[84] P. H. Diamond and T. S. Hahm, "On the dynamics of turbulent transport near marginal stability," *Physics of Plasmas*, vol. 2, pp. 3640–3649, 1995.

[85] X. Garbet and R. E. Waltz, "Heat flux driven ion turbulence," *Physics of Plasmas*, vol. 5, pp. 2836–2845, 1998.

[86] M. Nakata and S. Matsuoka, "Impact of Geodesic Curvature on Zonal Flow Generation in Magnetically Conned Plasmas," *Plasma and Fusion Research*, vol. 17, pp. 1 203 077–1 203 077, 2022.

[87] O. Beeke, M. Barnes, M. Romanelli, M. Nakata, and M. Yoshida, "Impact of shaping on microstability in high-performance tokamak plasmas," *Nuclear Fusion*, vol. 61, p. 066020, 2021.

[88] K. Ida, "Non-local transport nature revealed by the research in transient phenomena of toroidal plasma," *Reviews of Modern Plasma Physics*, vol. 6, p. 2, 2022.